UCL Université catholique de Louvain

École polytechnique de Louvain (EPL)

epl

Electrocatalysis of carbon compounds on rutile transition metal oxide catalysts: an ab initio study

Dissertation presented by
Louis STORMS

for obtaining the Master's degree in
Physical Engineering

Supervisor(s)
Geoffroy HAUTIER, Gian-Marco RIGNANESE

Reader(s)
Khaoula BOUKARI, Jean-Christophe CHARLIER

Academic year 2016-2017

Abstract

Rutile transition metals have lately been reported to exhibit outstanding catalytic activity. Whereas the Oxygen Evolution Reaction (OER) has been intensively studied on these catalysts, only very few mentions exist of these materials catalyzing the CO_2 Reduction Reaction. It is in the scope of this work to investigate both electrocatalytic reactions at low potential on IrO_2 and RuO_2 slabs.

Ab initio computations implementing Density Functional Theory (DFT) are used to calculate the total energy of structures with adsorbates. Stability analyses are performed using relative stability diagrams to screen for interesting reaction intermediates in a wide potential range. Free energy diagrams are constructed to identify potential limiting steps in the studied reaction mechanisms. To the extent possible, results are systematically confronted to reference work.

The critical influence of Zero Point Energy (ZPE) and van der Waals (vdW) corrections on the simulations are exposed.
RuO_2 is found to display increased affinity with OER intermediates as compared to IrO_2. A hydrogen-covered surface reconstruction (Ir_2O) on a IrO_2 slab is shown to exhibit competing stability with conventional IrO_2 surface intermediates at potentials below $-0.52\,V$.

Within the thermodynamic limits of this work, IrO_2 displays better affinity with carbon adsorbates and better performances in the CO_2 Reduction Reaction to methane than RuO_2. The CO_2 Reduction Reaction is shown to become favorable as from potentials as low as $-0.22\,V$ on an IrO_2 catalyst, in contrast to $-0.47\,V$ on RuO_2. At last, CO_2 reduction through a COH^* intermediate on an IrO_2 catalyst appears to be an interesting lead.

Keywords: electrocatalysis, oxygen evolution reaction, CO_2 reduction reaction, density functional theory, IrO_2, RuO_2, methane synthesis

Acknowledgements

I wish to thank all the people who have contributed to the accomplishment of this thesis.

Foremost, I would like to express my sincere gratitude towards my supervisors Prof. Geoffroy Hautier and Prof. Gian-Marco Rignanese for their guidance all along the realization of this work. Not only have they introduced me to this fascinating subject, but they have spent time helping me interpreting results and advising me all along the way up to the finalization of this work. Specifically, I wish to put forward the fact that they have been exceptionally available for me during the last eight months.

Further, I would like to express very special thanks to Jan Kloppenburg, who is a PhD student working on oxide catalysts and has provided invaluable help while running my *ab initio* simulations. He helped me set up the tools to realize my very first simulations with VASP and gave me precious advice when computations did not run smoothly. Moreover, along the numerous conversations we have had he has shared with me his vast knowledge about electrocatalysis. He has always been patient, kind and available.

Moreover, I wish to thank the other members of my jury, Prof. Jean-Christophe Charlier and Dr. Khaoula Boukari who showed interest in this work and took time to read this manuscript.

I also would like to thank all the members of the NAPS division for helping me by any means, for the pleasant atmosphere and for the nice working environment that have prevailed.

Last but not least, I owe more than thanks to my parents, sisters and friends for their incredible support during the entire duration of my education at university. I wish to address special gratitude to my sister Emilie, who has dedicated much energy providing me precious help and advice.

Computational resources have been provided by the supercomputing facilities of the Université Catholique de Louvain (CISM/UCL) and the Consortium des Equipements de Calcul Intensif en Fédération Wallonie-Bruxelles (CECI) funded by the Fonds de la Recherche Scientifique de Belgique (F.R.S.-FNRS).

Louis Storms

Contents

List of Figures

List of Tables

List of abbreviations and symbols

Abbreviations

AE	All-Electron
BZ	Brillouin Zone
CHE	Computational Hydrogen Electrode
CUS	Coordinately Unsaturated Site
DFT	Density Functional Theory
DFT-TS	Tkatchenko-Scheffler DFT method
GGA	Generalized Gradients Approximation
HER	Hydrogen Evolution Reaction
HF	Hartree-Fock
IBZ	Irreducible Brillouin Zone
KS	Kohn-Sham
LDA	Local Density Approximation
MD	Molecular Dynamics
NC-PP	Norm-Conserving Pseudopotential
OER	Oxygen Evolution Reaction
OP	Overpotential
PAW	Projector Augmented Wave
PBE	Perdew-Burke-Ernzerhof
PP	Pseudopotential
PW91	Perdew-Wang 1991
RHE	Reversible Hydrogen Electrode
RPBE	Revised Perdew-Burke-Ernzerhof
SCF	Self-Consistent Field
SHE	Standard Hydrogen Electrode
TS	Tkatchenko-Scheffler
US-PP	Ultrasoft Pseudopotential
VASP	Vienna Ab Initio Simulation Package
vdW	van der Waals
XC	Exchange-Correlation
ZPE	Zero Point Energy

Ag	silver
Ar	argon
Au	gold
C	carbon
Co	cobalt
Cu	copper
Fe	iron
H	hydrogen
Ir	iridium
Ni	nickel
O	oxygen
Pt	platinum
Ru	ruthenium
Ti	titanium
Zn	zinc

Symbols

α	symmetry factor
α_i	polarizability of atom i
ε_i^{HF}	electronic HF eigenenergies
ε_{xc}^{hom}	homogeneous electron gas energy per atom
ε_{xc}^{GGA}	exchange-correlation energy per atom in GGA
ε_{xc}^{LDA}	exchange-correlation energy per atom in LDA
η	overpotential
ν_i	free atomic volume of atom i
ϕ	one-electron wavefunction
Ψ	wavefunction (of a system)
ψ	wavefunction (of an electron)
ψ^N	nuclear wavefunction
Ω	real lattice volume
Ω^*	reciprocal lattice volume
$\mathbf{a}_1, \mathbf{a}_2, \mathbf{a}_3$	real lattice primitive vectors
$\mathbf{b}_1, \mathbf{b}_2, \mathbf{b}_3$	reciprocal lattice primitive vectors
C_{6ij}	dispersion coefficient for atom pair ij
E	total energy
E_{cut}	cutoff energy
$E_{DFT-disp}$	total DFT energy including dispersion correction
E_{disp}	dispersion energy correction
E_{KS-DFT}	Kohn-Sham DFT energy
E_{ext}	interaction energy between electrons and external potential
E_H	Hartree energy
E_{kin}	kinetic energy of the electrons
E_x	exchange energy
E_{xc}	exchange-correlation energy
$f_{d,6}$	damping function
$\mathcal{F}$	Faraday constant
F	functional
$\mathbf{G}$	reciprocal lattice vector
$\widehat{H}$	Hamiltonian operator
j	current density
j_0	exchange current density
$\widehat{J}_j$	Coulomb operator
$\mathbf{k}$	wavevector
$\widehat{K}_j$	exchange operator
M_α	mass of nucleus α
n	band index
N	number of unit cells
N_{at}	number of atoms
N_e	number of electrons
N_N	number of nuclei
$n(\mathbf{r})$	electronic density
$\mathbf{R}$	real lattice vector
R_{0i}	atomic radius
$r_{ij,L}$	distance between atoms i and j in in unit cell L
$\mathbf{R}_\alpha$	coordinates of nucleus α
$\mathbf{r}_i$	coordinates of electron i

r_c	cutoff radius
T	temperature
T_0	kinetic energy functional
$\widehat{T}_e$	electronic kinetic energy operator
$\widehat{T}_N$	nuclear kinetic energy operator
u	periodic potential
U	applied potential
V_{KS}	Kohn-Sham potential
$\widehat{V}_{ee}$	electron-electron Coulomb interaction operator
$\widehat{V}_{eN}$	electron-nucleus Coulomb interaction operator
V_{ext}	external potential
V_H	Hartree potential
$\widehat{V}_{NN}$	nucleus-nucleus Coulomb interaction operator
$\widehat{V}_x$	exchange potential operator
V_{xc}	exchange-correlation potential
w_i	Hirschfeld weight of atom i
Z_α	charge of nucleus α
∇^2	Laplacian operator

Chapter 1

Introduction

Context

This year, on August 2^{nd} 2017, we have used up all the resources from nature that our planet can renew in a whole year [42]. Worse still, every year the *Earth Overshoot Day* occurs a few days earlier. Although this is not the only cause, our dependence on fossil fuels and the resulting CO_2 emissions account for a major part in this issue. Fortunately, little by little renewable energy resources are gaining contribution in the global energy mix. However, these emerging technologies face major challenges towards a full transition to renewable energies. Wind and solar energies are intermittent sources and lack efficient storage means. Fuel cells, on the other hand, rely mainly on hydrogen, which is currently polluting to produce.

In this context, electrocatalysis offers a promising approach. Indeed, the water-splitting reaction enables to produce hydrogen from electricity. Other novel catalytic reactions enable to reduce CO_2 into hydrocarbon fuels. On the one hand, mastering this reaction would give humans the ability to control the CO_2 content in the atmosphere. On the other hand, because the hydrocarbon fuels would be produced from CO_2, the consumption of these fuels would release nothing more than the originally captured CO_2. As such, the generated fuels would have no additional CO_2 footprint when consumed.
In this work, we will mainly focus on two catalytic reactions. First, we investigate the oxygen evolution reaction, which is one of the half-reactions of the water-splitting reaction. Second, among the multiple hydrocarbons that can be generated from CO_2 reduction, it was chosen to focus on the CO_2 reduction to methane (CH_4).

However, these promising catalytic reactions still face major issues. A catalyst material needs to meet three important conditions to sustain a cost-effective process: (1) high selectivity towards desired products (2) high activity for the formation of the desired products and (3) high stability under reaction conditions [27]. To this date, no catalyst material satisfies these criteria to a sufficient extent. Indeed, both water-splitting and CO_2 reduction reactions require potentials over $1\,V$ on currently studied materials [49, 54, 55]. However, it has been shown that transition metal oxides exhibit interesting catalytic performances [8, 27, 55, 57].
Nonetheless, limited research has been preformed on these catalysts. It is in the scope of this work to further investigate rutile transition metal catalysts. More specifically, we focus on two specific materials: IrO_2 and RuO_2. Their performances and characteristics are confronted throughout this work.

Objectives

The objectives of the present thesis are twofold: on the one hand, investigate new intermediates which may play a role at low potential in the oxygen evolution reaction on both IrO_2 and RuO_2.

On the other hand, the feasibility of the CO_2 reduction reaction to methane is studied on these catalysts.

Towards this goal, we proceed through a step-by-step approach. First of all, two major parts can be distinguished: we start by giving a literature review before presenting the major simulation results.
In chapter 2, we establish the required theoretical background to understand computational material simulation. First, the Schrödinger equation and the Born-Oppenheimer approximation are introduced. The Hartree-Fock theory and the Density Functional Theory are built on this foundation. The chapter is closed with considerations on how to practically implement the Density Functional Theory in materials science simulation.
Chapter 3 follows with an overview of some basic concepts in electrocatalysis.
Next, in chapters 4 & 5 a literature review is given on the Oxygen Evolution Reaction and on the CO_2 Reduction Reaction respectively. Both catalyst materials (IrO_2 & RuO_2) and reaction mechanisms are discussed.

With this background, one should be able to interpret simulation results with a proper perspective. Chapter 7 reviews the simulations performed in the frame of the Oxygen Evolution Reaction. Therefore, standard results are first reproduced before extending the discussion to an analysis of other possible intermediates involved in this reaction, with a focus on low potentials.
Likewise, in chapter 8, major simulation results concerning the CO_2 Reduction Reaction are presented. Again, we first reproduce reference work before analyzing the full reaction pathway towards methane production. Both the IrO_2 and RuO_2 catalysts are confronted and different reaction mechanisms are compared.
Finally, chapter 9 provides the global conclusions of this thesis.

Part I

Literature review

Chapter 2

Theoretical background

Since the last few decades, materials science researchers have had a growing interest in computational methods. Indeed, as scales became smaller and smaller, experimental research became more complex and more expensive. Today, computational methods have become complementary to experimental research, enabling the prediction of a variety of physical and chemical properties.

In materials science, different types of computational methods can be distinguished. On the one hand, interatomic interactions can be described using classical force fields, such as Molecular Dynamics (MD), among others. On the other hand, interatomic interactions can be computed at the quantum mechanical level by solving Schrödinger's equation. The latter offers a much more accurate description, but at a much higher computational cost, which limits the number of atoms to be simulated. Among quantum mechanical methods, semi-empirical methods should be distinguished from first-principle methods. Whereas first-principle methods are based solely on quantum mechanics (*"ab initio": from the beginning*), semi-empirical methods rely partly on empirical data, for simplification purposes. Among the first-principle methods, different theories have been developed, such as the Densitiy Functional Theory (DFT), methods based on quantum chemistry (Hartree-Fock and post Hartree-Fock techniques) or the many-body perturbation theory.

In this chapter, an overview of the theoretical concepts required to understand DFT will be given. Therefore, we will first review the Schrödinger equation and the Born-Oppenheimer approximation. Next, the Hartree-Fock theory and the Density Functional Theory will be introduced to simplify the all-electron Schrödinger equation. At last, we will see how DFT can be practically implemented by reducing the amount of wavefunctions and electrons to treat.

All expressions given in this chapter are expressed in atomic units.

2.1 The Schrödinger equation

This section is mainly inspired from references [3, 4, 10, 15, 38].
A quantum mechanical system consisting of N_e electrons and N_N nuclei is completely described by its wavefunction Ψ:

$$\Psi = \Psi(\mathbf{r}_1, \mathbf{r}_2, ..., \mathbf{r}_{N_e}, \mathbf{R}_1, \mathbf{R}_2, ..., \mathbf{R}_{N_N}) \tag{2.1}$$

where $\mathbf{r}_i (i = 1, ..., N_e)$ and $\mathbf{R}_\alpha (\alpha = 1, ..., N_N)$ are the coordinates of the electrons and the nuclei respectively. The quantity $|\Psi|^2$ gives the probability density to find a certain configuration of electrons and nuclei. The purpose of quantum mechanical modelling is to determine this wavefunction as precisely as possible. This requires solving the Schrödinger equation:

$$\widehat{H}\Psi = E\Psi \tag{2.2}$$

where E is the energy and the Hamiltonian $\widehat{H}$ is given by:

$$\widehat{H} = \widehat{T}_e + \widehat{T}_N + \widehat{V}_{ee} + \widehat{V}_{eN} + \widehat{V}_{NN} \tag{2.3}$$

with:

$$\widehat{T}_e = \sum_{i=1}^{N_e} -\frac{1}{2}\nabla_{\mathbf{r}_i}^2 \qquad \text{electronic kinetic energy}$$

$$\widehat{T}_N = \sum_{\alpha=1}^{N_N} -\frac{1}{2M_\alpha}\nabla_{\mathbf{R}_\alpha}^2 \qquad \text{nuclear kinetic energy}$$

$$\widehat{V}_{ee} = \sum_{\substack{i,j \\ i<j}}^{N_e,N_e} \frac{1}{|\mathbf{r}_i - \mathbf{r}_j|} \qquad \text{electron-electron Coulomb interaction}$$

$$\widehat{V}_{eN} = \sum_{i=1}^{N_e}\sum_{\alpha=1}^{N_N} \frac{-Z_\alpha}{|\mathbf{r}_i - \mathbf{R}_\beta|} \qquad \text{electron-nucleus Coulomb interaction}$$

$$\widehat{V}_{NN} = \sum_{\substack{\alpha,\beta \\ \alpha<\beta}}^{N_N,N_N} \frac{Z_\alpha Z_\beta}{|\mathbf{R}_\alpha - \mathbf{R}_\beta|} \qquad \text{nucleus-nucleus Coulomb interaction}$$

where M_α and Z_α are the mass and the atomic number of nucleus α respectively.

2.2 The Born-Oppenheimer approximation

This section was inspired from references [3, 4].

The Born-Oppenheimer approximation is based on the observation that nuclei are much heavier than electrons ($M_\alpha >> 1$). Therefore, the electrons virtually instantaneously adapt their position to any movement of the nuclei. Based on this consideration, the Born-Oppenheimer approximation states that the dynamics of the electrons and nuclei can be decoupled. Hence, the wavefunction (equation 2.1) can be expressed as a function of its electronic (ψ) and nuclear (ψ^N) components:

$$\Psi = \psi(\mathbf{r}_1, \mathbf{r}_2, ..., \mathbf{r}_{N_e}) \times \psi^N(\mathbf{R}_1, \mathbf{R}_2, ..., \mathbf{R}_{N_N}) \tag{2.4}$$

In practice, the nuclei are considered as fixed when studying the electrons. Therefore, the system can be simplified to N_e interacting electrons in an external potential $V_{ext}(\mathbf{r})$ generated by the nuclei.
Hence, the wavefunction Ψ simplifies to:

$$\psi = \psi(\mathbf{r}_1, \mathbf{r}_2, ..., \mathbf{r}_{N_e}) \tag{2.5}$$

and the Hamiltonian to:

$$\widehat{H} = \widehat{T}_e + \widehat{V}_{eN} + \widehat{V}_{ee} \tag{2.6}$$

Thus, the Schrödinger equation simplifies to:

$$\widehat{H}\psi = \sum_i \left(-\frac{1}{2}\nabla_i^2 + V_{ext}(\mathbf{r}_i) + \sum_{i<j} \frac{1}{\mathbf{r}_i - \mathbf{r}_j} \right) \psi = E\psi \tag{2.7}$$

However, even this simplified Schrödinger equation is impossible to solve analytically for systems with more than two electrons. This is the so-called many-body problem. Numerous methods

were developed to circumvent this problem and solve the equation by approximating the electron interactions. Among others, we can cite the Hartree-Fock theory (HF) and the Density Functional Theory (DFT), which will be discussed in the next sections.

2.3 Hartree-Fock theory

This section is mainly based on references [3, 4, 38]. First, Hartree developed a theory to approximate the Schrödinger equation (section 2.3.1). Then this theory was further refined to include the Pauli exclusion principle, giving rise to the Hartree-Fock theory (section 2.3.2).

2.3.1 Hartree method

In order to simplify equation 2.7, Hartree proposed to replace the electron-electron interactions by an averaged potential. As such, instead of dealing with a numerous amount of electron-electron interactions, only interactions between each electron and an averaged field must be taken into account. Equation 2.7 then simplifies to:

$$\hat{H}\psi = \sum_i \left(-\frac{1}{2}\nabla_i^2 + V_{ext}(\mathbf{r}_i) + V_H(\mathbf{r}_i) \right) \psi = E\psi \tag{2.8}$$

where V_{ext} represents the interaction between electrons and nuclei and V_H is the Hartree potential, expressing a repulsive Coulomb interaction between electrons and an averaged field. It can be shown that this Hartree potential is given by [4]:

$$V_H(\mathbf{r}) = \int \frac{n(\mathbf{r}')}{|\mathbf{r} - \mathbf{r}'|} d\mathbf{r}' \tag{2.9}$$

where $n(\mathbf{r}) = \sum_n |\phi_n(\mathbf{r})|^2$ is defined as the electronic density.

Due to the form of equation 2.8, the electrons can be treated independently. The N_e-electron wavefunction can then be replaced by the product of N_e 1-electron wavefunctions:

$$\psi(\mathbf{r}_1, \mathbf{r}_2, ..., \mathbf{r}_{N_e}) = \phi_1(\mathbf{r}_1)\phi_2(\mathbf{r}_2)...\phi_{N_e}(\mathbf{r}_{N_e}) \tag{2.10}$$

With this description, Hartree introduced the so-called *Self-Consistent Field* method (SCF). Indeed, to obtain the Hartree potential $V_H(\mathbf{r})$, the electronic density $n(\mathbf{r})$ and hence all the wavefunctions $\phi_i(\mathbf{r})$ must be known. However, to obtain the wavefunctions $\phi_i(\mathbf{r})$, the Hartree potential $V_H(\mathbf{r})$ is needed. Therefore, one starts from a trial electronic density and iterates until self-consistency is reached. The procedure is depicted in figure 2.1.

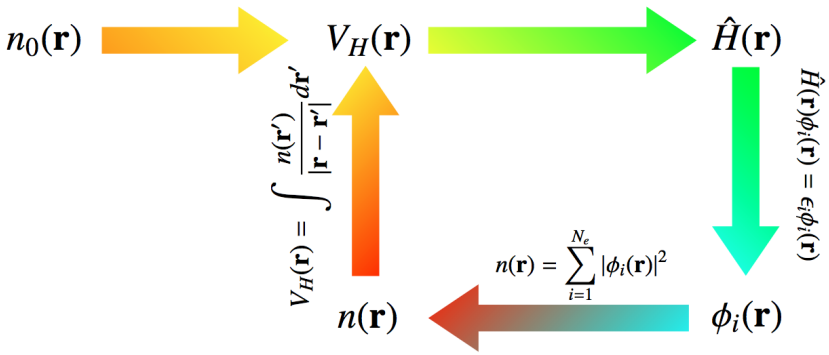

Figure 2.1: Self-Consistent Field (SCF) method [4].

However, this method is a rough approximation because it does not take into account Pauli's exclusion principle and the description of electron interaction is quite poor. Therefore, the Hartree method was refined into the Hartree-Fock method.

2.3.2 Hartree-Fock method

In order to satisfy the Pauli exclusion principle, Fock developed the wavefunction expression ψ as a linear combination of non-interacting one-electron wavefunctions ϕ, represented as the so-called *Slater determinant* given by:

$$\psi(\mathbf{r}_1, \mathbf{r}_2, ..., \mathbf{r}_{N_e}) = \frac{1}{\sqrt{!N_e}} \begin{vmatrix} \phi_1(\mathbf{r}_1) & \phi_2(\mathbf{r}_1) & \cdots & \phi_{N_e}(\mathbf{r}_1) \\ \phi_1(\mathbf{r}_2) & \phi_2(\mathbf{r}_2) & \cdots & \phi_{N_e}(\mathbf{r}_2) \\ \vdots & \vdots & \ddots & \vdots \\ \phi_1(\mathbf{r}_{N_e}) & \phi_2(\mathbf{r}_{N_e}) & \cdots & \phi N_e(\mathbf{r}_{N_e}) \end{vmatrix} \tag{2.11}$$

In order to fulfill the antisymmetry principle, two electrons must satisfy the following relation:

$$\psi(\mathbf{r}_1, \mathbf{r}_2) = -\psi(\mathbf{r}_2, \mathbf{r}_1)$$

In an N_e-electron system, this condition is exactly expressed by the Slater determinant. Indeed, when two rows or columns are exchanged, the determinant sign will change too. Moreover, any determinant which has two identical rows or columns will be equal to zero. This expresses the fact that a wavefunction where two electrons occupy the same spin cannot exist, which is exactly what Pauli's exclusion principle states.
There only exists one minimal ground-state energy in a system without degenerated states. Therefore, the variational principle states that by minimizing the system energy with respect to the wavefunction, one will eventually reach the ground-state energy. Without entering into too many details, it can be shown that the 1-electron Schrödinger equation can be rewritten as:

$$\left[-\frac{1}{2}\nabla^2 + V_{ext}(\mathbf{r}) + \sum_{j \neq i} (\widehat{J}_j - \widehat{K}_j) \right] \phi_i(\mathbf{r}) = \varepsilon_i^{HF} \phi_i(\mathbf{r}) \tag{2.12}$$

where $\widehat{J}_j$ is the *Coulomb operator*:

$$\widehat{J}_j \phi_i(\mathbf{r}) = \int \frac{\phi_j^*(\mathbf{r}')\phi_j(\mathbf{r}')}{|\mathbf{r} - \mathbf{r}'|} d\mathbf{r}' \phi_i(\mathbf{r}),$$

$\widehat{K}_j$ is the *exchange operator*:

$$\widehat{K}_j \phi_i(\mathbf{r}) = \int \frac{\phi_j^*(\mathbf{r}')\phi_i(\mathbf{r}')}{|\mathbf{r} - \mathbf{r}'|} d\mathbf{r}' \phi_j(\mathbf{r})$$

and ε_i^{HF} are the electronic eigenenergies.
Finally, it can be shown that equation 2.12 is identical to:

$$\left[-\frac{1}{2}\nabla^2 + V_{ext}(\mathbf{r}) + V_H(\mathbf{r}) + \widehat{V}_x \right] \phi_i(\mathbf{r}) = \varepsilon_i^{HF} \phi_i(\mathbf{r}) \tag{2.13}$$

with $\widehat{V}_x$ the *exchange potential* given by:

$$\widehat{V}_x \phi_i(\mathbf{r}) = \sum_j \left\{ \int \frac{\phi_j^*(\mathbf{r}')\phi_i(\mathbf{r}')}{|\mathbf{r} - \mathbf{r}'|} d\mathbf{r}' \right\} \phi_j(\mathbf{r})$$

Here also the Schrödinger equation should be solved with the *Self-Consistent Field* procedure described above.
Using the orthonormalization constraint, the energy of the system can be expressed as:

$$E = \langle \psi | \widehat{H} | \psi \rangle = \sum_{i,j} \int \psi_i^*(\mathbf{r}) \left[-\frac{1}{2}\nabla^2 + V_{ext}(\mathbf{r}) + V_H(\mathbf{r}) + \widehat{V}_x \right] \psi_i(\mathbf{r}) d\mathbf{r} \tag{2.14}$$

Although the Hartree-Fock method shows significant improvement compared to the Hartree method, the above described procedure still has some shortcomings. Indeed, including the Slater determinant fulfilled the antisymmetry requirement, according to which same-spin electrons repel each other (exchange interaction). However, opposite-spin electrons also have a tendency to stay away from each other because they bear the same charge. This effect is called *correlation* and is not accounted for in the Hartree-Fock method. Therefore, the band gaps often appear too wide and the band widths too narrow.
To compensate for these shortcomings, post Hartree-Fock methods were developed, which try to include correlation. However, the real breakthrough was only achieved with the *Density Functional Theory* (DFT), described in the next section.

2.4 Density Functional Theory

This section is mainly based on references [4, 10, 15, 38].

In an attempt to enhance the Hartree-Fock method for computing wavefunctions, Hohenberg, Kohn and Sham placed the foundations of the *Density Functional Theory*. In this approach, the focus is not placed directly on the wavefunction, like it is the case for the HF method, but instead on the electron density. First, Hohenberg and Kohn demonstrated how the electron density could be linked back to the wavefunction. They established an expression for a universal functional of the density. Next, Kohn and Sham developed a methodology to compute this density functional.

2.4.1 Hohenberg-Kohn theorems

Let us recall the simplified Schrödinger equation for N_e electrons (equation 2.7):

$$\widehat{H}\psi = \sum_i \left(-\frac{1}{2}\nabla_i^2 + V_{ext}(\mathbf{r}_i) + \sum_{i<j} \frac{1}{\mathbf{r}_i - \mathbf{r}_j} \right) \psi = E\psi \tag{2.15}$$

1st Hohenberg-Kohn theorem: There is a unique external potential $V_{ext}(\mathbf{r})$ (modulo a global constant) determined solely by the ground-state electron density, given by:

$$n(\mathbf{r}) = N_e \int [\psi(\mathbf{r}, \mathbf{r}_2, ..., \mathbf{r}_{N_e})]^* \psi(\mathbf{r}, \mathbf{r}_2, ..., \mathbf{r}_{N_e}) d\mathbf{r}_2 ... \mathbf{r}_{N_e} \tag{2.16}$$

More specifically, it can be proven that the external potential is a functional of the ground-state density.

2nd Hohenberg-Kohn theorem: At a given external potential $V_{ext}(\mathbf{r})$, minimizing the system energy by varying the electron density will eventually lead to the ground-state energy. This second theorem is introducing a variational principle for DFT, although it restricts the theory to ground states.

By combining these theorems, it is possible to gain insight about the energy functional:

$$E = \min_{\phi} \left\{ \langle \phi | \widehat{H} | \phi \rangle \right\} = \min_n \left\{ \min_{\phi \to n} \left\{ \langle \phi | \widehat{H} | \phi \rangle \right\} \right\} \tag{2.17}$$

$$= \min_n \left\{ \min_{\phi \to n} \left\{ \langle \phi | \widehat{T}_e + \widehat{V}_{ee} + \sum_{i=1}^{N_e} V_{ext}(\mathbf{r}_i) | \phi \rangle \right\} \right\} \tag{2.18}$$

$$= \min_n \left\{ \min_{\phi \to n} \left\{ \langle \phi | \widehat{T}_e + \widehat{V}_{ee} | \phi \rangle \right\} + \int n(\mathbf{r}) V_{ext}(\mathbf{r}) d\mathbf{r} \right\} \tag{2.19}$$

$$= \min_n \left\{ F[n] + \int n(\mathbf{r}) V_{ext}(\mathbf{r}) d\mathbf{r} \right\} \tag{2.20}$$

where $F[n] = \min_{\phi \to n} \left\{ \langle \phi | \widehat{T}_e + \widehat{V}_{ee} | \phi \rangle \right\}$ is a universal functional of the density, but is not known explicitly. This functional represents an important part of the total electronic energy and it is thus crucial to make a reasonable approximation for it. For the first time, Kohn and Sham managed to propose an accurate description for this functional, which will be presented in the next section.

2.4.2 Kohn-Sham equation

At this point, let us first recall the expression of the energy as given by the HF theory (equation 2.14), which we will simplify to:

$$E[n] = E_{kin}[n] + E_{ext}[n] + E_H[n] + E_x[n] \tag{2.21}$$

with:

$E_{kin}[n]$:	kinetic energy of the electrons
$E_{ext}[n]$:	interaction energy between electrons and an external potential generated by the nuclei
$E_H[n]$:	Hartree energy, interaction between single electrons and an averaged electron field
$E_x[n]$:	exchange potential accounting for same-spin electron repulsion (Pauli's principle)

To determine the density functional $F[n]$, Kohn and Sham first assumed that the electrons are non-interacting. Then, the N_e-electron system was substituted by a system of N_e non-interacting 1-electrons, subjected to the external potential. This was implemented through the definition of a so-called exchange-correlation energy functional $E_{xc}[n]$:

$$E_{xc}[n] = F[n] - T_0[n] - E_H[n] \tag{2.22}$$

where $T_0[n] = \min_{\phi \to i} \left\{ \langle \phi | \widehat{T}_e | \phi \rangle \right\}$ is a known kinetic energy functional of the non-interacting electrons.

As its name suggests, the exchange-correlation energy functional $E_{xc}[n]$ contains an exchange term (repulsion of same-spin electrons) and a correlation term (repulsion of opposite-spin electrons). Nonetheless, it also contains the difference between the kinetic energy of the fictitiously non-interacting electron gas ($T_0[n]$) and the real one. Substituting equation 2.22 in equation 2.20 gives:

$$E[n] = \min_n \left\{ F[n] + \int n(\mathbf{r}) V_{ext}(\mathbf{r}) d\mathbf{r} \right\} \tag{2.23}$$

$$= \min_n \left\{ T_0[n] + \int n(\mathbf{r}) V_{ext}(\mathbf{r}) d\mathbf{r} + E_H[n] + E_{xc}[n] \right\} \tag{2.24}$$

$$= \min_n \left\{ T_0[n] + \int n(\mathbf{r}) V_{ext}(\mathbf{r}) d\mathbf{r} + \frac{1}{2} \int \frac{n(\mathbf{r}) n(\mathbf{r}')}{|\mathbf{r} - \mathbf{r}'|} d\mathbf{r} d\mathbf{r}' + E_{xc}[n] \right\} \tag{2.25}$$

Under the constraint of a fixed number of electrons, and by introducing the Lagrange multipliers, it can be shown that this energy is equivalent to that a system of non-interacting electrons with the same electronic density in an external potential, called the *Kohn-Sham* potential:

$$V_{KS}(\mathbf{r}) = V_{ext}(\mathbf{r}) + V_H(\mathbf{r}) + V_{xc}(\mathbf{r}) \tag{2.26}$$

with $V_{xc}(\mathbf{r})$ the *exchange-correlation* potential. This Kohn-Sham potential corresponds to a fictitious system of non-interacting electrons, but will generate the same density as a system of interacting electrons.

The wavefunction can be found by solving the following 1-electron Schrödinger equation (also called KS equation) self-consistently:

$$\widehat{H}_{KS} \phi_i^{KS}(\mathbf{r}) = \varepsilon_i^{KS} \phi_i^{KS}(\mathbf{r}) \tag{2.27}$$

$$\left[-\frac{1}{2} \nabla^2 + V_{KS}(\mathbf{r}) \right] \phi_i^{KS}(\mathbf{r}) = \varepsilon_i^{KS} \phi_i^{KS}(\mathbf{r}) \tag{2.28}$$

with the electronic density defined as $n(\mathbf{r}) = \sum_{i=1}^{N} |\phi_n^{KS}(\mathbf{r})|^2$.
Although this corresponds to solving a fictitious system, over time the 1-electron reformulation has proven to approximate reality very accurately.

2.4.3 Exchange-correlation functionals

So far, it has been assumed that the exchange-correlation energy functional $E_{xc}[n]$ was known. However, the problem of correctly approximating this functional still remains. Two approaches for doing this will be presented here: the *Local Density Approximation* and the *Generalized Gradients Approximation*. At last, dispersion corrections will be discussed.

Local Density Approximation

The *Local Density Approximation* (LDA) [28] relies on the assumption that an electron is subjected to a local electron density which is similar to the global electron density. The exchange-correlation energy can then be expressed as:

$$E_{xc}[n] = \int n(\mathbf{r})\varepsilon_{xc}(\mathbf{r}, n)d\mathbf{r} \tag{2.29}$$

where $\varepsilon_{xc}(\mathbf{r}, n)$ is the local exchange-correlation energy per electron. Then, the overall system is divided into several subsystems, each with a different constant local electron density. In LDA, this local electron density is equal to that of a homogeneous electron gas with the same density (in a neutralizing background called "the jellium"):

$$\varepsilon_{xc}^{LDA}(\mathbf{r}, n) = \varepsilon_{xc}^{hom}(n(\mathbf{r})) \tag{2.30}$$

The exchange component ε_x can be calculated analytically using the HF method:

$$\varepsilon_x^{LDA}(\mathbf{r}, n) = -\frac{3}{4\pi}[3\pi^2 n((\mathbf{r})]^{1/3} \tag{2.31}$$

The correlation component ε_c, on the other hand, is obtained numerically from quantum Monte Carlo simulations.
The LDA generally gives an accurate approximation for systems where the charge density varies relatively slowly, such as in covalent systems and simple metals. However, LDA overestimates adsorption energies and is not adequate for strongly correlated systems, such as transition metals (strong electron localization with narrow d- and f- bands). These are better described by the *Generalized Gradients Approximation*, which will be described in the next section.

Generalized Gradient Approximation

The fundamental idea behind the *Generalized Gradient Approximation* (GGA) [47] is identical to LDA in the sense that the global electron density is approximated by a local density. However, GGA tries to push further by including a dependence on the gradient of the local density:

$$E_{xc}^{GGA}[n] = \int n(\mathbf{r})\varepsilon_{xc}^{GGA}[n(\mathbf{r}), |\nabla n(\mathbf{r})|]d\mathbf{r} \tag{2.32}$$

Different variants of GGA were developed such as PW91 [47] , PBE [46], revised PBE (RPBE) [17] etc. PBE has now become one of the most used functionals. The revised version of PBE uses a simpler mathematical form for the exchange energy component ε_{xc}.

Finally let us note that although DFT generally accurately approximates experimental data, the band gap energy remains a prominent exception as it is systematically underestimated in both LDA and GGA.

Van der Waals interactions

A contribution both LDA and GGA functionals are missing are the van der Waals (vdW) interactions, resulting from dynamical correlations between fluctuating charge distributions. To fulfill this shortcoming, a dispersion correction term can be added to the conventional Kohn-Sham DFT energy E_{KS-DFT} [34]:

$$E_{DFT-disp} = E_{KS-DFT} + E_{disp} \tag{2.33}$$

There exist multiple methods to compute the correction term E_{disp}.

The DFT-D2 method developed by Grimme [11] expressed E_{disp} as follows:

$$E_{disp} = -\frac{1}{2}\sum_{i=1}^{N_{at}}\sum_{j=1}^{N_{at}}\sum_{\mathbf{L}}{}' \frac{C_{6ij}}{r_{ij,L}^6} f_{d,6}(r_{ij}, L) \tag{2.34}$$

where summations are over all atoms N_{at} and all translations of the unit cell $L = (l_1, l_2, l_3)$. The prime indicates that $i \neq j$ for $L = 0$, C_{6ij} is the dispersion coefficient for atom pair ij and $r_{ij,L}$ is the distance between atoms i and j in unit cell L. $f(r_{ij})$ is the damping function given by [11]:

$$f_{d,6}(r_{ij}) = \frac{s_6}{1 + e^{-d(r_{ij}/(s_R R_{0ij})-1)}} \tag{2.35}$$

where s_6 and s_R are parameters optimized for different DFT functionals. This damping function scales the force fields in order to minimize contributions from interactions within typical bonding distances and thus determines the short-range behaviour of the dispersion correction [13, 34]. In practice, interactions over distances larger than a chosen cutoff radius can be ignored. C_{6ij} and R_{0ij} are computed using the following combination rules:

$$C_{6ij} = \sqrt{C_{6ii} C_{6jj}} \tag{2.36}$$

$$R_{0ij} = R_{0i} + R_{0j} \tag{2.37}$$

The greatest shortcoming of the DFT-D2 scheme is that the dispersion coefficients are computed for each pair of atoms and are thus insensitive to an atom's chemical environment. In contrast, in the DFT-D3 method [12], the dispersion coefficients C_{6ij} are geometry-dependent. They are adjusted based on the local geometry (coordination number) around atoms i and j.

The correction term E_{disp} for the DFT-D3 method is expressed as [12]:

$$E_{disp} = -\frac{1}{2}\sum_{i=1}^{N_{at}}\sum_{j=1}^{N_{at}}\sum_{\mathbf{L}}{}' \left(f_{d,6}(r_{ij}, L)\frac{C_{6ij}}{r_{ij,L}^6} + f_{d,8}(r_{ij}, L)\frac{C_{8ij}}{r_{ij,L}^8} \right) \tag{2.38}$$

Finally, the DFT-TS (Tkatchenko-Scheffler) method [58] is based on the DFT-D2 method, but includes a charge-density dependency. This enables to take into account variations in vdW contributions according to atoms' chemical environments. In this method, polarizability (α_i), dispersion coefficients (C_{6ii}) and atomic radii of atoms (R_{0i}) are computed from their free energy values using the following relationships:

$$\alpha_i = \nu_i \alpha_i^{free} \tag{2.39}$$

$$C_{6ii} = \nu_i^2 C_{6ii}^{free} \tag{2.40}$$

$$R_{0i} = \left(\frac{\alpha_i}{\alpha_i^{free}}\right)^{\frac{1}{3}} R_{0i}^{free} \tag{2.41}$$

ν_i are the free atomic volumes computed using the Hirschfeld partitioning of the all-electron density:

$$\nu_i = \frac{\int r^3 w_i(\mathbf{r}) n(\mathbf{r}) d^3\mathbf{r}}{\int r^3 n_i^{free}(\mathbf{r}) d^3\mathbf{r}} \tag{2.42}$$

with $n(\mathbf{r})$ the total electron density, $n_i^{free}(\mathbf{r})$ the spherically averaged electron density of the neutral free atomic species i and $w_i(\mathbf{r})$ the Hirshfeld weight defined by free atomic densities as:

$$w_i(\mathbf{r}) = \frac{n_i^{free}(\mathbf{r})}{\sum_{j=1}^{N_{at}} n_j^{free}(\mathbf{r})} \tag{2.43}$$

The combination rules to compute C_{6ij} and R_{0ij} using the DFT-TS method are given by:

$$C_{6ij} = \frac{2C_{6ii}C_{6jj}}{\frac{\alpha_j}{\alpha_i}C_{6ii} + \frac{\alpha_i}{\alpha_j}C_{6jj}} \tag{2.44}$$

$$R_{0ij} = R_{0i} + R_{0j} \tag{2.45}$$

2.5 Practical implementation

This section is based on references [3, 4, 38].

Although DFT is a considerable step forward towards materials science simulation, the amount of data to be treated is still tremendous. In this section, we will see how the properties of solids can be exploited to significantly reduce the computational load.

2.5.1 Plane-wave basis set

In this section, we will see how wavefunctions can be described using plane waves.

The smallest subset in a lattice structure allowing to fully reconstruct a solid is called a unit cell or primitive cell. The full crystal structure can be recovered by periodic repetition of this unit cell along a vector $\mathbf{R} = u\mathbf{a_1} + v\mathbf{a_2} + w\mathbf{a_3}$ with $\mathbf{a_1}$, $\mathbf{a_2}$, $\mathbf{a_3}$ the primitive vectors of the real lattice and u, v, w integers. On the other hand, the reciprocal lattice is defined such that the plane waves with wave vector $\mathbf{G}$ have the same periodicity as the real lattice, where $\mathbf{G} = u\mathbf{b_1} + v\mathbf{b_2} + w\mathbf{b_3}$ with $\mathbf{b_1}$, $\mathbf{b_2}$, $\mathbf{b_3}$ the primitive vectors of the reciprocal lattice and u, v, w integers. Both lattices are represented conceptually in figure 2.2 and their lattice vectors are related by:

$$e^{i\mathbf{G}\cdot\mathbf{R}} = 1 \tag{2.46}$$

The real and reciprocal lattice volumes are given by: $\Omega = a_1 \cdot (a_2 \times a_3)$ and $\Omega^* = b_1 \cdot (b_2 \times b_3)$ respectively. Their volumes are related by: $\Omega^* = (2\pi)^3/\Omega$. The primitive vectors in the real and reciprocal space are linked by:

$$b_1 = \tfrac{2\pi}{\Omega}(a_2 \times a_3) \quad b_2 = \tfrac{2\pi}{\Omega}(a_3 \times a_1) \quad b_3 = \tfrac{2\pi}{\Omega}(a_1 \times a_2)$$

Because the lattice points of the reciprocal lattice define the allowed wave vectors, this reciprocal lattice is more convenient for representing wave functions. Notice that the magnitude of real and reciprocal lattice primitive vectors are inversed.

According to Bloch's theorem, a wavefunction $\phi_{n\mathbf{k}}$ with wave vector $\mathbf{k}$ and band index n, in a system with a periodic potential $V(\mathbf{r}) = V(\mathbf{r} + \mathbf{R})$ can be represented as:

$$\phi_{n\mathbf{k}}(\mathbf{r}) = e^{i\mathbf{k}\cdot\mathbf{r}} u_{n\mathbf{k}}(\mathbf{r}) \tag{2.47}$$

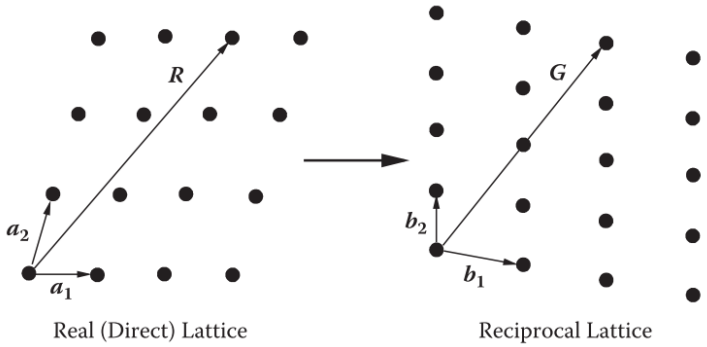

Figure 2.2: Representation of a real and reciprocal lattice. A real lattice vector $\mathbf{R}$ and a reciprocal lattice vector $\mathbf{G}$ are also shown [38].

where:

$$u_{n\mathbf{k}}(\mathbf{r}+\mathbf{R}) = u_{n\mathbf{k}}(\mathbf{r}) \tag{2.48}$$

$$\phi_{n\mathbf{k}}(\mathbf{r}+\mathbf{R}) = e^{i\mathbf{k}\cdot\mathbf{r}}\phi_{n\mathbf{k}}(\mathbf{r}) \tag{2.49}$$

As such, Bloch represents wavefunctions as a superposition of a plane wave $e^{i\mathbf{k}\cdot\mathbf{r}}$ and a periodical potential $u_{n\mathbf{k}}(\mathbf{r})$. This is represented schematically in figure 2.3.

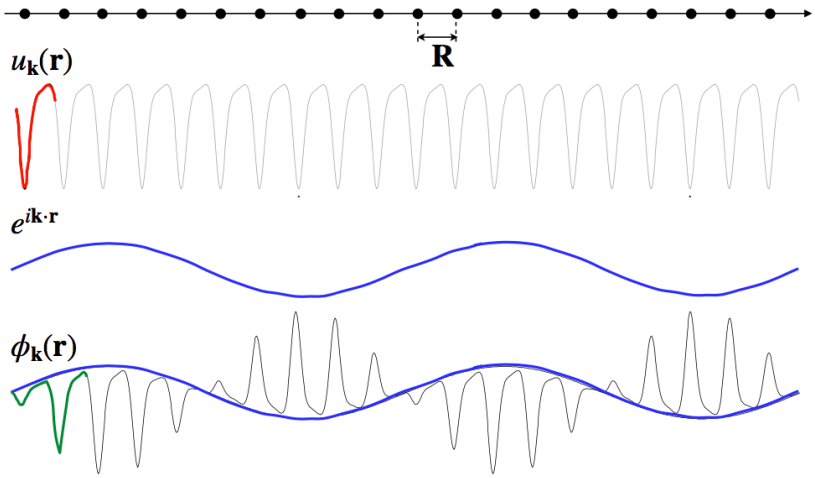

Figure 2.3: Representation of wavefunctions $\phi_{\mathbf{k}}(\mathbf{r})$ as a superposition of a plane wave $e^{i\mathbf{k}\cdot\mathbf{r}}$ and a periodical potential $u_{n\mathbf{k}}(\mathbf{r})$ according to Bloch's theorem [4].

By using the following Fourrier transforms:

$$u_{n\mathbf{k}}(\mathbf{G}) = \frac{1}{\Omega}\int_{\Omega} u_{n\mathbf{k}}(\mathbf{r})e^{-i\mathbf{G}\cdot\mathbf{r}}d\mathbf{r} \tag{2.50}$$

$$\phi_{n\mathbf{k}}(\mathbf{r}) = \sum_{G} u_{n\mathbf{k}}(\mathbf{G})e^{i(\mathbf{k}+\mathbf{G})\cdot\mathbf{r}} \tag{2.51}$$

the periodic potential $u_{n\mathbf{k}}(\mathbf{r})$ can be rewritten as:

$$u_{n\mathbf{k}}(\mathbf{r}) = \sum_{G} u_{n\mathbf{k}}(\mathbf{G})e^{i\mathbf{G}\cdot\mathbf{r}} \tag{2.52}$$

Finally, the wavefunctions can be rewritten as:

$$\phi_{n\mathbf{k}}(\mathbf{r}) = \frac{1}{\sqrt{N\Omega}}\sum_{G} u_{n\mathbf{k}}(\mathbf{G})e^{i(\mathbf{k}+\mathbf{G})\cdot\mathbf{r}} \tag{2.53}$$

where N is the number of unit cells repeated in the Born-von Karman periodic box.

In principle, this basis set for the expansion to represent a wavefunction is infinite. However, in numerical simulations it is impossible to take into account an infinite number of plane waves. Fortunately, the higher an electron's kinetic energy, the lower its contribution to total energy of the system. Therefore, we can introduce an upper limit to the kinetic energy of plane waves to be taken into account in the computation of the wave function. This upper limit is called the cutoff energy E_{cut} defined as:

$$E_{cut} \geq \frac{1}{2}(\mathbf{k} + \mathbf{G})^2 \tag{2.54}$$

Plane waves represent a very convenient basis set for expansion of Kohn-Sham orbitals. Indeed, the Fourrier transform significantly facilitates computations in the reciprocal space. However, despite introducing a cutoff energy, this approach requires a large amount of plane waves per atom. In the next two sections, we will see how we can further reduce the amount of plane waves to compute.

2.5.2 Brillouin zone sampling

In this section, we will see how the periodicity of solids make it possible to drastically reduce the quantity of atoms to handle without compromising the accuracy of the simulation.

First, a *supercell* is selected, consisting in a number of unit cells. A supercell is used instead of a unit cell in order to be able to represent defects, adsorbates etc. at any desired repetition throughout the material. Its size is critical when it comes to reducing interaction between particles or defects. This supercell can then be replicated periodically in all dimensions by using the periodic boundary conditions to represent a bulk material. The supercell approach can be extended to represent slabs or clusters.

The first *Brillouin zone* (BZ) is a uniquely defined primitive cell in reciprocal space. It corresponds to the volume defined by the three primitive reciprocal vectors Ω^*. Symmetry operations such as rotations and inversions can further reduce the first Brillouin zone to the *Irreducible Brillouin zone* (IBZ). In practice, for many properties integrals over the whole IBZ are necessary. This requires to evaluate the wavefunction for an infinite number of k-points, which is impossible. Fortunately, in most cases the k-points vary smoothly over the IBZ. Therefore, the integral is replaced by a sum over a restricted set of well-chosen k-points. This is called the *k-points* sampling. It is a crucial step as it should contain as few k-points as possible in order to reduce calculation size, but still enough k-points to adequately represent the system. The Monkhorst-Pack method [45] was developed to efficiently perform k-point sampling. It generates an evenly spaced k-point grid within the IBZ. The Γ-Point method is a specific case of this method where the k-point grid is concentrated around one, high-weighted and non-shifted point: the Γ-point (k=0). Using high symmetry around this point enables to further reduce computation time.
Figure 2.4 gives a schematic overview of the methods described above to scale down the simulation size of a bulk material from thousands of atoms to just a handful of k-points.

2.5.3 Pseudopotential approach

In this section, we will show how pseudopotentials enable to reduce the amount of electrons to be treated and therefore the amount of plane waves. Unlike valence electrons that participate to bonding, core electrons are highly localized and have only little influence on the overall material properties of a solid. In this perspective, the *frozen-core approximation* consists in smoothing out the "core" of an atom (nucleus & core electrons) and considering it as a constant non-polarizable

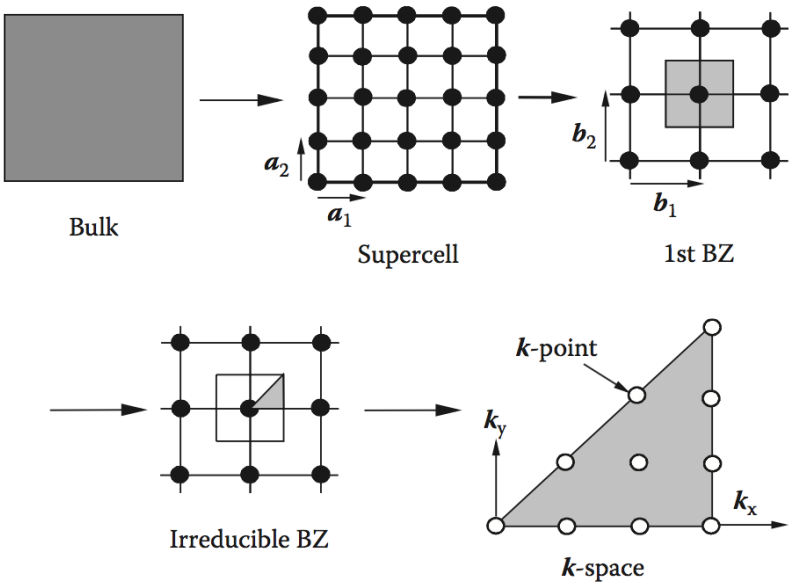

Figure 2.4: Overview of approaches used for scaling down calculation load when treating solids [38].

ion core. As such, only the valence electrons need to be considered. The pseudopotential (PP) approach goes further by pseudizing the valence electrons, which is the parameterization of the pseudopotential from a reference state. More specifically, an all-electron (AE) calculation is performed for an atom at a reference energy. Then, a cutoff radius r_c is set such that the pseudo- and all-electron valence eigenstates have the same energies and amplitude (and thus density) outside r_c [66]. This pseudization procedure also enables to soften out the wiggles of wavefunctions in the core region. These wiggles result from the orthogonality criterion and are depicted in figure 2.5. From there, a simplified pseudo-wavefunction is constructed. Hence, the system can be reduced to a restricted amount of pseudo-wavefunctions describing the valence electrons inside a pseudopotential approximating the atomic core. This approach provides numerous benefits such as the reduction of the amount of plane-waves required or the reduction of computational load.
According to this formalism, the KS equation can be rewritten as:

$$\left[-\frac{1}{2}\nabla^2 + V_{PP}(\mathbf{r})\right]\phi_i^{PP}(\mathbf{r}) = \varepsilon_i^{PP}\phi_i^{PP}(\mathbf{r}) \tag{2.55}$$

with the electronic density $n(\mathbf{r}) = \sum_{i=1}^{N} |\phi_n^{PP}(\mathbf{r})|^2$.

There exist different types of pseudopotentials among which we can name norm-conserving and ultrasoft pseudopotentials.
Norm-conserving pseudopotentials (NC-PP) [16, 59] are constructed such that the norm of each pseudo-wavefunction inside the cut-off radius is equal to its corresponding all-electron (AE) wavefunction.

$$\int_0^{r_c} |\phi_i^{PP}(\mathbf{r})|^2 d\mathbf{r} = \int_0^{r_c} |\phi_i^{AE}(\mathbf{r})|^2 d\mathbf{r}$$

This condition states that the charge within the cut-off radius r_c is fixed.
Ultrasoft pseudopotentials (US-PP) [61] relax the NC-PP condition to further reduce the required basis set. This is done by splitting the pseudo wavefunctions into two parts: an ultrasoft valence wavefunction that does not fulfill the norm conservation criterion ($\phi_i^{US}(\mathbf{r})$) plus a core augmentation charge (to fill in the charge deficit in the core region).

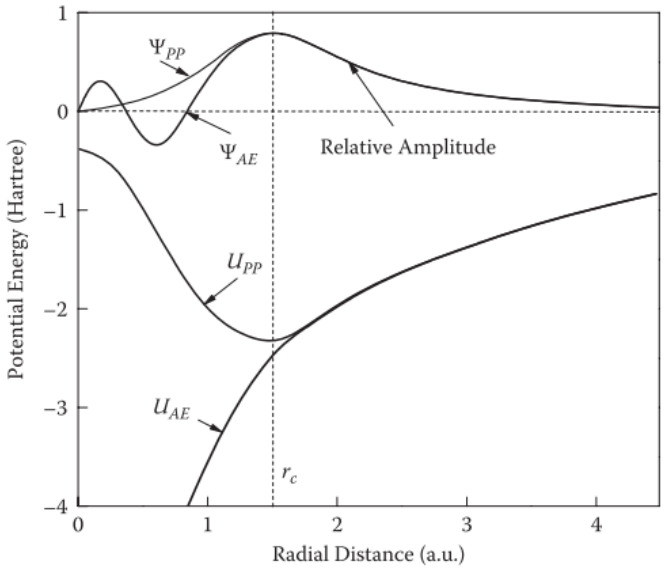

Figure 2.5: Schematic of a pseudo- and all-electron wavefunction with their corresponding pseudo- and all-electron potentials. At $r \leq r_c$ the pseudo- and all-electron wavefunctions coincide [38].

The *Projector-augmented wave method* (PAW) [30] is strictly speaking not a pseudopotential approach. It is a generalization of the pseudopotential and linear-augmented-wave methods [65]. By combining parts of both core wavefunctions and valence wavefunctions, it aims to reconstruct the AE wavefunction. More specifically, this technique manages to transform the rapid oscillations near the ion core (see figure 2.5) into computational-friendly smooth wavefunctions.

2.6 Conclusion

In this chapter, we have laid the foundations for understanding DFT and as a consequence modern computational materials science. First, we have seen that solving the Schrödinger equation enables to completely determine a quantum mechanical system. Next, we used the Born-Oppenheimer approximation to decouple the dynamics of electrons and nuclei. Then, we have reviewed two theories to simplify the all-electron Schrödinger equation: the Hartree-Fock theory and the Density Functional Theory. Hartree established the basis of the HF theory by replacing the electron-electron interactions by an averaged potential, which enabled to express the N_e-electron wavefunctions as a product of N_e 1-electron wavefunctions. Fock completed the theory by introducing a Slater determinant to take into account Pauli's exclusion principle. Next, we have seen that the The Density Functional Theory uses another approach to simplify Schrödinger's equation. Indeed, the Hohenberg-Kohn theorems enabled to re-express the Schrödinger equation as the minimization of an energy functional, depending on a density functional. The Kohn-Sham equations then established a framework to compute this density functional by defining an equivalent fictitious system. We finished the description of DFT by introducing GGA and LDA and by describing how dispersion corrections can be included. At last, we have seen how DFT can be practically implemented. Whereas the Brillouin zone sampling drastically reduces the amount of wavefunctions, the use of pseudopotentials restricts the number of electrons to treat.

Chapter 3

Electrocatalysis

In this chapter, we will review the basic notions of electrocatalysis. Electrocatalysis is catalysis taking place in electrochemical reactions. The catalyst tunes the reaction rate without being consumed during the reaction. The catalyst material is most often present at the electrode surface, or even fully composes the electrode material [64]. Hence, electrocatalysis is the science exploring the rates of electrochemical reactions as a function of the electrode surface properties [35].

3.1 Electron transfer process

The electron transfer processes of electrochemical reactions are commonly called redox (oxidation-reduction) reactions. These reactions involve a change of oxidation state of the species composing the reaction constituents. The oxidation reaction is defined as the reaction in which a species loses electrons and increases its oxidation state. On the other hand, the reduction reaction is defined as the reaction in which a species gains electrons and reduces its oxidation state [1].
An electrochemical cell is composed of two electrodes dipped into an electrolyte. If the electrolytes of each electrode are different, the two compartments can be joined by a so-called salt bridge or separated by a diaphragm. The electrodes where the oxidation and reduction reactions occur are called the anode and cathode respectively. The electrolyte is an ion conductor but does not allow electrons to pass through. Electron transfers take place at the electrode/electrolyte interface. The currents associated to the oxidation and reduction reactions are called the partial anodic current and partial cathodic current respectively. Two types of electrochemical cells can be distinguished: galvanic cells and electrolytic cells. Both type of cells are depicted in figure 3.1. In galvanic cells electrochemical reactions occur spontaneously at the electrodes when they are connected externally by a conductor. In electrolytic cells an energy barrier refrains the

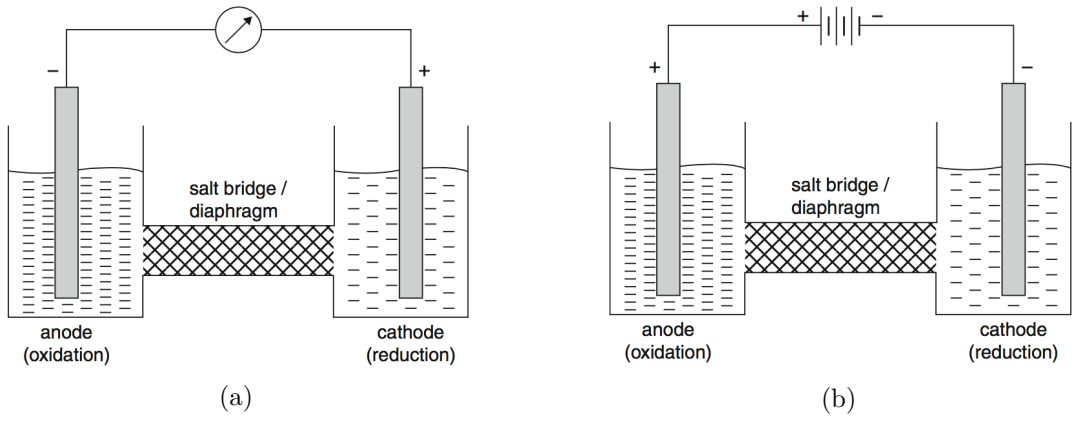

Figure 3.1: Schematic representation of (a) a galvanic cell and (b) an electrolytic cell [35].

redox reaction from happening spontaneously. This energy barrier can be reduced by applying a potential between both electrodes. When the equilibrium potential E_{eq} is applied between the two electrodes, partial anodic and cathodic currents are equal so that the total current is zero [35]. The cell potential is defined as the potential of the cathode minus the potential of the anode: $E = \phi_{cathode} - \phi_{anode}$.

3.2 Overpotential

In reality, a higher or lower potential than the equilibrium potential needs to be applied to drive a redox reaction to account for kinetic barriers at the cathode and anode, as well as resistance losses within the device [7]. The overpotential is the extent to which the reaction is driven beyond the equilibrium potential and is defined as:

$$\eta = E - E_{eq} \tag{3.1}$$

where E is the actual applied potential required to drive the reaction and E_{eq} is the theoretical required equilibrium potential. The expression for the applied potential E is given by the Nernst equation:

$$E = E^0 + \frac{RT}{n\mathcal{F}} \ln \frac{C_O}{C_R} \tag{3.2}$$

In this equation, E^0 is the cell potential at standard conditions, T is the temperature, R is the universal gas constant, $\mathcal{F}$ is the Faraday constant, n is the number of electrons transferred and C_O and C_R are the concentrations of the oxidized and reduced reactants respectively [57]. Be aware that this relation is only valid at equilibrium conditions.
The Butler-Volmer equation expresses the fundamental relationship between current and potential in an electrochemical cell, assuming both oxidation and reduction take place on the same electrode [35]:

$$j = j_0 \left\{ \exp\left(\frac{(1-\alpha)n\mathcal{F}\eta}{RT}\right) - \exp\left(\frac{-\alpha n\mathcal{F}\eta}{RT}\right) \right\} \tag{3.3}$$

In this equation, the first exponential term accounts for partial anodic current, whereas the second exponential term accounts for partial cathodic current. Also, j_0 is the exchange current density, α is the symmetry factor, and η is the overpotential defined above.
It is important to note here that the overpotential varies with current density. Therefore, the overpotential is often referenced to a corresponding exchange current density $j_0 = 10\ \mathrm{mA \cdot cm^{-2}}$ [57].

3.3 Tafel slope

In the limiting case where high overpotential is applied, the Tafel equation can be derived [35]:

$$\eta = a \pm b \log j \tag{3.4}$$

At high anodic overpotential, the partial cathodic current can be neglected, suppressing the second exponential term in equation 3.3 and leading to a plus–sign in equation 3.4. On the other hand, at high cathodic overpotential, the partial anodic current can be neglected, suppressing the first exponential term in equation 3.3 and leading to a minus–sign in equation 3.4. A typical Tafel plot is depicted in figure 3.2.
The Tafel slope is of significant interest in electrocatalysis. Indeed, the slope is an indicator of the number of electrons exchanged during catalysis and can thus provide valuable information regarding the reaction mechanism, but also the rate-determining step [35].

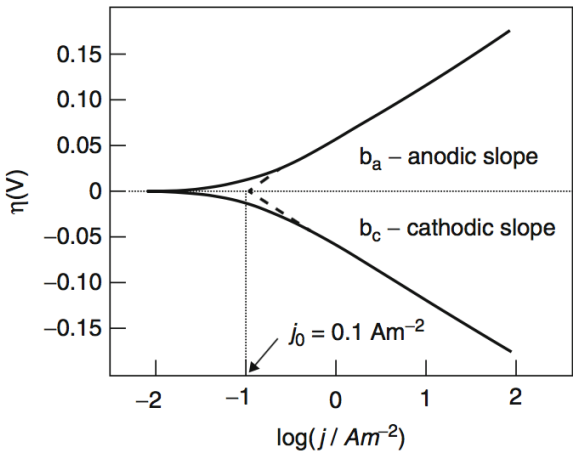

Figure 3.2: Tafel plot [35].

3.4 Volcano plots

A volcano plot is a very interesting tool to study an electrocatalyst's activity. It shows the reaction rate plotted as a function of a descriptor of the adsorption, which is often represented as bond strength of one or more species for different materials. The Sabbatier principle states that the interaction between catalyst and adsorbed species should neither be too strong nor too weak. Indeed, if the interaction is too weak, the species will not adsorb, but if the interaction is too strong, the species will not be able to desorb. Yet a good catalyst must be able to both adsorb and desorb the reactive species. Based on this principle, Volcano plots show a maximum corresponding to optimal activity [35]. The illustration of a conceptual volcano plot is given in figure 3.3.

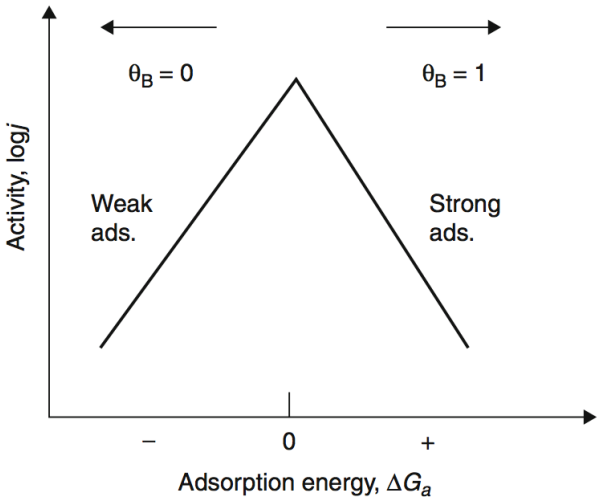

Figure 3.3: Conceptual schematic of a volcano plot. B is the rate determining step, θ_B is the coverage associated to the species involved in B and ΔG_a is the descriptor [35].

3.5 Conclusion

In this chapter, we have briefly reviewed fundamental concepts and tools in electrocatalysis. First, we discussed redox reactions. The oxidation and reduction reactions were defined as well as the major components of an electrochemical cell. Next, we introduced the concept of overpotential

(η), which was defined as the difference between the actual potential required to drive the reaction (E) and the theoretical required potential (E_{eq}). In this context, the Nernst equation and the Butler-Volmer equation enabled to relate current and potential in an electrochemical cell. At last, two convenient tools were presented: Tafel slopes to visualize the current-potential relationship and volcano plots to represent the activity of a catalyst.

Chapter 4

Oxygen Evolution Reaction

The Oxygen Evolution Reaction (OER) is probably one of the most studied electrocatalytic reactions today. Indeed, its understanding and mastering is of capital importance for diverse novel technologies such as fuel cells, hydrogen production, metal-air batteries... The main reason that puts this reaction under considerable research interest is because reducing its overpotential may largely enhance the associated technologies.

In this chapter, we will first analyze the global reaction and reaction mechanisms before reviewing the major catalyst materials reported in literature.

4.1 Reaction & reaction mechanisms

The overall reaction can be written as:

$$2H_2O_{(l)} \rightarrow 2H_{2(g)} + O_{2(g)} \tag{4.1}$$

This reaction can be split into two half reactions.

In **acidic** conditions, we have [57]:
Cathode:

$$4H^+ + 4e^- \rightarrow 2H_{2(g)} \qquad E^\circ = 0\,V \tag{4.2}$$

Anode:

$$2H_2O_{(l)} \rightarrow O_{2(g)} + 4H^+ + 4e^- \qquad E^\circ = +1.23\,V \tag{4.3}$$

The first and second reactions are commonly called the Hydrogen Evolution Reaction (HER) and Oxygen Evolution Reaction (OER) respectively. As can be seen in equations 4.2 and 4.3, the HER requires a 2-electron transfer (per mole of hydrogen created), whereas the OER requires a 4-electron transfer [57]. It has been reported that it is unlikely to have more than one electron transferred simultaneously [14]. Therefore, many-electron transfer processes require additional intermediate reaction steps and are thus more likely to be associated to higher overpotentials. Hence in the following we will only concentrate on the OER, which often happens more sluggishly than the HER.

It is important to note here that potentials are given according to the Standard Hydrogen Electrode (SHE). In this convention, the HER is referenced to occur at zero potential in acidic solution, at all temperatures and at 1 bar [67]. The drawback of this reference is that the potential is dependent on pH, which is not convenient for experimental benchmarking. The Reversible Hydrogen Electrode (RHE) tackles this shortcoming. This reference is very similar to the SHE, except here the acidic concentration corresponds to the electrolyte concentration,

making the potential stable at variable pH [35].

A reaction mechanism was proposed by Rossmeisl *et al.* and is now commonly accepted [18,54,55]:

$$\begin{aligned} 2H_2O_{(l)} &\rightarrow OH^* + H_2O + H^+ + e^- && \Delta G_1 \\ &\rightarrow O^* + H_2O_{(l)} + 2H^+ + 2e^- && \Delta G_2 \\ &\rightarrow OOH^* + 3H^+ + 3e^- && \Delta G_3 \\ &\rightarrow O_{2(g)} + 4H^+ + 4e^- && \Delta G_4 \end{aligned} \tag{4.4}$$

Notice that an asterisk (*) indicates an active site, or an adsorbed species when written next to a compound. The reaction mechanism is schematically depicted in figure 4.1.

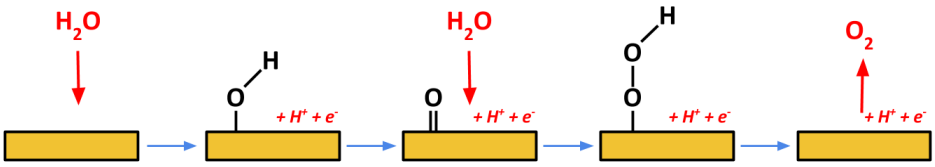

Figure 4.1: Schematic of the reaction mechanism of the OER. Black components are adsorbates, whereas red components are reactants or products in solution.

In **alkaline** conditions, the reaction can be rewritten as [57]:
Cathode:

$$2H_2O_{(l)} + 2e^- \rightarrow 2OH^- + H_{2(g)} \qquad E^\circ = -0.83\,V \tag{4.5}$$

Anode:

$$4OH^- \rightarrow 2H_{2(g)} + 2H_2O_{(l)} + 4e^- \qquad E^\circ = -0.40\,V \tag{4.6}$$

The associated reaction mechanism proposed by Rossmeisl *et al.* is given by [18, 54, 55]:

$$\begin{aligned} 4OH^- &\rightarrow OH^* + 3OH^- + e- && \Delta G_1 \\ &\rightarrow O^* + H_2O_{(l)} + 2OH^- + 2e^- && \Delta G_2 \\ &\rightarrow OOH^* + H_2O_{(l)} + OH^- + 3e^- && \Delta G_3 \\ &\rightarrow O_{2(g)} + 2H_2O_{(l)} + 4e^- && \Delta G_4 \end{aligned} \tag{4.7}$$

The same intermediates are present in both acidic and alkaline environment. Moreover, both descriptions are equivalent because they are both referenced to water ($H_2O \rightleftharpoons OH^- + H^+$). In the following, we will always focus on the acidic environment.

Free energy diagrams

A free energy differential is associated to each of the four steps in reaction 4.4: ΔG°_{1-4}. For an ideal catalyst, each of these reaction steps would have $\Delta G^\circ = 1.23\,eV$. However, for real catalysts this is not the case. Therefore, a potential determining step G^{OER} is determined as follows:

$$G^{OER} = \max[\Delta G^\circ_1, \Delta G^\circ_2, \Delta G^\circ_3, \Delta G^\circ_4] \tag{4.8}$$

This is the energy required for all steps to become downhill in energy. The overpotential is then given by:

$$\eta^{OER} = (G^{OER}/e) - 1.23V \tag{4.9}$$

Theoretically, at this overpotential the reaction given in equation 4.4 should be possible [40]. The effect of a finite potential U on all states involving n electrons in the electrode is included by shifting the energy of this state by $-neU$ [44]. A free energy diagram of an ideal and a real catalyst is given in figure 4.2.

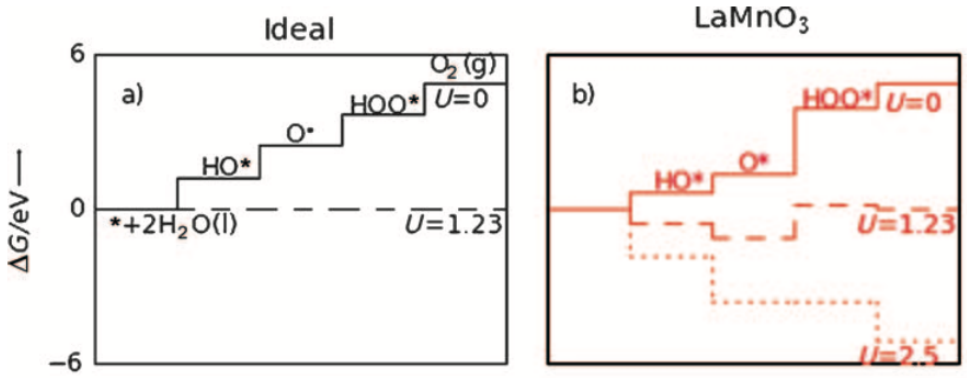

Figure 4.2: Free energy diagrams for the OER at pH=0 and T=298K. On the left: ideal catalyst. On the right: $LaMnO_3$ catalyst [40].

Notice that each successive step requires an additional proton-electron pair transfer. Therefore, when a potential is applied, the first step is shifted by $-eU$, the second step by $-2eU$ etc. For the ideal catalyst, all reactions have the same free energy and the reaction becomes possible at $U = 1.23\,V$. However, for a real catalyst, some steps have higher free energy. Therefore, higher potential is needed to make all steps downhill in energy. The potential determining step is defined as the step requiring the largest positive energy input to overcome the energy barrier between two successive steps at $U = 0\,V$. For instance, in figure 4.2 for the $LaMnO_3$ catalyst, step 3 (formation of OOH^*) is potential determining.

Free energy diagrams are a simple and powerful tool to study electrocatalytic reactions. Yet, this framework clearly has certain limits. Indeed, as will be seen later, energies are computed in vacuum. However, in reality the solvent (water) affects the energy of adsorbates. Moreover, the discussion is limited to a single, chosen reaction mechanisms, whereas experimentally other reaction mechanisms might be taking place in parallel. The effects of electric fields and surface charges are also not included. At last, proton transfer barriers are not taken into account [55]. Indeed, our framework only studies the energy of successive intermediates. However, in reality, an activation energy barrier is associated to the transition from one intermediate to the other. This activation barrier can be qualitatively assessed by the Evans-Polanyi principle, which states that there exists a linear relationship between the activation energy and the difference in energy between two successive intermediates [63].
All these effects discussed above may affect the experimentally required potential to drive a reaction.

4.2 Catalysts

In the last few decades, extensive research has been performed on OER catalysts. At first, metal catalysts were studied [54]. Then, it was discovered that metal oxides were interesting candidates from a thermodynamic point of view [55]. We will focus here on pioneering experimental work led by Rossmeisl *et al.*, before briefly reviewing novel catalyst materials and experimental research.

4.2.1 Metals

Rossmeisl *et al.* constructed a free energy diagram for OER on a Pt(111) surface with DFT, depicted in figure 4.3.
The first step in the reaction mechanism is the adsorption of a water molecule, forming an OH^* adsorbate and a proton. Next, the OH^* adsorbate loses a proton and another water molecule adsorbs, forming OOH^*. Finally, another proton is lost and an oxygen molecule desorbs, restoring

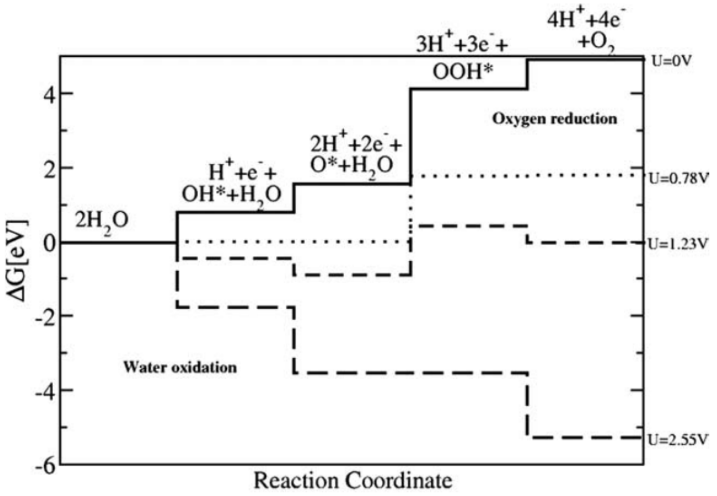

Figure 4.3: Free energy diagram for OER at different potentials on Pt(111) [54].

the original surface. This mechanism was also shown schematically in figure 4.1. Looking at figure 4.3, it can be seen that the potential limiting step for OER on Pt(111) is the formation of the OOH^* intermediate. At an applied potential $U = 2.55\,V$ this step, and as a consequence all the other steps, become downhill in energy. However, for potentials above $0.78\,V$, water splitting occurs (formation of OH^* and O^*), whereas adsorption of OOH^* requires a much higher potential. This means that the oxygen coverage will build up on the surface until it becomes more favorable for a water molecule to adsorb dissociatively on an adsorbed oxygen atom rather than on a free surface atom. With this observation it became clear that oxides could be better catalysts for OER because no supplementary potential is needed to first oxidize the surface. Rossmeisl *et al.* calculated that when the potential is increased gradually, the critical oxygen coverage required in order to make the formation of OOH^* possible is 2/3 on a Pt(111) surface and 1/3 on a Au(111) surface [54]. The corresponding potentials for OER at these oxygen coverages are $1.90\,V$ and $1.84\,V$ on a Pt(111) and a Au(111) surface respectively. The potential for the gold surface is slightly better because the required oxygen coverage is lower. Therefore more room is available for water to stabilize OOH^* and OH^* adsorbates.

4.2.2 Oxides

Following the investigation on metals, Rossmeisl *et al.* studied oxide catalysts for the OER. More specifically, RuO_2, IrO_2 and TiO_2 were studied [55]. The resulting free energy diagram for RuO_2 computed with DFT is depicted in figure 4.4.
The studied surface for this energy diagram is an O^*-covered RuO_2 surface. Adsorption occurs on an oxygen vacancy. The reaction mechanism on this surface is identical to what has been described in the previous section and is depicted in figure 4.1.
As can be seen in figure 4.4, the third step is the potential determining step, requiring $1.60\,V$. This potential is substantially lower compared to the $1.90\,V$ and $1.84\,V$ required for the OER on the Pt and Au surfaces respectively.
On IrO_2 a similar mechanism occurs, but the required potential ($1.79\,V$) is slightly higher than on RuO_2.

4.2.3 Scaling relations and activity volcano

Rossmeisl *et al.* demonstrated that there is a linear relationship between the adsorption energies of OH^* and O^*, and OOH^* and O^*, on different catalyst surfaces [40, 53–55]. More specifically, intermediates that bind to the surface through a same type of atom tend to scale linearly. The

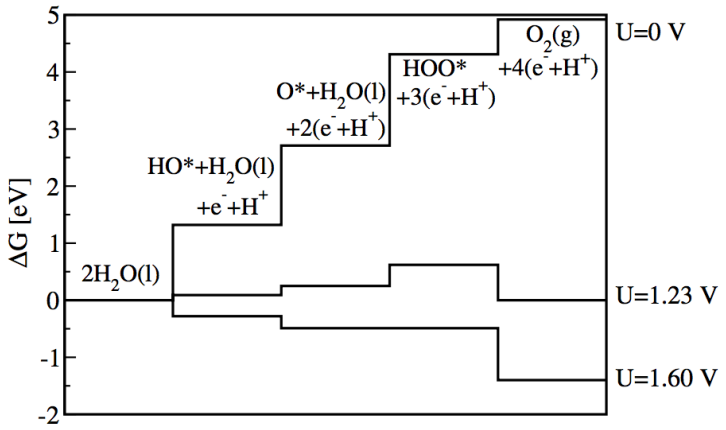

Figure 4.4: Free energy diagram for OER at different potentials on an O^*-covered RuO_2 surface [55].

slope attributed to an intermediate is an indicator for the number of bonds to the surface. OH^* and OOH^* bind to the surface through one bond, whereas O^* binds to the surface through a double bond. Therefore, plotting the OH^* and OOH^* bonding energies ΔE_{OH^*} and ΔE_{OOH^*} versus the O^* bonding energies ΔE_{O^*} gives approximately the same slope. This is represented conceptually in figure 4.5. The slope has a value of approximately 0.5 on metal surfaces and about 0.6 on oxide surfaces. This means that the difference between ΔE_{OH^*} and ΔE_{OOH^*} is constant. This difference was calculated to be about $3.2\,eV$ on metals and about $2.9\,eV$ on oxide catalysts [55].

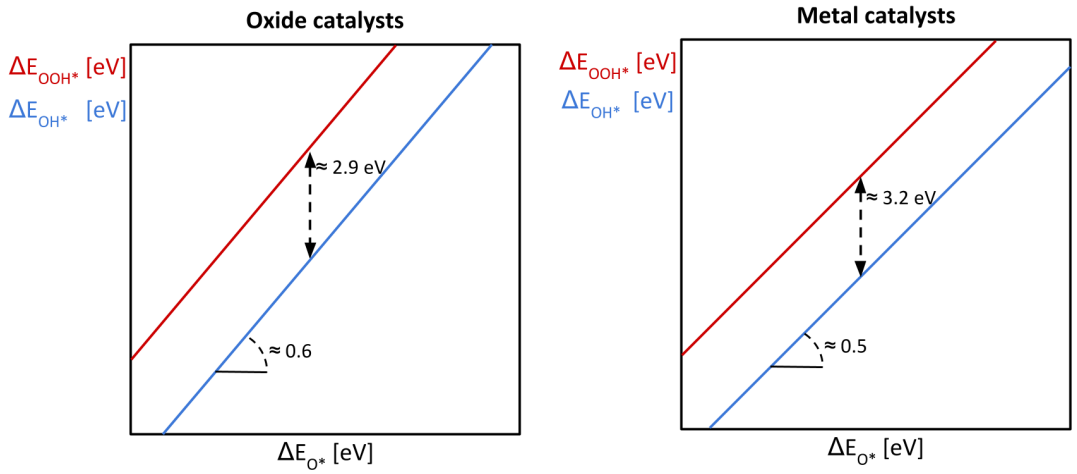

Figure 4.5: Conceptual representation of the scaling relations on metal and oxide catalysts.

This constant difference defines a lower limit for the overpotential of the OER. Indeed, we know that for an ideal catalyst the difference between two successive steps is $1.23\,eV$. Because there is a double proton-electron transfer between these two intermediates, the overpotential between the OH^* and OOH^* intermediates should optimally be $2 \times 1.23\,eV = 2.46\,eV$. However, due to the constant difference between the OH^* and OOH^* intermediates binding energies, there exists a minimal overpotential of $(3.2\,eV - 2.46\ eV)/2e = 0.37\,V$ on metals and $(2.9\,eV - 2.46\,eV)/2e = 0.22\,V$ on oxides, even if we could develop an optimal catalyst with ΔE_{O^*} just between ΔE_{OH^*} and ΔE_{OOH^*}. An additional challenge towards finding the optimal catalyst for OER thus consists in breaking the scaling between OH^* and OOH^* intermediates.

Given the constant difference between ΔE_{OH^*} and ΔE_{OOH^*}, the variation in overpotential from

one intermediate to the other is determined by ΔE_{O^*}. As such, either step 2 (ΔG_2) or step 3 (ΔG_3) is the potential determining step. We can show ΔG_2 can be used as a universal descriptor for the OER activity [53]:

$$\Delta G^{OER} = \max[\Delta G_2, \Delta G_3] = \max[(\Delta G_{OH^*} - \Delta G_{O^*}), (\Delta G_{OOH^*} - \Delta G_{O^*})] \tag{4.10}$$

$$= \max[(\Delta G_{OH^*} - \Delta G_{O^*}), \delta - (\Delta G_{OH^*} - \Delta G_{O^*})] \tag{4.11}$$

The associated overpotential is then given by:

$$\eta^{OER} = \max[(\Delta G_{OH^*} - \Delta G_{O^*}), \delta - (\Delta G_{OH^*} - \Delta G_{O^*})]/e - 1.23\,V \tag{4.12}$$

with $\delta \approx 3.2\,eV$ for metals and $\delta \approx 2.9\,eV$ for oxides.
Rossmeisl *et al.* plotted the catalyst activity as a function of oxygen binding energy for both metal and oxide catalysts (see figure 4.6) [55].

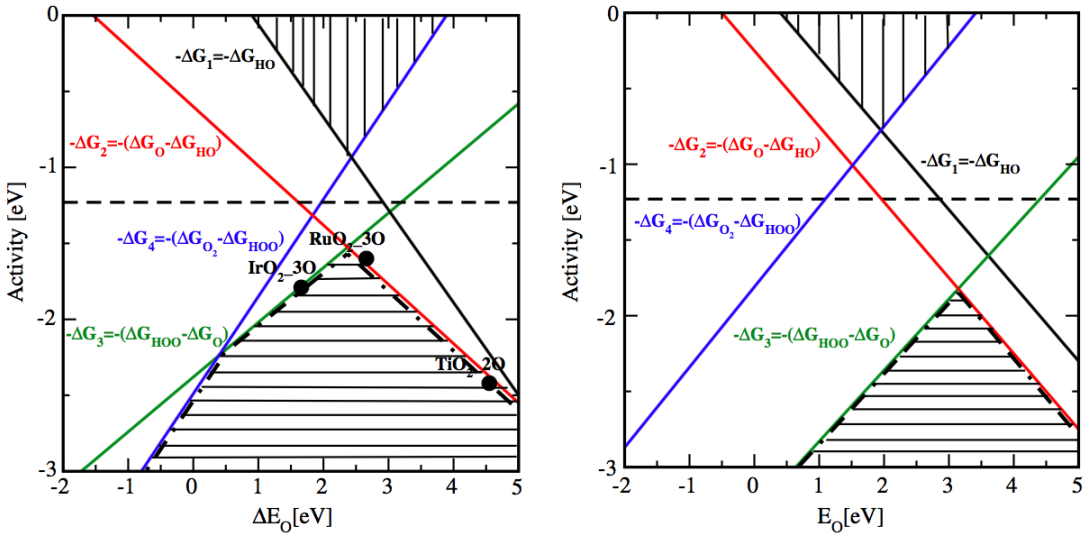

Figure 4.6: Activity as a function of oxygen binding energies for oxide catalysts (on the left) and metal catalysts (on the right). The resulting volcano is indicated by the hatched area. The horizontal dashed lines indicate the theoretical optimal overpotential of $1.23\,V$ [55].

The negative of the free energy $-\Delta G$ is used as a measure of the reaction rate and is called activity. The lowest rate is the upper bound for the total rate. Therefore, as can be seen in figure 4.6, the formation energies of the O^* and OOH^* intermediates monitor the overall reaction rate. This confirms what has been described above. Still, we are looking for the optimal reaction rate, thus the top of the volcano corresponds to the optimal catalysts. On the left of the volcano maximum, the formation of OOH^* (3^{rd} step) is the rate determining step, whereas on the right, the formation of O^* (2^{nd} step) is rate-determining [55]. The volcano-shape translates the Sabbatier principle (see section 3.4): on the left side of the volcano maximum, adsorption is too strong, whereas on the right side adsorption is too weak [35]. As can be seen in figure 4.6, in this analysis RuO_2 is the best oxide catalyst, binding oxygen a little too weakly. IrO_2 requires a slightly higher overpotential and binds oxygen too strongly.

4.2.4 Other catalyst materials & future perspectives

The universal trends described in the previous section were confirmed by later studies led by Rossmeisl *et al.* [40]. A multitude of other oxide catalysts were studied such as perovskite, spinel, rock salt and bixbyite and also exhibited the universal scaling relationship between the binding energy of HOO^* and HO^*. These oxide materials can be composed of diverse combinations

of transition metals, which results in tunable OER properties. Other promising candidates for OER catalysis include layer structure type materials. These are typically composed of transition metals surrounded by octahedron oxygen structures in a layered structure separated by protons. Recent developments in oxide catalyst investigations reported promising behaviour by doping oxide systems (typically spinel and layered structures) with Fe, Co or Ni [8, 57].
On the other hand, metal catalysts have lately exhibited interesting properties. More specifically, metal chalcogenides, metal pnictides and organometallics have shown excellent OER catalytic activities [57].
Finally, even non-metal structures have lately shown promising behaviours, like carbon nanotubes and other nanostructures [57].
Despite the large range of materials that has so far been studied, the perfect catalyst for OER was certainly not discovered yet. However, towards this goal, the thorough understanding of reaction mechanisms remains of paramount importance. In this scope, DFT computations become a very interesting tool.

4.3 Conclusion

In this chapter, we started by studying the reaction and reaction mechanisms of OER, before reviewing major catalyst materials reported in literature. We have studied the work of Rossmeisl *et al.* on both metal and oxide catalysts. It was demonstrated theoretically that oxides were better candidates for OER than metals. Moreover, it was shown that adsorbates that bind to the surface through the same type of atom tend to scale linearly. Therefore, it was shown that there exists a constant difference between ΔE_{OH^*} and ΔE_{OOH^*}. As a consequence, we have concluded that ΔE_{O^*} can be used as a descriptor of the OER activity and that either the adsorption of OH^* or OOH^* will be the potential determining step. At last, a brief review of other catalyst materials was given.

Chapter 5

CO_2 Reduction Reaction

At a time where society is facing climate change and the shrinking of fossil fuel reserves, the reduction of carbon dioxide represents a huge stake. However, CO_2 electro-reduction faces several scientific challenges. Indeed, the conversion to e.g. methane is an 8-electron transfer process, which is likely to be a kinetically complex mechanism, requiring transition through unfavorable intermediates [35]. Moreover, hydrogen evolution becomes favorable at $0\,V$ vs RHE. Therefore, water reduction to hydrogen is in strong competition with CO_2 reduction [39], which happens at negative potentials. Finally, CO_2 reduction currently generates a wide range of products such as formic acid, carbon monoxide, ethylene and hydrogen. The separation of these products is costly and impractical. Therefore, the selectivity towards the generation of specific products remains an important issue.

In this chapter, reaction mechanisms and catalysts for CO_2 reduction will be discussed in parallel. First, the experimental and computational research on metals will be reviewed. Next, we will briefly discuss CO_2 reduction on oxides, which is a novel domain.

5.1 Experimental research

Hori *et al.* performed pioneering experimental research on CO_2 reduction [23,24]. They concluded that of all pure metal catalysts, copper was the most selective, able to produce hydrocarbons with highest energy density at highest Faradaic efficiency. The Faradaic efficiency is defined as the the efficiency at which electrons are transferred to promote an electrochemical reaction [39]. In this context, the Faradaic yield can be seen as the generated fraction of a specific product on the overall generated products. An overview of the main products and their respective Faradaic yields of CO_2 reduction on a copper catalyst is given in figure 5.1.

As can be seen in figure 5.1, different products are generated, including methane, ethylene, formic acid, carbon monoxide, hydrogen, and others. Let us focus on the production of methane. In order to get a significant Faradaic yield, an overpotential of $\sim 1\,V$ is required. This is very large compared to the overpotential required for the oxygen evolution reaction, which is usually the reaction occurring at the counter-electrode for CO_2 reduction. This $\sim 1\,V$ overpotential is also highly ineffective compared to the theoretical thermodynamic required potential:

$$CO_{2(g)} + 8H^+ + 8e^- \rightarrow CH_{4(g)} + 2H_2O_{(l)} \qquad E_0 = 0.169\ V \text{ vs RHE} \tag{5.1}$$

However, the Faradaic yield for hydrocarbons on copper is reported to be $72.3\,\%$ while the yield for H_2 is $20.5\ \%$ [23, 24].

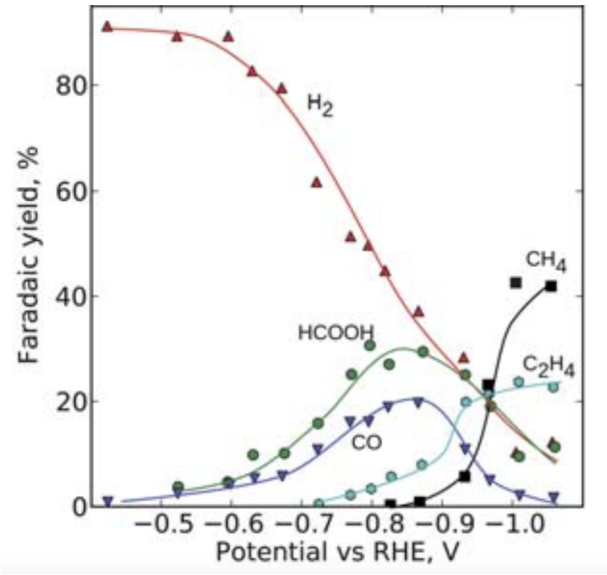

Figure 5.1: Faradaic yield plots as a function of applied potential in the electrochemical reduction of CO_2 at a copper electrode in 0.1 M $KHCO_3$ (pH 6.8) at 18.5 °C, as measured by Hori *et al.* [24].

5.2 Computational research

Following the study of Hori *et al.*, Peterson *et al.* performed computational studies using DFT to gain insight into the reaction mechanism [48, 49]. The proposed mechanism for methane production is given as:

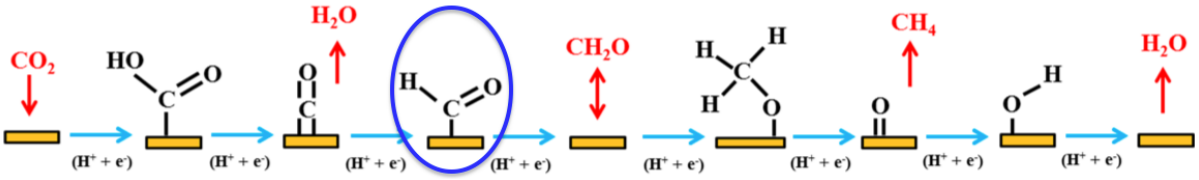

Figure 5.2: Reaction pathway for the reduction of CO_2 to CH_4 on copper as proposed by Peterson *et al.* through a CHO^* intermediate. Black components are adsorbates, whereas red components are reactants or products in solution. Figure reproduced from reference [29].

The reaction intermediates along with free energy diagrams for the production of hydrogen, formic acid, carbon monoxide and methane on copper are given in figure 5.3.
This reaction pathway for the production of methane on a copper catalyst is commonly accepted in literature [49]. As can be seen in figure 5.3, the formation of CHO^* represents the potential limiting step, requiring $-0.74\,V$ [49]. In a later publication, Peterson *et al.* performed a more thorough research on the CO_2 reduction reaction, where the stability of all adsorbates is referenced to the CO^* bonding energy [48]. From this study, it became clear that the formation of CHO^* remains potential expensive for all transition metal oxides. Therefore, Peterson proposed another reaction pathway given in figure 5.4, which is believed to be kinetically more accessible [43, 50, 62]. In this case, the potential limiting step is the protonation of CH^* to CH_2^* [48]. This alternative route for CO_2 reduction was shown to be more likely on catalysts with low CO^* bonding energy. However, at low CO^* bonding energy, the production of gaseous CO is likely to predominate, before other crucial intermediates for the formation of hydrocarbons can be formed. On the other hand, at high CO^* bonding energy, the catalyst is likely to be largely covered by CO^*, leading to a reduced affinity for the formation of downstream intermediates. In this case, the production

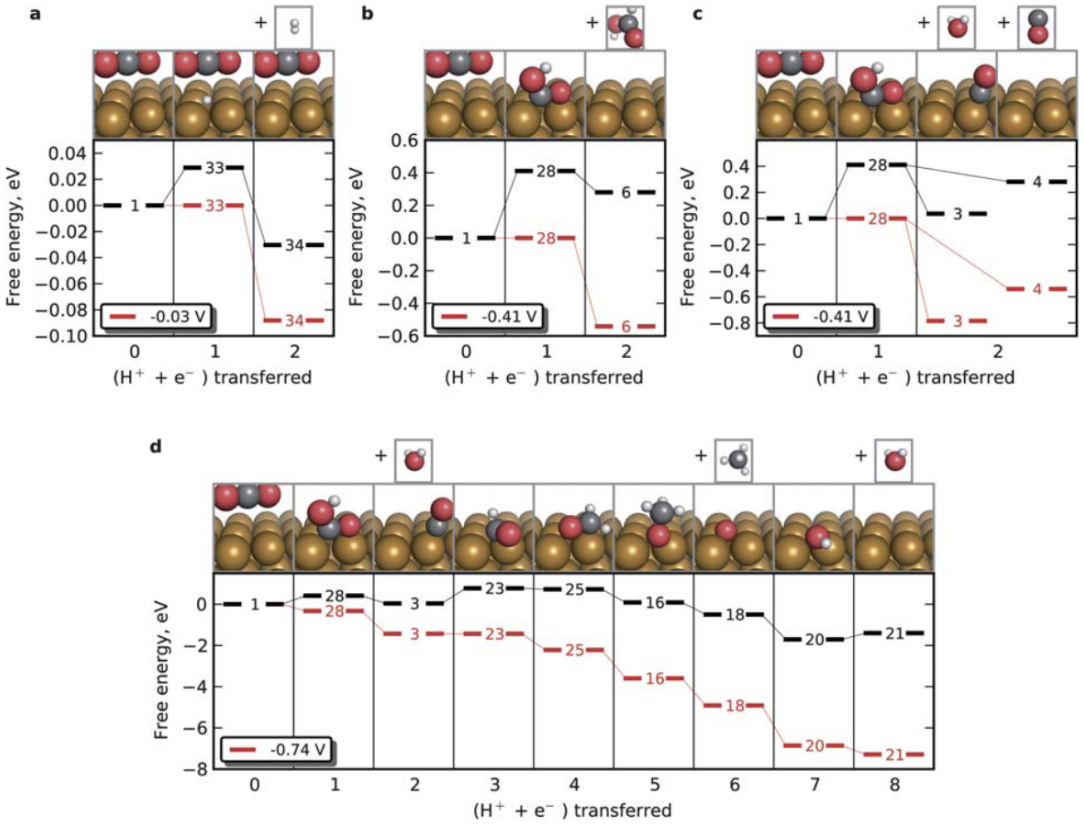

Figure 5.3: Reaction pathways and free energy diagrams for the reduction of CO_2 into (a) H_2, (b) $HCOOH$, (c) CO, (d) CH_4. On the insets, the color of the spheres indicate different atoms: red: O, grey: C, white: H, gold: Cu [49].

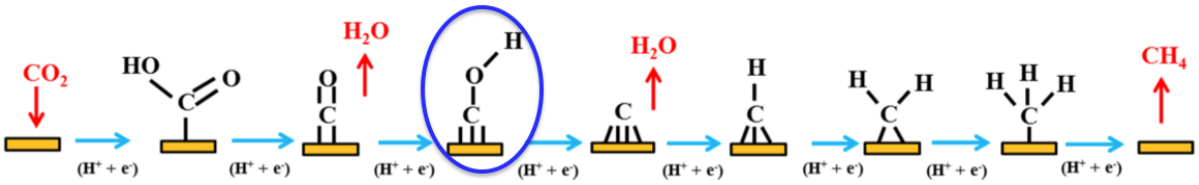

Figure 5.4: Alternative reaction pathway for the reduction of CO_2 to CH_4 on copper as proposed by Peterson *et al.* through a COH^* intermediate. Black components are adsorbates, whereas red components are reactants or products in solution. Figure reproduced from reference [29].

of hydrogen will be the prominent product. The reason why copper is such a good catalyst for CO_2 reduction is because it has an intermediate CO^* bonding strength. On the contrary, Au, Ag, and Zn bind CO^* too weakly, whereas Ni, Pt, and Fe bind CO^* too strongly [25, 36]. However, even at optimal CO^* bonding energy, the theoretical overpotential still adds up to $\pm 0.7\,V$. Further reducing this overpotential would require a surface capable of breaking the scaling relationship between the bonding energies of key intermediates, such as CO^* and CHO^* [25].

5.3 Oxide catalysts

As it becomes clear now, research is far from having found the ideal catalyst for CO_2 electroreduction into hydrocarbon fuels. Indeed, the required overpotentials are too large and selectivity towards specific products is very poor. Moreover, due to the competing hydrogen evolution reaction, efficiency towards hydrocarbons remains low. Since the work of Peterson *et al.*, considerable

effort has been made in order to develop better electrocatalysts. Lately, bifunctional alloys have been under considerable research [20, 25].
To the best of our knowledge however, only one paper has studied RuO_2 as a catalyst for CO_2 reduction, and no research has been done regarding IrO_2. It will be in the scope of this work to explore these catalysts in the framework of CO_2 electro-reduction.

Karamad *et al.* motivated their research towards RuO_2 catalysts based on the fact that CO_2 electro-reduction has been reported on RuO_2 at overpotentials less than $0.4V$ RHE [56]. RuO_2 was reported to remain stable at reducing potentials [2, 52]. Karamad *et al.* claim that the RuO_2 surface is partially reduced at negative potentials [27]. They also claim that CO^* covered surfaces exhibit high thermodynamic stability [27]. This hypothesis is supported by the high desorption energies and very low Faradaic efficiency experimentally observed for CO production on RuO_2 [56]. However, the question remains whether these structures are kinetically accessible. Indeed, the formation of a CO^* adsorbate from CO_2 adsorption is largely accepted to occur through the formation of a rather bulky $COOH^*$ intermediate:

$$^* + CO_2(g) + (H^+ + e^-) \rightarrow COOH^* \tag{5.2}$$

$$COOH^* + (H^+ + e^-) \rightarrow CO^* + H_2O \tag{5.3}$$

This mechanism was reported to take place on copper and gold [22, 49].
However, the most notable conclusion of the work of Karamad *et al.* is the formulation of a new reaction mechanism for the production of methane:

$$CO_2(g) \rightarrow OCHO^* \rightarrow HCOOH^* \rightarrow H_2COOH^* \rightarrow CH_3O^* + OH^*(cu) \rightarrow CH_4(g) + O^*(cu) + OH^*(br) \rightarrow +O^*(br) + H_2O \rightarrow +OH^*(br) \rightarrow H_2O \tag{5.4}$$

At this stage, note that "cu" and "br" denote two different active adsorption sites. These will be discussed in more detail in section 6.

5.4 Conclusion

In this chapter, we unraveled reaction pathways and catalyst materials for CO_2 reduction. It is noteworthy to realize CO_2 reduction into hydrocarbon fuels is often a complex process requiring many-electron processes. As a consequence, selectivity towards specific products is often low. On metals, CO_2 reduction to methane is a well documented reaction, both experimentally and computationally. Two reaction mechanisms are commonly accepted: through a CHO^* intermediate or through a COH^* intermediate. For the first reaction mechanism, the protonation of CO^* to CHO^* represents the potential limiting step, whereas for the second reaction pathway, the protonation of CH^* to CH_2^* is potential limiting. Karamad *et al.* have studied the reduction of CO_2 on RuO_2 and suggest another reaction pathway through an $OCHO^*$ intermediate. Moreover, Karamad *et al.* claim the RuO_2 surface is reduced and covered with CO^*.
In this work, we will verify the hypotheses of Karamad *et al.* Moreover, we will investigate the reaction pathway. Next to RuO_2, the same aspects will also be studied on IrO_2.

Part II

Ab Initio computations

Chapter 6

Materials & Methods

In the present work, two materials are studied: IrO_2 and RuO_2. These compounds have lately been under thorough investigation in the scope of OER and are now used as benchmark electrocatalysts owing to their high catalytic activities. However, the high cost and scarcity of these precious metal oxides currently refrains them from being used in large-scale industrial applications. As was depicted in figure 4.6, RuO_2 exhibits slightly better OER activity than IrO_2. However, RuO_2 was reported to dissolve faster than IrO_2 under anodic potentials (OER). Under cathodic potentials (HER, CO_2 reduction), both oxides were reported to remain stable [5]. The catalytic activities of IrO_2 and RuO_2 can widely vary as a function of their structure, composition or preparation process [8, 57]. Here, IrO_2 and RuO_2 slabs will be investigated.

In this chapter, the computational description of IrO_2 and RuO_2 is presented. Moreover, we introduce a framework to describe the stability of intermediates as a function of applied potential.

6.1 Materials

Both IrO_2 and RuO_2 adopt a rutile structure. In this structure, each Ir/Ru atom has a coordination of 6, meaning it is surrounded by an octahedron of 6 oxygen atoms. On the other hand, each oxygen atom is bound to 3 Ir/Ru atoms. Along this work, we will study 4-layer (2×1) periodic slabs. Figure 6.1 depicts a typical supercell used for the simulation of IrO_2. $RuO2$ slabs have similar structure. For all computations, a minimum vacuum distance of 10 Å was ensured between slabs to avoid interaction. The adsorption of intermediates is only studied on the upper (110) facet. Bottom active sites are terminated with hydrogen atoms to refrain free electrons from perturbing relaxation.

The supercell dimensions are a = 6.50 Å, b = 6.38 Å and c = 25 Å for IrO_2 slabs and a = 6.43 Å, b = 6.27 Å and c = 25 Å for RuO_2 slabs. Dimensions in the **c**-direction are given as a minimum, because the relaxation of certain structures sometimes required a larger vacuum distance. The initial relaxed supercell structures as depicted in figure 6.1 were recovered from reference [37]. In these structures, the two bottom layers are fixed into bulk positions, whereas the two upper layers are allowed to relax.

The slab surface has coordinately unsaturated (CUS) sites and bridge-sites. Both type of sites are represented in figure 6.2.

Take note that each slab has two CUS-sites and two bridge-sites. Other apparent sites are repeated atoms due to the supercell structure. In the following, an active CUS-site will denote a position on top of the CUS Ir/Ru atom, whereas an active bridge-site will denote the position replacing the bridge oxygen atoms. Active sites are denoted with an asterisk (*). Species adsorbed on an active site are followed by an asterisk.

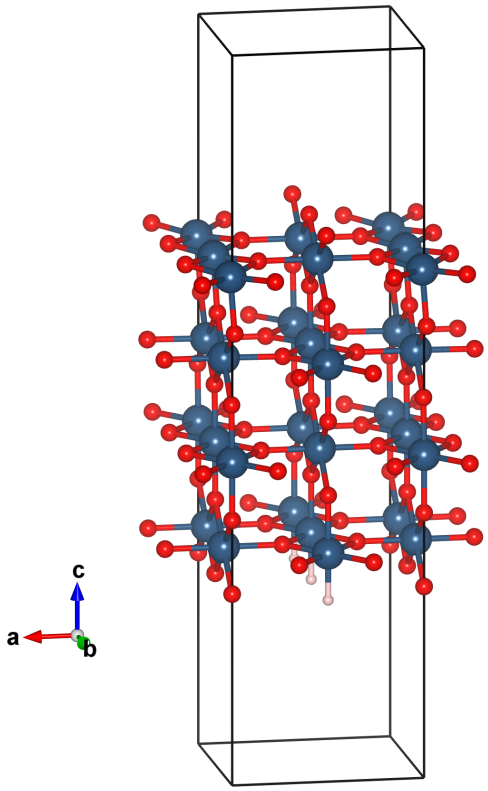

Figure 6.1: Supercell used for the simulation of IrO_2 slabs. The structure is similar for RuO_2 slabs. Colors denote oxygen (red), hydrogen (white) and iridium (blue) atoms.

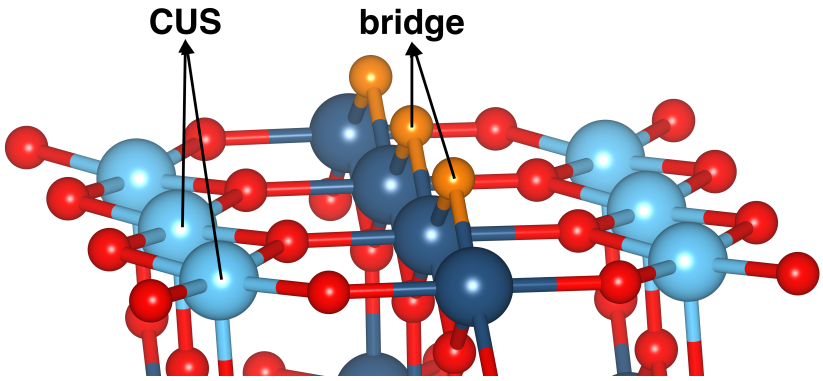

Figure 6.2: Representation of CUS- and bridge-sites. Light blue and orange atoms respectively represent Ir-CUS and O-bridge sites.

6.2 Computational details

All simulations were run using VASP (Vienna Ab initio Simulation Package) [31–33], implementing DFT with the PAW (Projector-Augmented Wave) method [30]. An RPBE (Revised Perdew-Burke-Erzenhof) exchange-correlation functional [17] was used for all simulations, in accordance with reference work simulating rutile oxides [27,37,55]. K-point sampling was done using a 8×4×1 Monkhorst-Pack [45] k-point grid. Because the unit cell is replicated twice in the **b**-direction, the k-point sampling can be halved in this direction. Moreover, the **c**-direction is much bigger than the **a**- and **b**-directions, therefore, only one k-point is sufficient. Van der Waals corrections were applied using the Tkatchenko-Scheffler method [58], in accordance with reference work [37]. The cutoff energy was set to $400\,eV$. For theoretical background about these parameters, the

reader is redirected to chapter 2. Dipole corrections were also applied. Finally, symmetry was turned off and all computations were spin polarized.

Smearing

Because IrO_2 and RuO_2 are metallic systems, they exhibit a sharp drop in occupation around the Fermi level. This triggers a discontinuity in the integration over the Brillouin zone, resulting in a significant increase in computational cost. To overcome this problem, the step function of occupancies is replaced by a smoother, "smeared" function. There exist different smearing schemes such as Gaussian smearing, Fermi smearing or Methfessel-Paxton smearing [41], which is used here. More specifically, a second order Methfessel-Paxton smearing is implemented, which uses a step function expanded into polynomials and Gaussian functions. Smearing is often characterized with a parameter, namely $\sigma = k_B T$. This parameter corresponds to a fictional temperature which tunes the broadening of the occupation function. In this case, $\sigma = 0.2\,eV$.

Relaxation scheme

Two types of relaxations can be distinguished. On the one hand, the electronic relaxation implements the SCF method (see figure 2.1 on page 7) to find the ground state energy at fixed atomic positions. On the other hand, the ionic relaxation aims to relax the ionic positions and/or unit cell shape/size. These two relaxation types are implemented in a double nested loop. In the inner loop, electronic relaxation is performed and the final energy and forces acting on each ion are computed. Next, the ionic positions are updated towards more favorable positions and the outer loop (ionic relaxation) progresses one step. Then, an electronic relaxation is performed again followed by an ionic relaxation step, etc., until the convergence criterion is met.
For both electronic and ionic relaxation, different schemes are implemented in VASP. The electronic relaxation requires diagonalization of the $\widehat{H}$ matrix. This can happen either by direct diagonalization or with iterative methods (conjugate gradient and Car-Parinello algorithms). In this work, iterative methods are used. A Davidson [6] scheme is used for the initial phase (here set to 5 electronic steps) and the RMM-DIIS [51, 68] method for the rest of the relaxation. The electronic convergence criterion is set to 1E-6 eV maximum. This means electronic convergence is reached once the difference between to electronic steps is smaller than 1E-6 eV. If this criterion is not met, VASP will break the self-consistent loop after 200 electronic steps.
The ionic relaxation can also happen according to different algorithms. However, first, the forces acting on the atoms are calculated with the Hellman-Feynman theorem [9, 21], which can easily account for forces from both atomic and electronic origin. The theorem states that if an exact Hamiltonian $\widehat{H}$ and the corresponding wavefunctions ϕ_i are calculated, the force on an atom is the expectation value of the partial derivative of $\widehat{H}$ with respect to atomic position $\mathbf{r}_I$.

$$\mathbf{F}_I = -\frac{dE}{d\mathbf{r}_I} = -\left\langle \phi_i \left| \frac{\partial \widehat{H}}{\partial \mathbf{r}_i} \right| \phi_i \right\rangle = -\frac{\partial V_{IJ}}{\partial \mathbf{r}_I} - \int \frac{\partial V_{ext}}{\partial \mathbf{r}_I} n(\mathbf{r}) d\mathbf{r} \tag{6.1}$$

Once the forces are calculated, the new atomic positions can be determined using different algorithms. In this case, the conjugate-gradient algorithm is implemented. In the first step, ions are moved in the direction of steepest descent (i.e. direction of calculated forces & stress tensor). A line minimization is then performed in several steps:

(i) a trial step into the search direction.

(ii) the approximate minimum of the total energy is calculated using quadratic or cubic interpolation and a corrector step towards the approximate minimal energy is performed.

(iii) energy and forces are recalculated and minimization is continued if stopping criterion is not reached.

Ions are allowed to fully relax, whereas cell shape and volume are kept fixed. The ionic relaxation criterion was set to 1E-2 $eV/$Å.

ZPE Computation

Zero Point Energy (ZPE) corrections have been applied in certain computations. These corrections were approximated by calculating the vibrational frequencies of the considered system, which are calculated from the Hessian matrix (matrix of the second derivatives of the energy with respect to the atomic positions). This matrix is determined using finite differences: each ion is displaced in each direction of space. The Hessian matrix can then be deducted from the computation of the forces at each step [34]. 4 steps were performed in each direction of space: $\pm\delta$ and $\pm 2\delta$, where δ sets the size of each step. In this case: $\delta = 0.015$ Å.

The choice of computational parameterization described in this section is consistent with the work of other groups on the same materials [27, 37].

6.3 Computational Hydrogen Electrode

The systems studied in this work are open systems, where a slab composed of IrO_2 or RuO_2 interacts with a water reservoir. The energy of the system can be defined by a grand canonical potential Φ:

$$\Phi = G^{DFT} - n_O\mu_O - n_H\mu_H \tag{6.2}$$

where n_O, n_H and μ_O, μ_H are respectively the amount of oxygen and hydrogen atoms and the chemical potentials of an oxygen and a hydrogen atom. Moreover, G^{DFT} is the Gibbs free energy computed in the DFT framework. Before we get to this concept, let us first define the classical definition of the Gibbs free energy:

$$G(T,p) = H(T,p) - TS(T,p) \tag{6.3}$$

However, in DFT, temperature is at $T = 0\,K$. To take into account the effect of temperature, Zero Point Energies (ZPE) and entropy corrections are applied. Hence, in the framework of DFT, the Gibbs free energy is expressed as:

$$G^{DFT} = E^{DFT} + ZPE - TS \tag{6.4}$$

where E^{DFT} is the total energy as obtained from DFT computations, ZPE is the Zero Point Energy and S is the entropy. In this work, the standard entropy was only taken into account for molecules and adsorbates and has been neglected for slabs.

Coming back to equation 6.2, μ_O and μ_H are defined in the framework of the Computational Hydrogen Electrode (CHE), developed by Nørskov *et al.* [44]. This model enables to take into account the effect of an applied potential on the system energy. The formulation is based on the Reversible Hydrogen Electrode (RHE), where the Hydrogen Evolution Reaction (HER) is defined to be in equilibrium at zero potential, at $pH = 0$, at $T = 298\,K$, and with H_2 at 1 atm:

$$H^+ + e^- \rightleftharpoons \frac{1}{2}H_2 \tag{6.5}$$

The CHE model relates the chemical potential of a proton-electron pair (which we will denote for simplicity as μ_H) to 1/2 of that of a hydrogen molecule, at $0\,V$. The effect of an applied potential is taken into account by the standard relation between chemical and electrical potential:

$\Delta G = -eU$, where e is the positive elementary charge of an electron and U is the applied potential. Altogether, this gives:

$$\mu_H = \frac{1}{2}G^{DFT}_{H_{2(g)}} - eU \tag{6.6}$$

The oxygen molecule is known to be badly modeled by DFT [55]. Therefore, to avoid known errors of DFT, the chemical potential of oxygen is computed as:

$$\mu_O = G^{DFT}_{H_2O_{(l)}} - 2\mu_H \tag{6.7}$$

Introducing equations 6.6 and 6.7 in equation 6.2 gives:

$$\Phi(U) = G^{DFT} - n_O\left[G^{DFT}_{H_2O_{(l)}} - 2\left(\frac{1}{2}G^{DFT}_{H_{2(g)}} - eU\right)\right] - n_H\left[\frac{1}{2}G^{DFT}_{H_{2(g)}} - eU\right] \tag{6.8}$$

$$= G^{DFT} - n_O G^{DFT}_{H_2O_{(l)}} + n_O G^{DFT}_{H_{2(g)}} - 2n_O eU - \frac{1}{2}n_H G^{DFT}_{H_{2(g)}} + n_H eU \tag{6.9}$$

As such, we have established an expression of the energy as a function of potential. Notice that the dependence on applied potential is linear and that the addition of hydrogen atoms tends to make the slope more positive, whereas the addition of oxygen atoms tends to make the slope more negative.
In a similar manner, we can extend this framework to include carbon atoms. The grand canonical potential then becomes:

$$\Phi = G^{DFT} - n_O\mu_O - n_H\mu_H - n_C\mu_C \tag{6.10}$$

where μ_C is referenced to $CO_{2(g)}$:

$$\mu_C = G^{DFT}_{CO_{2(g)}} - 2\mu_O \tag{6.11}$$

By introducing equations 6.6, 6.7 and 6.11 in equation 6.10, we can derive an expression for the energy depending on potential ($\Phi(U)$) similar to equation 6.9.
Finally, notice that these are not the only possibilities to define μ_O and μ_C. For instance, μ_C could have been defined with respect to $CH_{4(g)}$. This choice does indeed make a small difference, but the current definitions were established in accordance with reference work [27].

Relative stability diagrams

In order to be able to conveniently compare the stability of different structures at different applied potentials, the energy of structures can be plotted in a relative stability diagram [19]. In these diagrams, the energy of a system as defined by equation6.9 is plotted versus the applied potential U. More specifically, the energy of a reference structure is subtracted from the energy of each represented structure ($\Phi - \Phi_{ref}$). Because the amount of Ir/Ru atoms in our slabs is fixed, the subtraction cancels out the contribution of these atoms in the expression for the total energy. In figure 6.3, a conceptual relative stability diagram is represented.
In figure 6.3, 'R' denotes a reference structure, '$R-H$' denotes the reference structure with an adsorbed hydrogen atom and '$R-OH$' denotes the reference structure with an adsorbed OH group. The colored areas indicate the most stable structures – corresponding to lowest relative energy – in the whole potential range.
Towards negative potentials, the surface is reduced. In our case, this corresponds to adding hydrogen or removing oxygen atoms. On the other hand, towards positive potentials, the surface is oxidized. This corresponds to removing hydrogen or adding oxygen atoms.

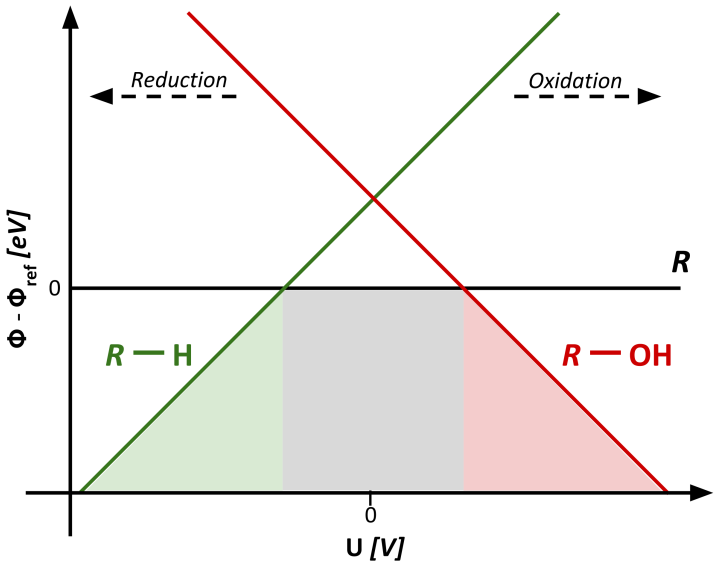

Figure 6.3: Conceptual representation of a relative stability diagram. 'R' denotes a reference structure, '$R-H$' denotes the reference structure with an adsorbed hydrogen atom and '$R-OH$' denotes the reference structure with an adsorbed OH group. The colored areas indicate the most stable structures (lowest relative energy) in the whole potential range.

6.4 Conclusion

In this chapter, we developed how IrO_2 and RuO_2 slabs can be described computationally using VASP. The basic slab structures were presented and the adsorption sites (CUS- and bridge-sites) were defined. Moreover, methods for describing ZPE and vdW corrections were discussed. After reviewing computational parameters, we introduced the Computational Hydrogen Electrode (CHE). In this framework, the chemical potential of a hydrogen atom is linked to free energy of a hydrogen molecule and the effect of an applied potential is taken into account. Finally, relative stability diagrams were presented as a tool to investigate structures at different applied potentials.

Chapter 7

Oxygen Evolution Reaction

In this chapter, the Oxygen Evolution Reaction on IrO_2 & RuO_2 is studied. This reaction is usually studied at high potential. However, in this case we will investigate low potentials as a preliminary study towards the CO_2 reduction reaction, which also takes place at low potential. First, we will study the classic reaction as it was reported in many previous studies. Second, we will explore other possible intermediates which may intervene in the OER at low potential.

7.1 Free energy diagrams

In this section, we will reproduce the work of Karamad *et al.* published in reference [55]. The four reaction steps are reminded here:

$$^* + H_2O_{(l)} \rightarrow OH^* + H^+ + e^- \qquad \Delta G_1 \tag{7.1}$$

$$OH^* \rightarrow O^* + H^+ + e^- \qquad \Delta G_2 \tag{7.2}$$

$$O^* + H_2O_{(l)} \rightarrow OOH^* + H^+ + e^- \qquad \Delta G_3 \tag{7.3}$$

$$OOH^* \rightarrow ^* + O_2 + H^+ + e^- \qquad \Delta G_4 \tag{7.4}$$

The asterisks (*) denote actives sites, the components followed by an asterisk being the adsorbed components. The corresponding reaction free energies are given below to illustrate the concept of CHE:

$$\Delta G_1 = G_{OH^*} + G_{(H^+ + e^-)} - G_* - G_{H_2O_{(l)}} \tag{7.5}$$

$$= G_{OH^*} + \frac{1}{2}G_{H_2} - G_* - G_{H_2O_{(l)}} - eU \tag{7.6}$$

$$\Delta G_2 = G_{O^*} + G_{(H^+ + e^-)} - G_{OH^*} \tag{7.7}$$

$$= G_{O^*} + \frac{1}{2}G_{H_{2(g)}} - G_{OH^*} - eU \tag{7.8}$$

$$\Delta G_3 = G_{OOH^*} + G_{(H^+ + e^-)} - G_{O^*} - G_{H_2O_{(l)}} \tag{7.9}$$

$$= G_{OOH^*} + \frac{1}{2}G_{H_{2(g)}} - G_{O^*} - G_{H_2O_{(l)}} - eU \tag{7.10}$$

$$\Delta G_4 = G_* + G_{O_2(g)} + G_{(H^+ + e^-)} - G_{OOH^*} \tag{7.11}$$

$$= G_* + G_{O_2(g)} + \frac{1}{2}G_{H_{2(g)}} - G_{OOH^*} - eU \tag{7.12}$$

The successive intermediates adsorbed on an IrO_2 surface are depicted in figure 7.1. Both bridge-sites and one CUS-site are occupied with oxygen atoms. Notice that this is not our usual reference (see figure 6.1). An oxygen atom is added on one CUS-site to be consistent with work

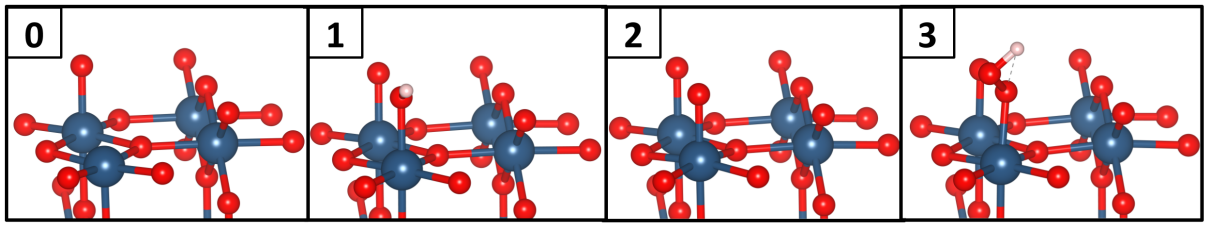

Figure 7.1: Successive steps for OER on IrO_2. Intermediates adsorbed on RuO_2 have similar structure. Numbers in the upper left corners indicate reaction coordinates. Colors denote iridium (blue), oxygen (red), and hydrogen (white) atoms.

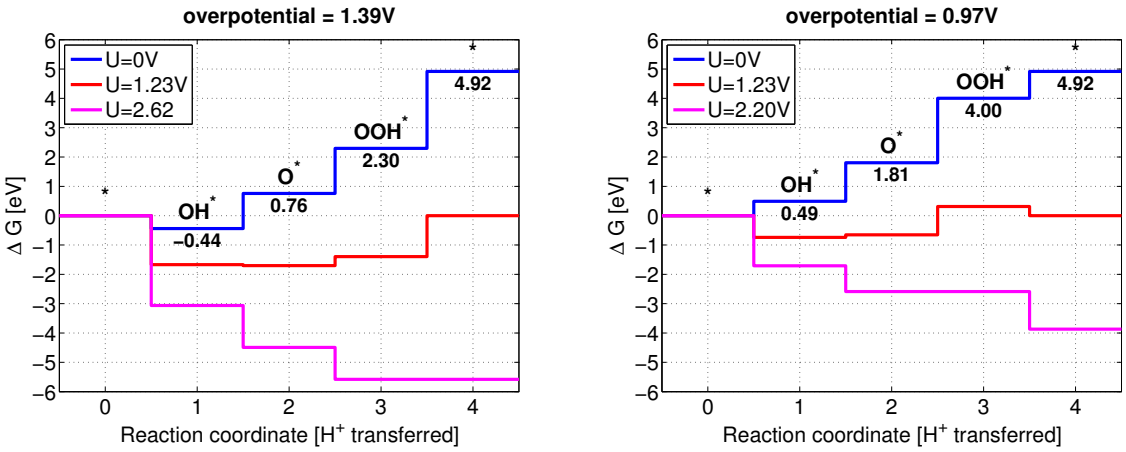

(a) IrO_2 - with vdW (b) IrO_2 - without vdW

Figure 7.2: Free energy diagrams for the OER on IrO_2 with (a) computational parameters described in section 6.2 and (b) without van der Waals correction.

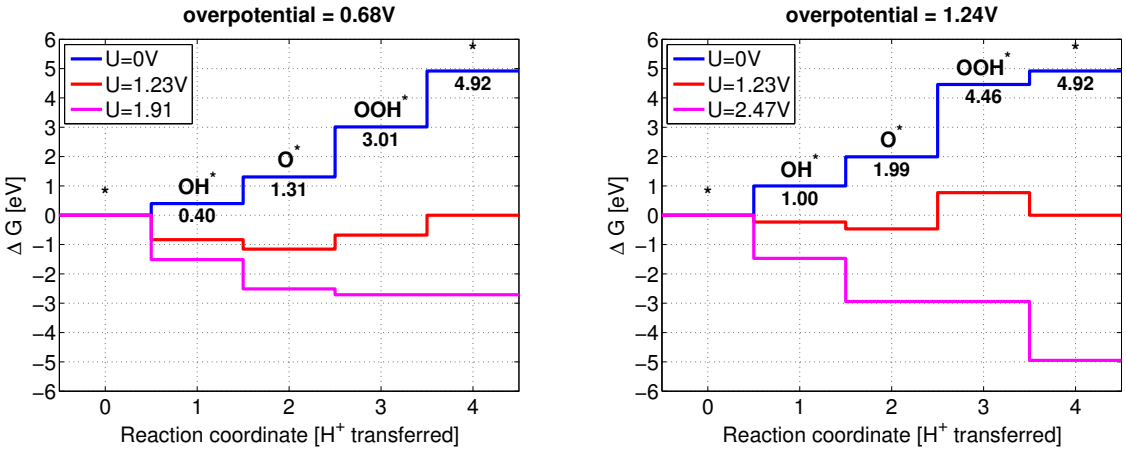

(a) RuO_2 - with vdW (b) RuO_2 - without vdW

Figure 7.3: Free energy diagrams for the OER on RuO_2 with (a) computational parameters described in section 6.2 and (b) without van der Waals correction.

from Karamad *et al.* [55] so a comparison can be made. Intermediates adsorb on the remaining CUS-site.

Figures 7.2 & 7.3 show the free energies of reaction intermediates involved in OER, depicted in figure 7.1. The three different applied potentials correspond to no potential ($U = 0\,V$), the thermodynamical required potential ($U = 1.23\,V$) and the minimal required potential in order to

make all steps downhill in free energy. The overpotential is defined as the latter potential minus $1.23\,V$. All simulations were corrected with ZPE energies. The last reaction step was fixed to $4.92\,V$ in order to avoid the calculation of E^{DFT} for O_2, which is known to be inaccurate [55] and to be consistent with other reference work. Figures 7.2 (a) & 7.3 (a) show the free energy diagrams for IrO_2 and RuO_2 respectively with van der Waals corrections and computational details described in section 6.2. Figures 7.2 (b) & 7.3 (b), again show the free energy diagrams for IrO_2 and RuO_2 respectively, but this time without van der Waals corrections. Clearly, the van der Waals correction makes a very significant difference. Without the van der Waals correction, this model correctly predicts the rate determining step (ΔG_3) and the overall appearance is similar to results from Karamad *et al.* (see figure 4.4). However, the predicted overpotential is divergent from Karamad *et al.*'s calculations ($0.56\,V$ for IrO_2 and $0.37\,V$ for RuO_2) [55]. With the van der Waals corrections, on the other hand, the last step is rate determining (ΔG_4). The most plausible explanation for the divergence with Karamad *et al.*'s work is the disparity in computational parameters and corrections. More specifically, there is no mention of van der Waals and dipole corrections. Moreover, Karamad *et al.* specified using US-PP whereas we use the PAW method.

7.2 Low potential analysis

In this section, we will investigate the stability of intermediates which may play a role at low potential in the Oxgyen Evolution Reaction (OER).

7.2.1 Comparison to reference & influence of ZPE

To make sure we are doing things right, we will first reproduce data from Karamad *et al.*'s work (2015) [27]. In this work, the stability of surface structures of RuO_2 is studied in an aqueous solution. The investigated surfaces are depicted in the insets above figure 7.4. Relative stability diagrams for these surfaces are plotted just below, in figure 7.4. These diagrams were introduced in section 6.3 on page 41 and are used to make comparative stability analyses at a wide range of potentials. At any potential, the line appearing lowest in the diagram corresponds to optimal thermodynamic stability. Whenever applicable, the frames of the pictures depicting structures were given the same color as their corresponding line in the relative stability diagrams.
As can be seen in figure 7.4, the general trend and slopes clearly match. However, crossings are a bit off due to a slight offset. In particular, the hydrogenated structures ($b-H$ & $H-H$) make a very good fit, whereas structures containing oxygen ($b-OH$, $b-O$ & $O-O$) are shifted 0.5 to $1\,eV$ down in figure 7.4 (a) as compared to the reference in figure 7.4 (b). This is probably due to a different computational parameterization in Karamad *et al.*'s work. It was namely specified that dipole and polarization corrections have been neglected [27]. On the other hand, in Karamad *et al.*'s work solvation corrections are accounted for.
To assess the influence of ZPE on the computations, the same stability analysis as in figure 7.4 was performed, but this time without including ZPE corrections. First, table 7.1 shows ZPE values for intermediates used in figure 7.4, both on bridge- and CUS-sites, and compared to reference values [27].
Computed ZPE values correlate very well to reference values [26]. Furthermore, it can be observed that ZPE corrections computed for the same intermediates on CUS- and bridge sites are equivalent. The ZPE energy appears to increase linearly with the addition of an oxygen atom. However, this correlation is not verified with the addition of a hydrogen atom. Figure 7.5 depicts the influence of ZPE on the previously performed analysis (see figure 7.4).
The ZPE correction has obviously a significant impact. However, both with and without including ZPE, the model makes the same prediction on the most stable intermediates. More specifically, both with and without ZPE correction, intermediates $O-O$, $b-OH$ and $H-H$ are successively

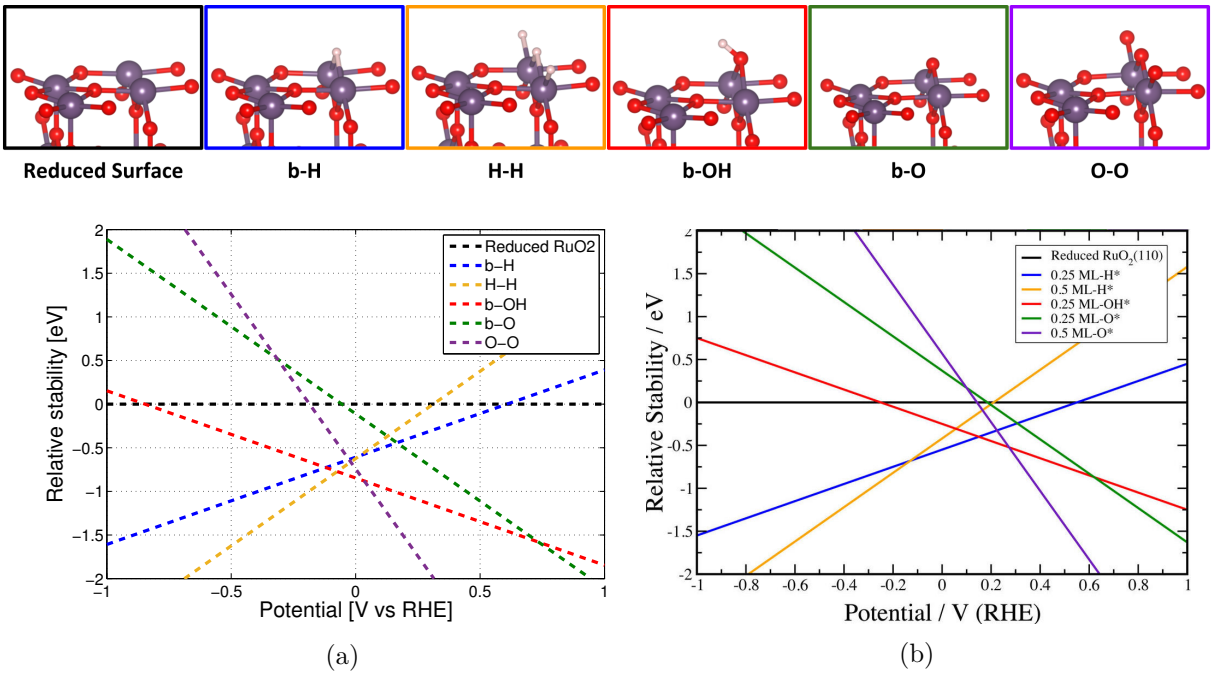

(a) (b)

Figure 7.4: Relative stability diagram of surface structures of RuO_2 in aqueous solution. Results in (a) are compared to results from Karamad *et al.* (b) [27]. Computations include ZPE corrections. Stability is referenced to reduced RuO_2 depicted in the outer left inset (Ru: purple, O: red, H: white). The legend in figure (a) gives the adsorbates on both bridge-sites. A lowercase 'b' denotes a bare bridge-site.

	bridge-site	**CUS-site**	**Karamad *et al.* [26]**
H-b	0.19	/	/
H-H	0.32	/	/
O-b	0.07	0.07	0.08
O-O	0.15	0.14	/
OH-b	0.35	0.35	0.35
OOH-b	/	0.43	0.4

Table 7.1: Overview of ZPE corrections computed for given intermediates on bridge- and CUS-sites as compared to a reference value [26]. A '/' indicates the calculation was not performed or the data was not available. All values are given in eV.

most stable in a certain potential range from -1 to $1\,V$. For this reason and due to the important additionally required computational cost, ZPE energies will only be included in free energy diagrams, where accuracy is crucial for proper interpretation, but not in relative stability diagrams.

7.2.2 Adsorbates inventory study

Following the reproduction of Karamad *et al.*'s structures, other intermediates possibly intervening in the OER were listed and computed. First, two categories were distinguished: structures with bare CUS-sites and structures with water on both CUS-sites. On the bridge-sites, different combinations of H^*, O^* and OH^* adsorbates were listed. Both IrO_2- and RuO_2 slabs were investigated. In figure 7.6, for the sake of clarity, only the most stable structures were represented in the relative stability diagrams. An overview of the entire batch of simulated structures can be found in appendix A.1. In the following plots "cu:" denotes adsorbates present on both CUS-sites

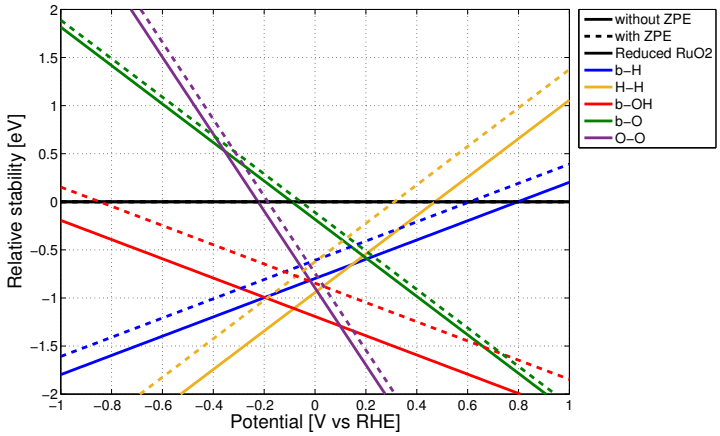

Figure 7.5: Analysis on the influence of ZPE on the stability of RuO_2 intermediates in aqueous solution.

and "br:" denotes adsorbates on both bridge-sites. A lowercase "b" denotes a bare site.
Comparing IrO_2 to RuO_2 (figures 7.6 (a) and (b) respectively to figures 7.6 (c) and (d)), one can see the same succession of structures are most stable (from right to left the order of successive lowest structures is identical). However, crossings are slightly shifted and adsorbates appear more stable on RuO_2 than on IrO_2 ($\sim 1\,eV$). On the other hand, when comparing structures with bare CUS-sites to structures with water-covered CUS-sites, one can conclude all slopes and crossings are very similar, but water-covered sites (figures 7.6 (b) and 7.6 (d)) are shifted down 2 to 3 eV and thus exhibit increased stability with respect to structures with bare CUS-sites (figures 7.6 (a) and 7.6 (c)).
From figure 7.6, we can select a subset of structures which exhibit enhanced thermodynamic stability and thus increased probability to play a role during OER or RHE. Indeed, in all four plots, the surface shifts from oxygen-covered bridge sites at higher potentials towards hydrogen-covered bridge sites at lower potentials, while transiting through intermediate structures (namely br:$OH-O$, br:$OH-OH$, br:$OH-H$).
Based on this ascertainment, a second batch of structures was listed, restricted to the intermediates cited above. This time however, these same selected adsorbates were not only positioned on bridge-sites, but also on CUS-sites, in an attempt to find even more stable structures. An additional twenty structures were constructed, both on IrO_2 and RuO_2. The relative stability diagrams of all these structures can be found in appendix A.2. However, for the sake of clarity, it was chosen to represent only the most stable intermediates, depicted in figure 7.7.
Both on IrO_2 and RuO_2 the same intermediates are thermodynamically most stable, with the exception of structure 1, which only appears as a minimum on RuO_2. Moreover, on IrO_2 the fully hydrogenated surface (structure 4) becomes predominant much faster than on RuO_2, where water on the CUS-site (structures 1,2,3) seems to be stable up to lower potentials.
The same trend comes out both in figure 7.6 and 7.7. Indeed, towards negative potentials, the surface is reduced. This goes along with the adsorption of hydrogen and the desoprtion of oxygen. On the other hand, towards positive potentials, the surface is oxidized. This happens through the desoprtion of hydrogen and the adsorption of oxygen.

7.2.3 Other structures

H_2O on bridge-sites

In an attempt to identify stable structures of IrO_2 and RuO_2 in aqueous solutions, the stability of water on bridge-sites was investigated. Also here, a consistent batch of structures was selected

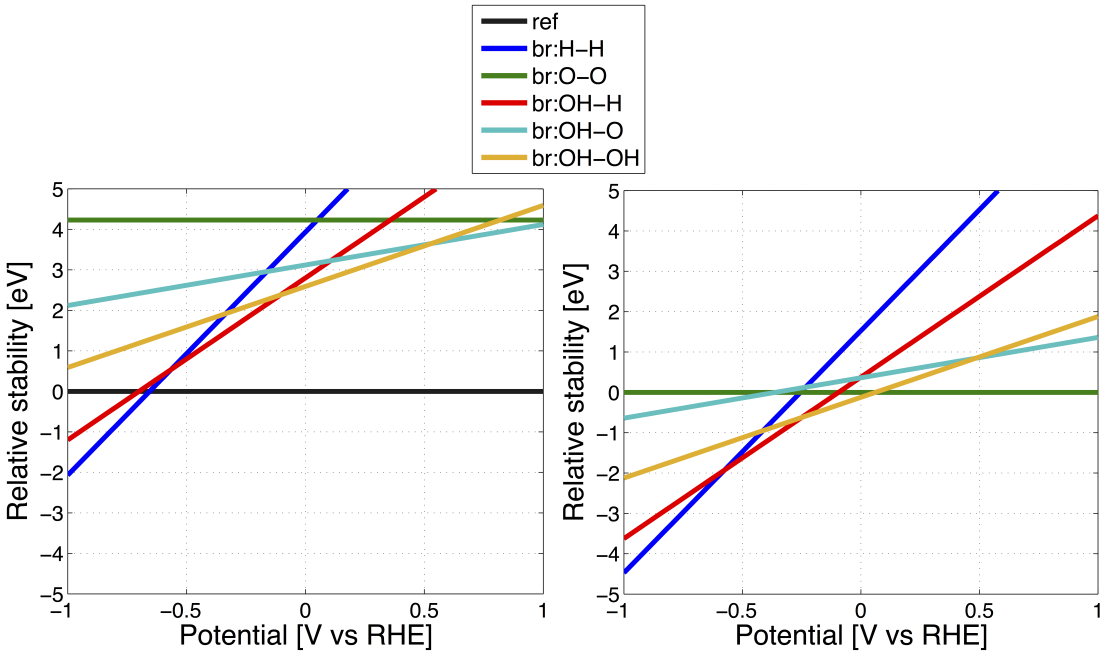

(a) IrO_2 - cu:b-b

(b) IrO_2 - cu:H_2O-H_2O

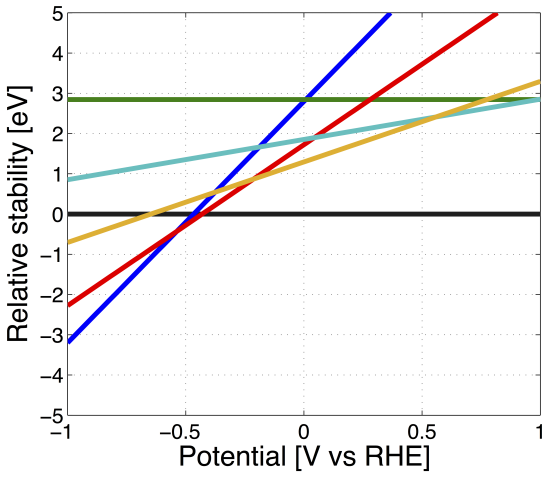

(c) RuO_2 - cu:b-b

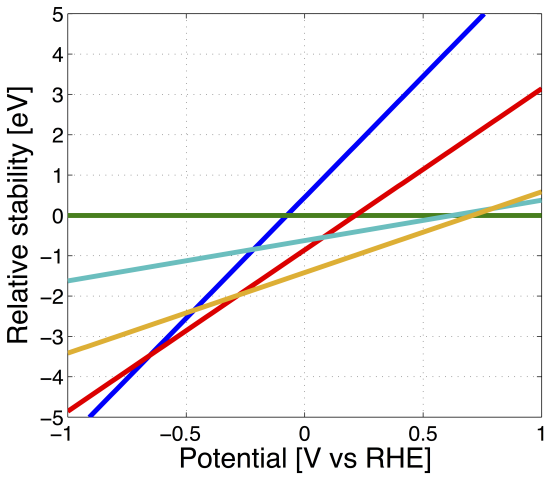

(d) RuO_2 - cu:H_2O-H_2O

Figure 7.6: Relative stability diagrams for a first selection of most stable OER intermediates on IrO_2 (a-b) and RuO_2 (c-d) slabs. In figure (a) and (c) both CUS-sites are left bare, whereas in figure (b) and (d) both CUS-sites are occupied by water. Occupation on bridge sites is mentioned in the common legend above the figures. In all figures, the reference is cu:H_2O-H_2O – br:O-O on an IrO_2 or RuO_2 slab respectively.

and simulated. We can distinguish structures with bare CUS-sites and structures with water on both CUS-sites. Bridge sites were either both covered with water molecules, or one of them was left bare. Structures with one bridge occupied with water and one with hydrogen were also simulated. This was originally to avoid a water molecule to dissociate on a bridge site left bare. However, in the end it appeared water molecules could adsorb on bridge sites without dissociating.

The overall conclusion is that the adsorption of water on bridge sites is difficult, but nonetheless possible. To illustrate this statement, simulation results are presented in table 7.2.

From table 7.2, it appears that H_2O is too bulky to adsorb on the bridge site when water is already adsorbed on the CUS-sites or when both bridge sites are occupied with water. However,

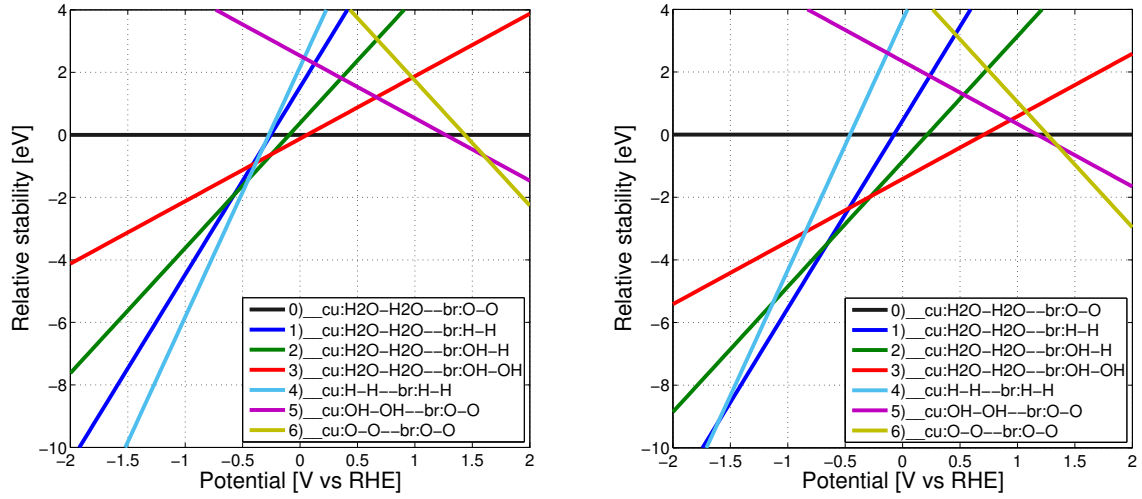

(a) IrO_2 (b) RuO_2

Figure 7.7: Relative stability diagrams for a second selection of most stable OER intermediates on (a) IrO_2 and (b) RuO_2 slabs. Both legends are identical.

	br:H_2O-b	**br:H_2O-H**	**br:H_2O-H_2O**
cu:b-b	✓	✓	✗
cu:H_2O-H_2O	✗	**IrO_2 : ✗ – RuO_2 : ✓**	✗

Table 7.2: Overview of simulated structures with water on bridge sites. A ✓ denotes the water molecule(s) has adsorbed, whereas a ✗ denotes the water molecule(s) did not adsorb. If not specified, the result is valid both for IrO_2- and RuO_2 slabs.

when water manages to adsorb on a bridge-site, it turns out to be a relatively stable structure, as can be seen in figure 7.8.

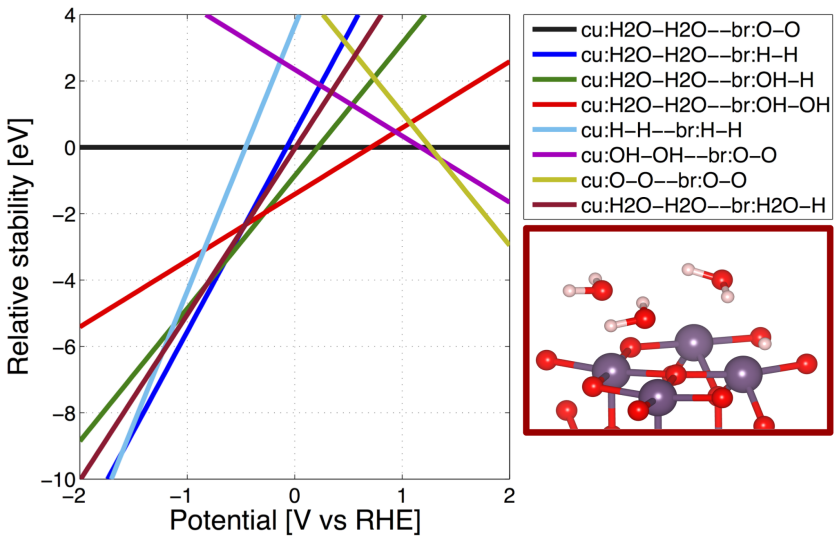

Figure 7.8: Relative stability diagram comparing the stability of water-covered bridge-sites to the selection of most stable OER intermediates on RuO_2.

Screening of new adsorption sites

(a) **Interposed hydrogen on bridge-site**
As shown in figure 7.9, it was attempted to interpose a hydrogen atom in between two bridge oxygen atoms. In this configuration, the interposed hydrogen atoms are positioned right on top of an Ir/Ru atom. In figure 7.9, the upper row depicts the initial structures, whereas the lower row shows the structures after relaxation. In most cases, the structures relaxed to form OH^* adsorbates or water. However, in one case (3b) a new equilibrium position emerged. Indeed, the hydrogen atoms relaxed not in their original position, but were shifted towards the CUS-sites while remaining in between two bridge sites. The stability of this structure is shown in figure 7.11 in the same color as its frame and with circular markers, as compared to previously described intermediates. Clearly this new system does not exhibit interesting stability.

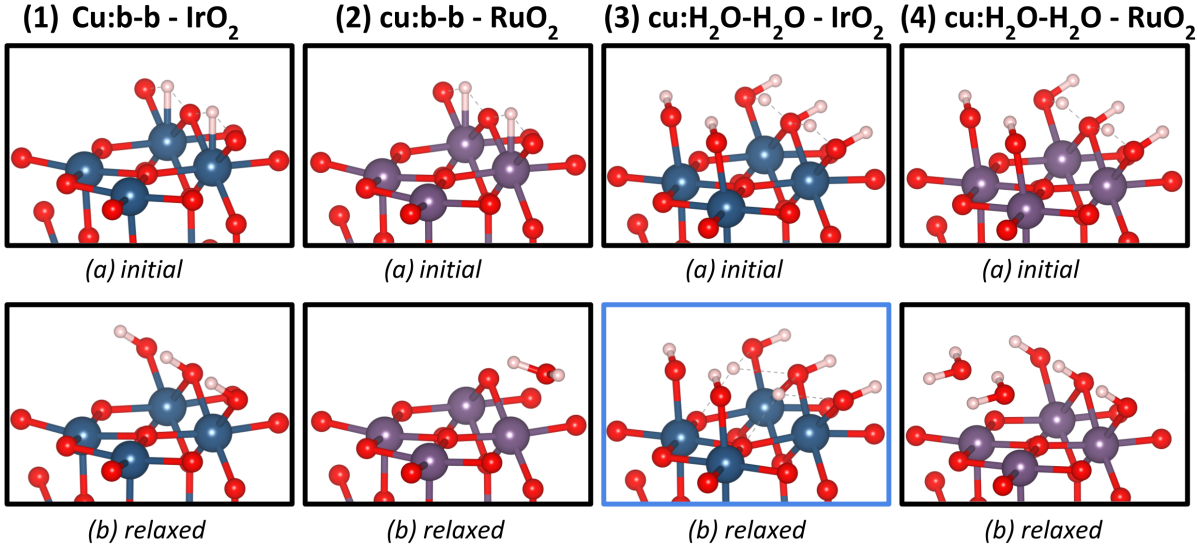

Figure 7.9: IrO_2 (1-3) and RuO_2 slabs (2-4) with interposed hydrogen atoms on the bridge-sites. The upper row show initial structures, whereas the lower row shows relaxed structures. Colors denote iridium (blue), ruthenium (purple), oxygen (red) and hydrogen (white) atoms.

(b) **Shifted oxygen on bridge-site**
Let us investigate a structure with shifted bridge oxygen atoms. This time, we are not interposing additional atoms as in the previous paragraph, but the existing bridge oxygen atoms are simply shifted on top of Ir/Ru atoms. Four slabs were constructed: both with bare and with water-covered CUS-sites and both with only one or two shifted oxygen atoms. These four structures were also constructed on RuO_2 slabs. The relaxed structures are depicted in figure 7.10. Only IrO_2 slabs are depicted because relaxation on RuO_2 slabs resulted in the exact same structures. As opposed to the interposed hydrogen atoms, this time the oxygen atoms remain stable in their shifted position. The stability of the color-framed structure is compared to previously studied intermediates in figure 7.11 (yellow circular markers). Again this new structure does not show interesting stability.

(c) **Shifted hydrogen on bridge-site**
Finally, when discovering that hydrogen-covered surfaces become very stable at low potentials, it was attempted to shift bridge-hydrogen atoms on top of Ir/Ru atoms. The structure is depicted in figure 7.12 (a). However, when relaxing this structure, the bridge-hydrogen atoms recover their original position, as depicted in figure 7.12 (b). The same result is obtained on RuO_2 slabs.

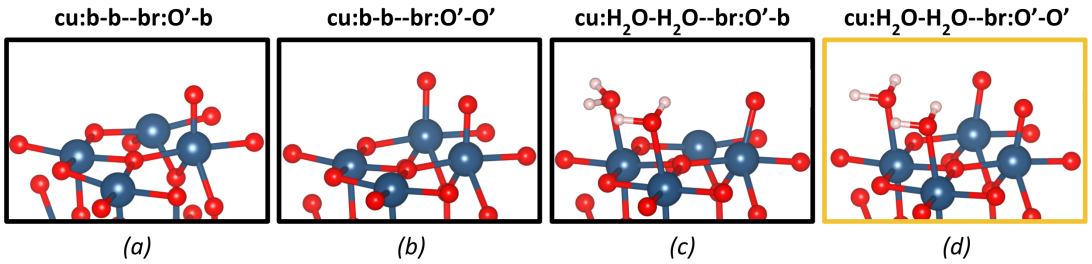

Figure 7.10: IrO_2 slabs with shifted bridge-oxygen atoms. Full configuration is indicated above each image. An apostrophe denotes a shifted atom.

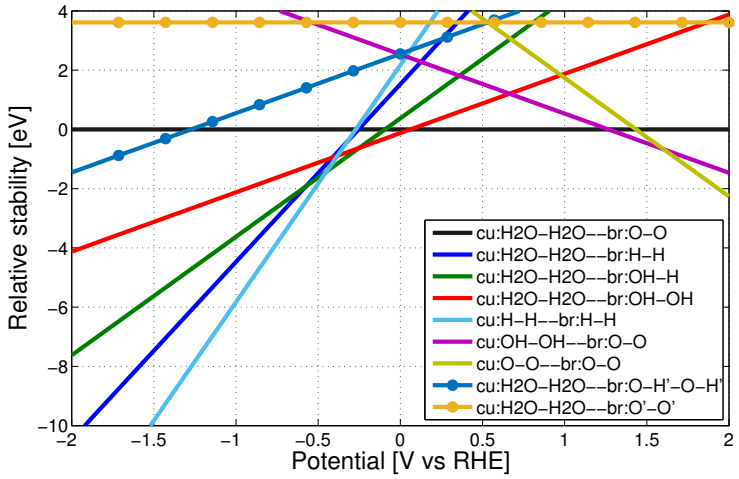

Figure 7.11: Relative stability diagram for OER intermediates on an IrO_2 slab. The two bottom structures in the legend correspond to structures from figures 7.9 and 7.10 and are indicated with circular markers. Atoms shifted from their usual position are denoted with an apostrophe. Colors denote iridium (blue), oxygen (red) and hydrogen (white) atoms.

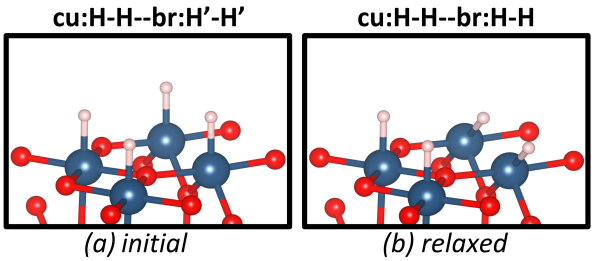

Figure 7.12: Hydrogen-covered IrO_2 slabs with shifted bridge-hydrogen atoms. An apostrophe denotes a shifted atom. Both initial (a) and relaxed structures (b) are depicted.

Ir_2O & Ir_2O_3 surface reconstructions

At last, the stability of the OER intermediates is compared to surface reconstructions. The structures in this section are inspired from the work of Ünal [60] *et al.*, where TiO and Ti_2O_3 reconstructions are investigated on TiO_2 slabs, which have the same rutile structure as IrO_2. These structures were reproduced on IrO_2 slabs and are denoted as Ir_2O and Ir_2O_3. Notice these notations only refer to the surface of the slab. The bulk of the material still consists of IrO_2. Due to the geometry of these reconstructions, new supercells have been used for simulation. The supercell is twice as big in the **a**-direction. Therefore, the k-point grid was halved in this direction. Other computational parameters are identical to what has been done before. Each

supercell has now 4 CUS-sites and 4 bridge sites. These structures are depicted in figure 7.13.

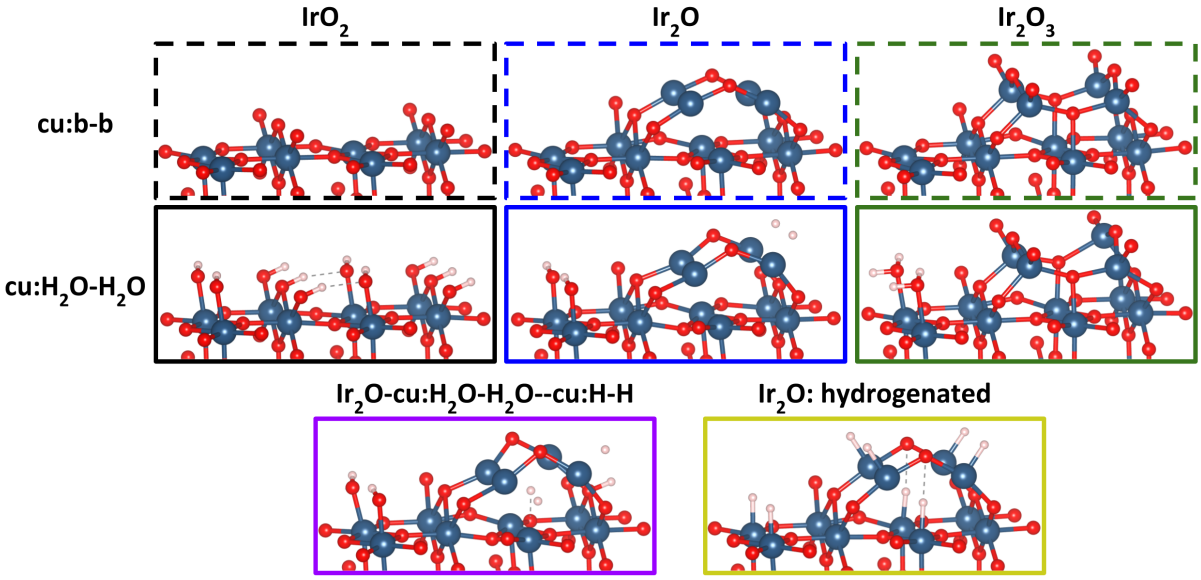

Figure 7.13: IrO_2 surface reconstructions.

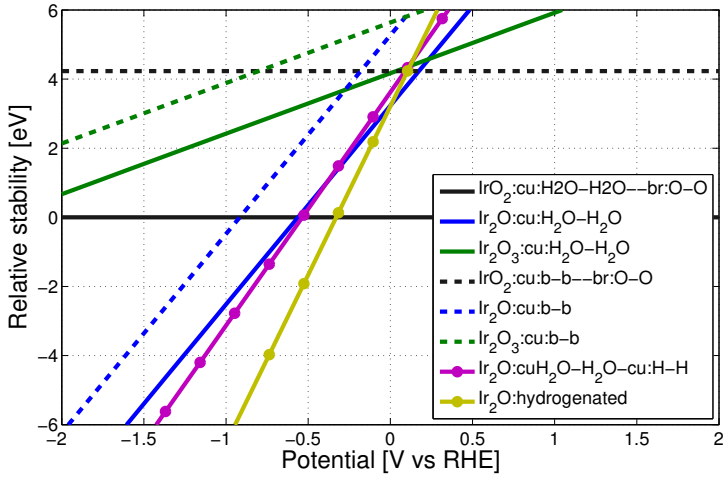

Figure 7.14: Relative stability diagram of surface reconstructions on IrO_2. Structures are depicted in the insets (Ir: blue, O: red, H: white). Solid lines indicate water on CUS-sites, whereas dashed lines denote bare CUS-sites. Lines with circular markers do not belong to any category.

For both types of surface reconstructions (Ir_2O & Ir_2O_3), computations were performed both with and without water on CUS-sites. Moreover, due to the increased stability of hydrogenated surfaces (as can be seen in figure 7.11), hydrogen-covered surfaces were also computed (lower structures in figure 7.13). Finally, a fully-hydrogenated Ir_2O_3 structure was simulated (with hydrogen atoms on upper oxygen atoms), but this configuration turned out to be unstable and did not relax until convergence. An attempt to adsorb more water on the top iridium atoms of the Ir_2O surface also failed. As can be seen in figure 7.14, at zero applied potential, the surface reconstructions (blue & green lines) are not favorable compared to IrO_2 (black lines). Nonetheless, the Ir_2O reconstruction is more stable than the Ir_2O_3 reconstruction in the negative potential range. The Ir_2O reconstructed surfaces only become favorable at roughly $-0.25\,V$ with bare CUS-sites and $-0.5\,V$ with water on CUS-sites compared to the their respective IrO_2 reference slab. However, the hydrogenated Ir_2O surface exhibits interesting stability at relatively

low applied potential. In figure 7.15, the stability of this structure is compared to the selection of the so far most stable structures.

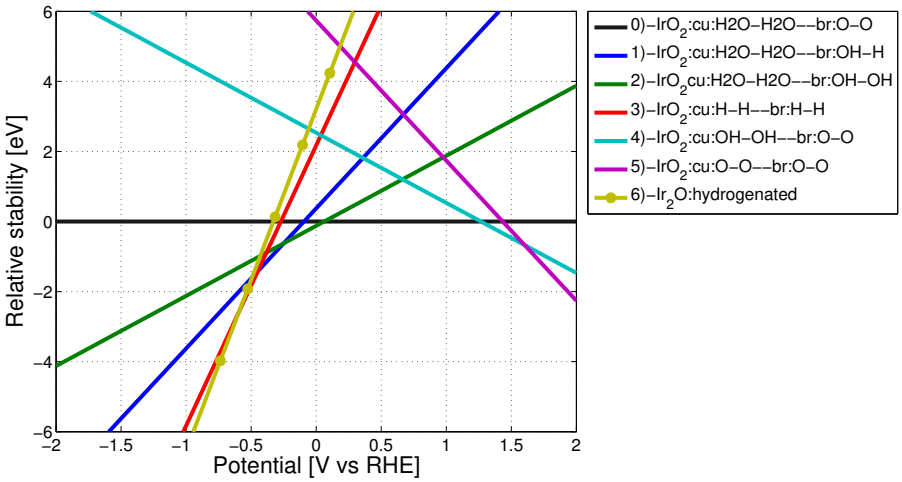

Figure 7.15: Relative stability diagram of the most stable reconstructed surfaces (hydrogenated Ir_2O) (line with circular marker) compared to the most stable intermediates on IrO_2 (no marker).

As can be seen in figure 7.15, at $-0.52\,V$, the reconstructed Ir_2O surface becomes slightly more stable than the fully hydrogenated IrO_2 surface.

7.3 Discussion

In this chapter, we have proceeded through a twofold analysis. First, standard free energy diagrams for the OER were reproduced both on IrO_2 and RuO_2. At this point, we have shown the importance of corrections such as the vdW and ZPE energies for the analysis of free energy diagrams and for the estimation of overpotentials.
Second, possible OER intermediates were investigated at low potential. First we started with classic OER intermediates such as H^*, O^* and OH^*, positioned on the conventional adsorption sites. This enabled to identify a first selection of structures exhibiting optimal stability (see figure 7.7). Next, we tried to adsorb water on bridge-sites, which did not reveal notable stability. Then, it was attempted to shift adsorbates from their usual position and to interpose protons between bridge-oxygen atoms. These structures did not reveal interesting stability either. At last, we investigated surface reconstructions such as Ir_2O and Ir_2O_3. In the negative potential range, the hydrogenated Ir_2O surface exhibited competing stability with a hydrogenated IrO_2 surface.

The last step of the analysis consists in interpreting our computational observations in the light of the experimental measurements. It is important to realize that our computations and the relative stability diagrams only reflect the thermodynamic stability of a certain structure. However, before a surface can actually take form, many other aspects must be considered. Let us have a look at figure 7.15 to illustrate this point. The analysis is done on IrO_2 to include surface reconstructions. However, similar intermediates are involved on RuO_2 and therefore this discussion is fully applicable to RuO_2 slabs. First, remember theoretically at $0\,V$ and below the hydrogen evolution becomes thermodynamically favorable. Therefore, if experimentally the HER takes place, the formation of hydrogen-covered surfaces such as structures 3 and 6 in figure 7.15 might be compromised. Second, although two structures are thermodynamically stable and form a crossing does not mean it is kinetically possible for the surface to transit from one configuration

to the other. For example, consider structures 3 and 1 in figure 7.15. The oxidation reaction going from Ir_2O-cu:H-$H - br$:H-H (3) to Ir_2O-cu:H_2O-$H_2O - br$:OH-H (1) is given as:

$$(3) + 3H_2O \rightarrow (1) + 4H^+ + 4e^- \tag{7.13}$$

This reaction requires a 4-electron process, which is quite complex to be achieved. This gives an indication of the complexity of the reaction which must underlie the transfer from IrO_2 to a surface reconstruction such as hydrogenated Ir_2O (structure 6). However, it is worth noting that each step in the successive oxidation from structure 1 to structure 5 (reaction $(1) \rightarrow (2) \rightarrow (0) \rightarrow (4) \rightarrow (5)$) requires a two electron transfer.
With this analysis it has become clear that our relative stability diagrams should be interpreted with care. Many considerations should be taken into account before we can conclude a stable surface might be intervening experimentally.

Chapter 8

CO_2 Reduction Reaction

The content of this chapter largely emanates as a reflection on Karamad *et al.*'s work [27]. In their article entitled "Mechanistic Pathway in the Electrochemical Reduction of CO_2 on RuO_2", also discussed in chapter 5, Karamad *et al.* explore reaction intermediates and pathways to reduce CO_2 on RuO_2. In this chapter, we will verify Karamad *et al.*'s hypotheses and extend the discussion to IrO_2 slabs.

8.1 Comparison to reference & influence of ZPE

Let us start by comparing some standard results to Karamad *et al.*'s work. In this scope, a couple of intermediates depicted in the insets of figure 8.1 were simulated. Relative stability diagrams are depicted in figure 8.1 (a), as opposed to Karamad *et al.*'s results in figure 8.1 (b).

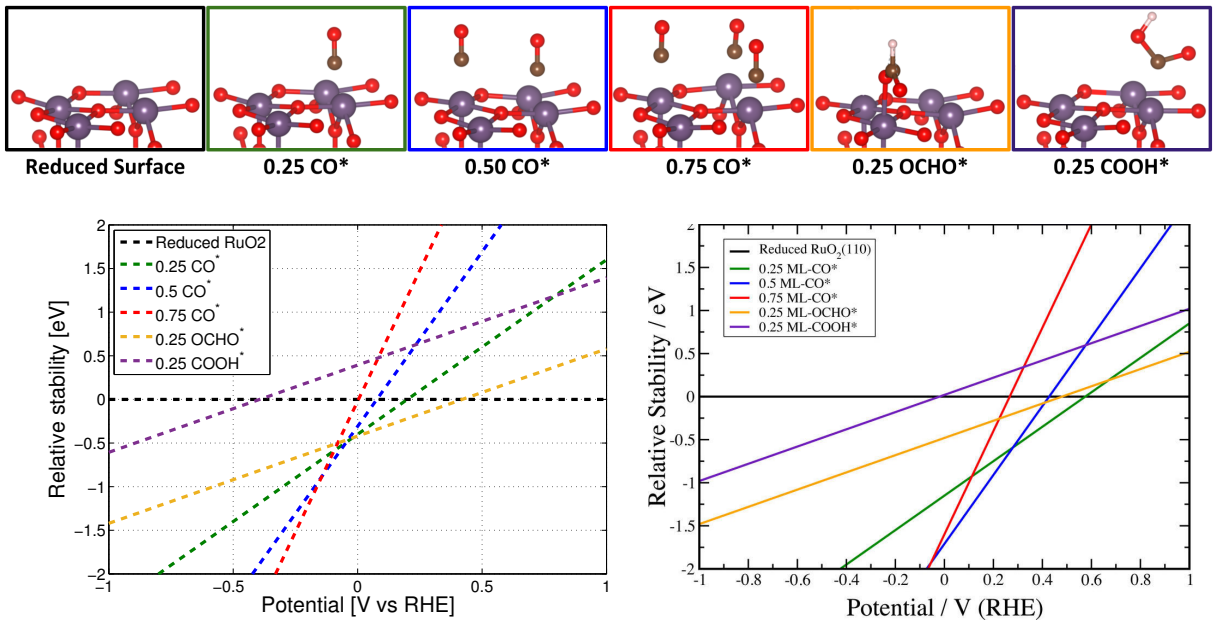

(a) (b)

Figure 8.1: Relative stability diagram of carbonated surface structures on RuO_2. Results in (a) are compared to results from Karamad *et al.* (b) [27]. Computations include ZPE corrections retrieved from Karamad *et al.* [26]. Stability is referenced to reduced RuO_2 depicted in the outer left inset (Ru: purple, O: red, H: white, C: brown).

From figure 8.1, one can conclude that slopes correctly correlate. Whereas 0.25 $OCHO^*$ almost exactly fits Karamad *et al.*'s result, all other slopes seem to be shifted approximately half an

eV upwards. Again, this discrepancy may arise from different computational parameterization, as was discussed in section 7.2.1. Indeed, in his work, no dipole or polarization corrections are applied, but solvation corrections were accounted for. He also mentions to apply a $0.45\,eV$ correction on $CO_2(g)$ to account for the bad description of the OCO backbone in RPBE, which may affect future results.

Let us now assess the influence of the ZPE corrections. As opposed to results discussed in chapter 7, in this case ZPE corrections were not computed, but simply retaken from Karamad *et al.* [26]. Indeed, following the discussion from section 7.2.1, it can be concluded that our ZPE computations sufficiently correlate with Karamad *et al.*'s data to use them consistently. Figure 8.2 depicts the stability of the same structures as in figure 8.1, but this time computed both with (dashed line) and without (solid line) ZPE correction.

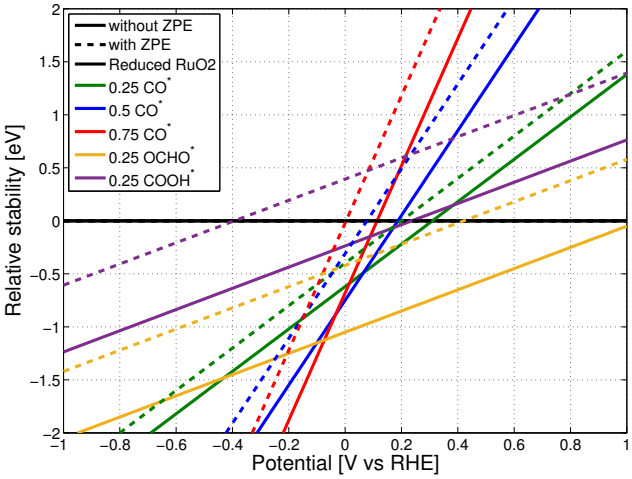

Figure 8.2: Analysis on the influence of ZPE on the stability of carbonated RuO_2 intermediates.

Obviously, the ZPE correction again has a significant impact. Notice the generated shift is much larger for bulky intermediates ($OCHO^*$, $COOH^*$) than for small intermediates (CO^*).

8.2 CO^* coverage analysis

In their work [27], Karamad *et al.* claim that the first step in the reduction mechanism of CO_2 on RuO_2 is the formation of a CO^* adsorbate. This is a 2-step reaction reminded below:

$$\begin{aligned} {}^* + CO_2 + (H^+ + e^-) &\rightarrow COOH^* && \Delta G_1 \\ COOH^* + (H^+ + e^-) &\rightarrow CO^* + H_2O && \Delta G_2 \end{aligned} \tag{8.1}$$

Notice that this requires the formation of a $COOH^*$ adsorbate, which might not be kinetically accessible. Karamad *et al.* suggest CO^* will build up on the reduced RuO_2 surface under CO_2 reduction. This hypothesis is supported by the high desorption energies and very low Faradaic efficiency experimentally observed for CO production on RuO_2 [56]. To estimate the CO^* coverage, the formation of $COOH^*$ was taken into account. It was reported that the $COOH^*$ intermediate becomes thermodynamically favorable at potentials below $-0.02\,V$ on the reduced RuO_2 surface and at $-0.41\,V$ on the 0.25 CO^* covered surface. Therefore, it was concluded that within this potential range, the CO^* coverage is expected to be somewhere in between 0.25 and 0.5. Based on this statement, Karamad *et al.* selected two limiting starting structures to further investigate CO_2 reduction. These are the 0.25 CO^* and 0.5 CO^* coverage on the reduced RuO_2 surface. Both structures are depicted in the insets of figure 8.1. In this section,

we will investigate this hypothesis by a comparative analysis of the stability of Karamad *et al.*'s structures with other competing structures.
Before going on, it is important to realize that CO_2 cannot adsorb directly on an IrO_2 or RuO_2 surface. It must first be reduced to another intermediate before adsorption is possible. Moreover, the CO^* adsorbate binds to the surface through the carbon atom and not the oxygen atom. These statements were verified with computations.

8.2.1 CO^* intermediates: stability analysis

In the first place, we will only focus on the stability of carbonated intermediates. A full analysis with comparison to other structures will follow later. An overview of the complete set of selected structures can be found in appendix A.3. The results for a selection of the most interesting structures are given in figure 8.3 for IrO_2 (a) and RuO_2 (b).

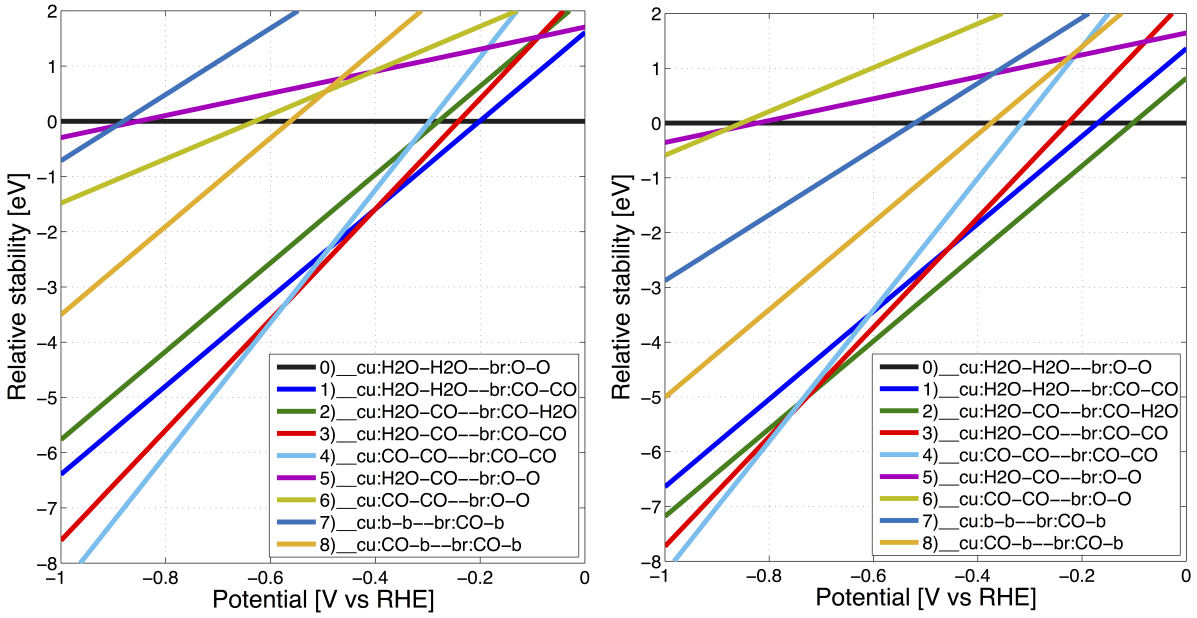

(a) IrO_2 (b) RuO_2

Figure 8.3: Relative stability diagrams of most interesting CO^*-covered structures on (a) IrO_2 and (b) RuO_2 slabs. Legends are identical in both figures.

In this figure, structures 7 & 8 represent Karamad *et al.*'s 0.25 CO^* & 0.5 CO^* coverages respectively. Obviously, these structures are far from being the most stable ones, requiring a minimum of $-0.4\,V$ potential to overtake the stability of structure 0, here defined to be the reference state. But most astonishing, one can see these coverages never become more favorable than other computed structures. Moreover, when looking at the most stable structures (0, 1, 2, 3, 4), it becomes obvious that water remains very stable on the adsorption sites. Indeed, it takes up to $-0.59\,V$ on IrO_2 slabs and $-0.75\,V$ on RuO_2 slabs to completely replace water by CO^* (these are the potentials at which structure 4 becomes most favorable). More specifically, when considering structures 0, 5 and 6, one can conclude it requires a significant potential to replace water by CO^* on CUS-sites. On the other hand, when considering structures 0 and 1, it seems to be thermodynamically not very expensive to have CO^* on bridge-sites instead of O^*.
At last, one can notice the significant increased stability of structure 2 on RuO_2 compared to IrO_2.
To sum up, Karamad *et al.*'s hypothesis to consider 0.25 CO^* and 0.5 CO^* (see insets figure 8.1) coverages for CO_2 reduction does not seem to be very realistic when considering an aqueous medium.

8.2.2 CO^* vs aqueous intermediates: stability analysis

Figure 8.4 depicts the most stable intermediates, from both OER and CO^* coverage analyses. Panel (a) depicts results for IrO_2 and panel (b) for RuO_2.

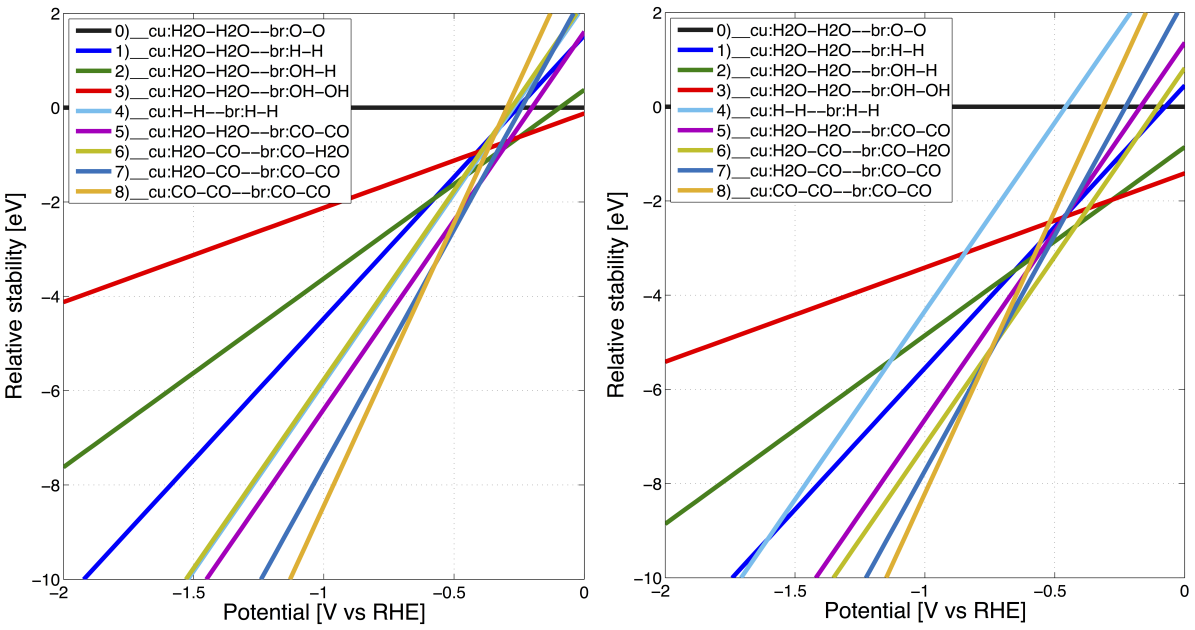

(a) IrO_2 (b) RuO_2

Figure 8.4: Relative stability diagrams of most stable intermediates from both OER and CO^* coverage analysis. Legends are identical in both figures.

As can be seen in this figure, there exists a turnover potential, at which CO^* adsorbates (structures 5 - 8) become more stable than OER adsorbates (structures 0 - 4). This potential is $-0.30\,V$ for IrO_2 and $-0.42\,V$ for RuO_2. When decreasing potential further, we can see for IrO_2, it is more favorable to have H_2O^* on CUS-sites, and CO^* on bridge-sites (structure 5), whereas RuO_2 prefers alternating H_2O^* and CO^* on bridge- and CUS-sites (structure 6). At last, the fully CO^* covered surface becomes stable at less negative potentials on IrO_2 ($-0.59\,V$) than on RuO_2 ($-0.75\,V$).
From these observations, we can conclude CO^* adsorbs more easily on IrO_2 than on RuO_2. Vice versa, at decreasing potentials, H_2O^* sticks for longer on RuO_2 than on IrO_2.

8.3 Formation of CO^* intermediate

Now that we have studied the overall stability of CO^* covered surfaces, we will here investigate the reaction free energies associated to the formation of the CO^* adsorbate. The overall reaction is given by equation 8.1. The procedure to obtain the reaction free energies is similar to what has been done in section 7.1. When considering successive reaction steps, ZPE corrections have a drastic impact. Therefore, in this section, ZPE corrections from Karamad *et al.* were included [26].

Figures 8.5 and 8.6 depict free energy diagrams for the formation of CO^* on RuO_2 and IrO_2 respectively at $U = 0\,V$ (RHE). The insets of figure 8.5 show the structures represented in the diagrams. The first row of insets show the starting structures. Rows below depict successive reaction steps. The limiting potential required to make all steps exergonic is given in the figure legend. If no value is given, the reaction is already exergonic at $U = 0\,V$.
Comparing figures 8.5 (a) and (b), one can see the general tendency is similar, but an offset shifts our results from Karamad *et al.*'s results. The $COOH^*$ adsorbate on the reduced surface

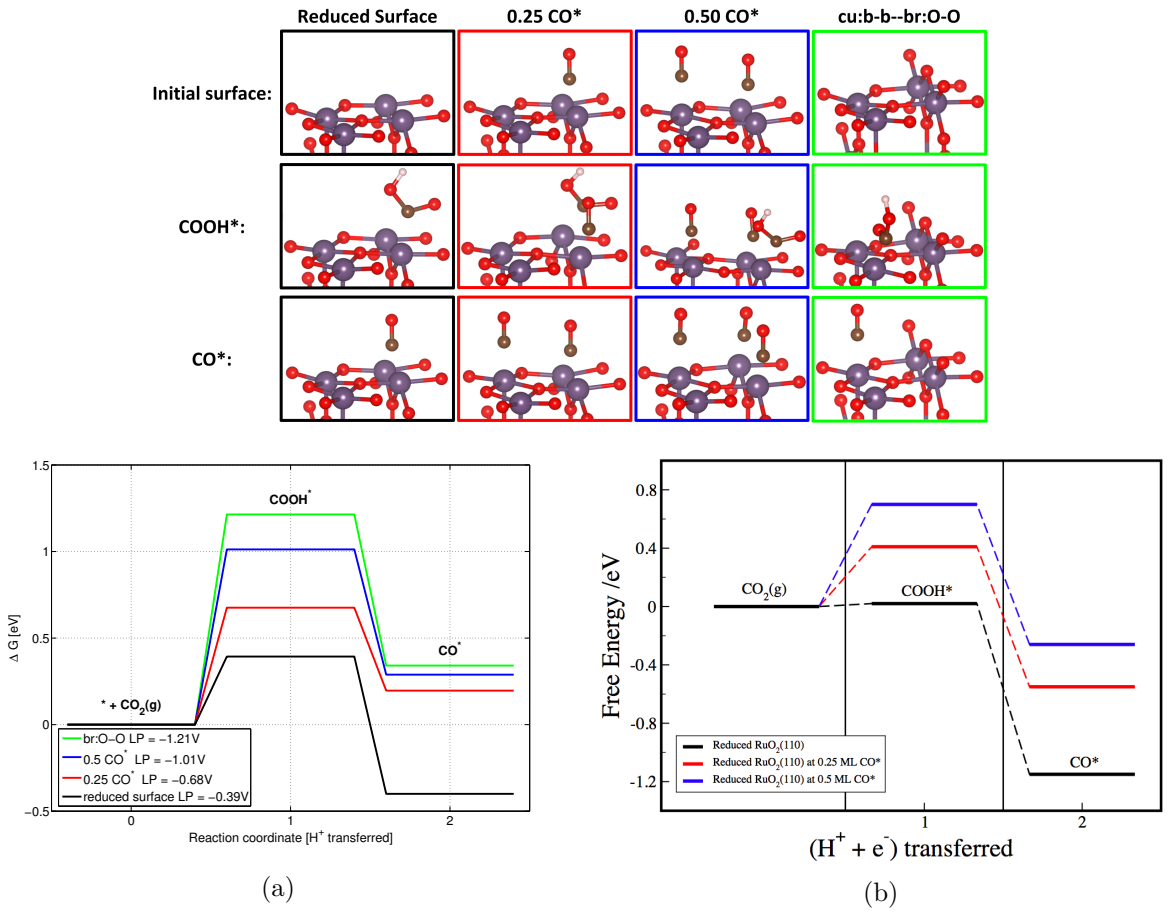

(a) (b)

Figure 8.5: Free energy diagrams for the formation of CO^* on RuO_2 at $U = 0\,V$ (RHE). Results in figure (a) are confronted to results from Karamad *et al.* in figure (b) [26]. Four different coverages are investigated, all depicted in the first row of the insets (Ru: purple, O: red, H: white, C: brown). Rows below depict the surface at successive reaction steps. In the legend of figure (a), LP indicates the limiting potential required to obtain successive downhill reaction steps.

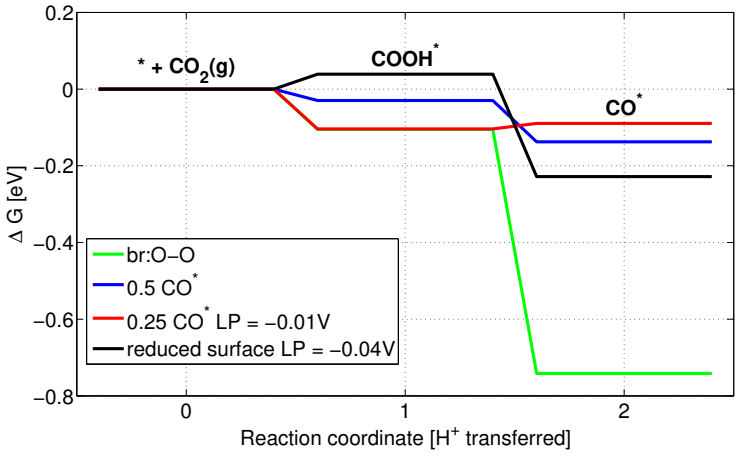

Figure 8.6: Free energy diagram for the formation of CO^* on IrO_2 at $U = 0\,V$ (RHE). Structures corresponding to each reaction step are depicted in the insets of figure 8.5 for RuO_2 slabs, but are identical on IrO_2 slabs.

(black) is shifted $0.4\,eV$ upwards in figure (a) as compared to figure (b). The exact same offset

was observed in figure 8.1. The $COOH^*$ intermediate on other coverages shows a slightly smaller offset. Finally the shift experienced on the last reaction step is slightly larger than for the first reaction step and is in a range of 0.55 to $0.8\,eV$ depending on coverage. As mentioned earlier, this difference is most probably due to a different computational parameterization. Again, it was specified that dipole and polarization corrections have been neglected [27]. On the other hand, in Karamad *et al.*'s work solvation corrections are accounted for. The formation of CO^* has been computed on an additional reference structure. It was indeed observed in previous computations that keeping the bridge-sites occupied with oxygen atoms is thermodynamically more favorable and probably more realistic in an aqueous environment, as compared to a fully reduced surface. In this case, the $COOH^*$ intermediate adsorbs on two CUS-sites. However, on RuO_2, the oxygenated bridge surface requires higher potential than the other investigated structures.
The picture is drastically different when considering an IrO_2 slab (see figure 8.6). Indeed, the formation of CO^* requires a maximal potential of $-0.04\,V$ on the studied surfaces, as opposed to a minimal potential of $-0.39\,V$ on RuO_2. Even more remarkable, the CO^* formation on the 0.5 CO^* and br:$O-O$ IrO_2 structures are exergonic at $U = 0\,V$.
All in all, the formation of CO^* appears to be much more favorable on IrO_2 than on RuO_2. This is in accordance with what is observed in figure 8.4. Moreover, whereas the presence of oxygen atoms on the bridge-sites seems to stabilize the adsorption of $COOH^*$ on IrO_2, it is all the contrary for RuO_2.

8.4 Formation of HCOOH* intermediate

The formation of $HCOOH^*$ is an important step in the reduction of CO_2 to CH_4. Indeed, as will be seen later, this step is potential limiting on a RuO_2 catalyst. Therefore, we will here investigate the most favorable way to produce this intermediate. Two reaction pathways can be distinguished for the formation of $HCOOH^*$. Indeed, this reaction can proceed through a $COOH^*$ or an $OCHO^*$ intermediate. Both reaction pathways are detailed below:

$$\begin{aligned} {}^* + CO_{2(g)} + (H^+ + e^-) &\rightarrow COOH^* \\ COOH^* + (H^+ + e^-) &\rightarrow HCOOH^* \end{aligned} \tag{8.2}$$

$$\begin{aligned} {}^* + CO_{2(g)} + (H^+ + e^-) &\rightarrow OCHO^* \\ OCHO^* + (H^+ + e^-) &\rightarrow HCOOH^* \end{aligned} \tag{8.3}$$

Notice that reaction pathway 8.2 requires the protonation of $COOH^*$ at a carbon atom, whereas the reaction pathway 8.3 requires the protonation of $OCHO^*$ at an oxygen atom. The expressions for the reaction free energies in the framework of CHE are similar to what has been done before and are therefore not detailed here. The different intermediates are depicted in figure 8.7 on 0.25 CO^* RuO_2 slabs. Intermediates for other coverages and on IrO_2 slabs are similar.

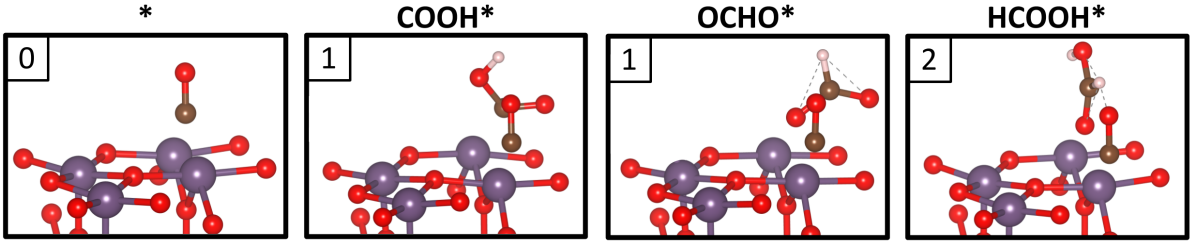

Figure 8.7: Intermediates for the formation of $CHOOH^*$ on 0.25 CO^* RuO_2. Numbers in the upper left corners indicate the reaction coordinate. Colors denote ruthenium (purple), oxygen (red), hydrogen (white) and carbon (brown) atoms.

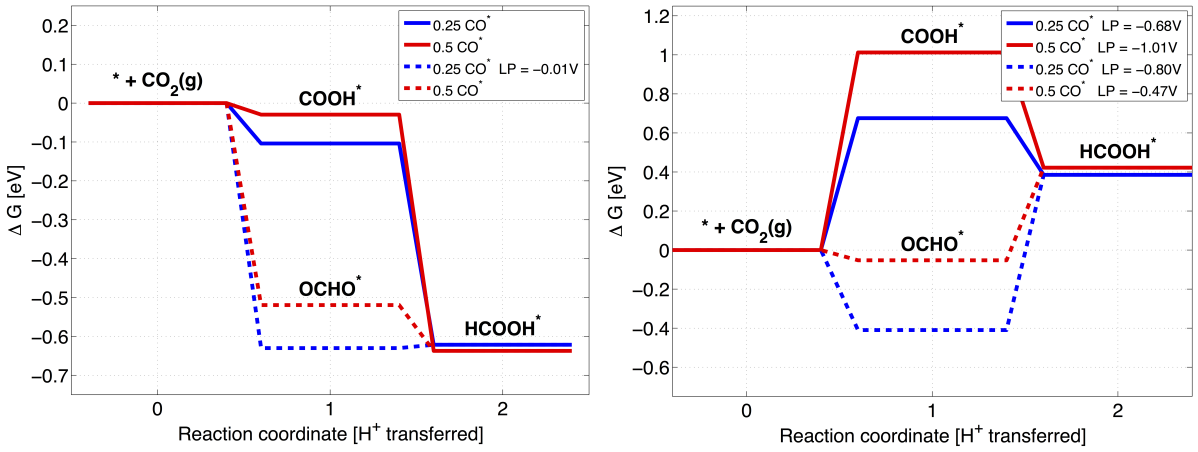

(a) IrO_2 (b) RuO_2

Figure 8.8: Free energy diagrams for the formation of $HCOOH^*$ on IrO_2 (a) and RuO_2 (b) at $U = 0\,V$ (RHE). Two different coverages are investigated: 0.25 CO^* (blue) and 0.50 CO^* (red). Solid and dashed lines show the $COOH^*$ and $OCHO^*$ reaction paths respectively. LP indicates the limiting potential required to obtain successive downhill reaction steps.

As can be seen in figure 8.8, the formation of $HCOOH^*$ on RuO_2 is more favorable through an $OCHO^*$ intermediate. This explains the choice of Karamad *et al.* to proceed through this intermediate for the synthesis of CH_4 [27]. On the other hand, on IrO_2 (figure 8.8 (a)) the choice for the $OCHO^*$ intermediate is less straightforward. Indeed, both reaction paths require no or very little potential to become exergonic. Moreover, although at the first step the $OCHO^*$ intermediate is more stable, the second step becomes limiting with the $OCHO^*$ intermediate (on 0.25 CO^*) coverage. All in all, on IrO_2, both reaction pathways seem to be competing for the formation of $HCOOH^*$.

8.5 Synthesis of $CH_{4(g)}$

Now that we have studied subsequent reactions required for the reduction of CO_2 to CH_4, we can study the overall reaction process. It was chosen to investigate the reaction pathway selected by Karamad *et al.* [27]. The reaction is studied on two different initial structures, namely the 0.25 CO^* and 0.5 CO^* coverages, which were already discussed in previous sections. The successive reaction intermediates are depicted in figure 8.9 for RuO_2. Be aware that, unlike previous structure renderings, in this case the full supercell has been depicted for clarity purposes, which means atoms are repeated on every border of the supercell. On IrO_2, the reaction intermediates are very similar. The numbers in the upper left corner of each structure indicate the reaction coordinate in the free energy diagrams in figures 8.10, 8.11 and 8.12. Figures 8.10 and 8.12 depict the computed free energy diagrams for RuO_2 and IrO_2 respectively. The upper plots are at zero potential, whereas lower plots are at the potentials required to make the reaction exergonic. Figure 8.11 depicts the same diagram extracted from Karamad *et al.*'s work for comparison [27]. When comparing the upper panel in figure 8.10 to figure 8.11, one can see the first four reaction steps have very similar differential free energies. However, reaction steps 5, 6 and 7 are significantly lower in energy in Karamad *et al.*'s plot compared to our computations. Nonetheless, a similar shift is generated by the difference in coverage (blue line vs red line) in our computations and in Karamad *et al.*'s work.
When looking at figure 8.10 (b), one can see the potential limiting step is the protonation of $OCHO^*$ to $HCOOH^*$, at both 0.25 CO^* and 0.5 CO^* coverages. Karamad *et al.* reports the same potential limiting step on 0.25 CO^* coverage, but claims on 0.5 CO^* coverage the

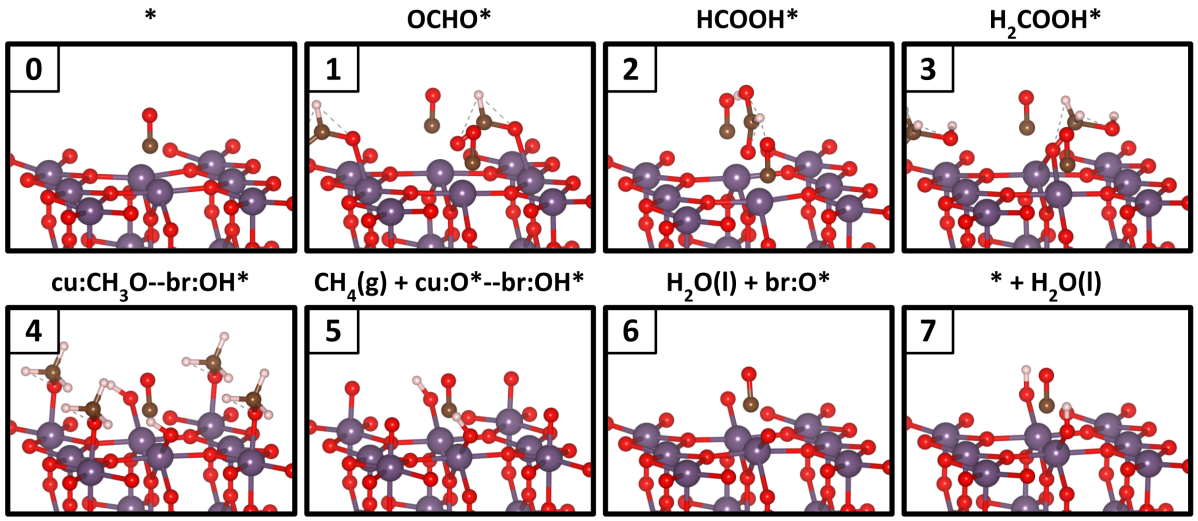

Figure 8.9: Successive intermediates for the reduction of CH_4 on 0.25 CO^* RuO_2. Numbers in the upper left corner of each image indicate the reaction coordinate. Colors denote ruthenium (purple), oxygen (red), hydrogen (white) and carbon (brown) atoms.

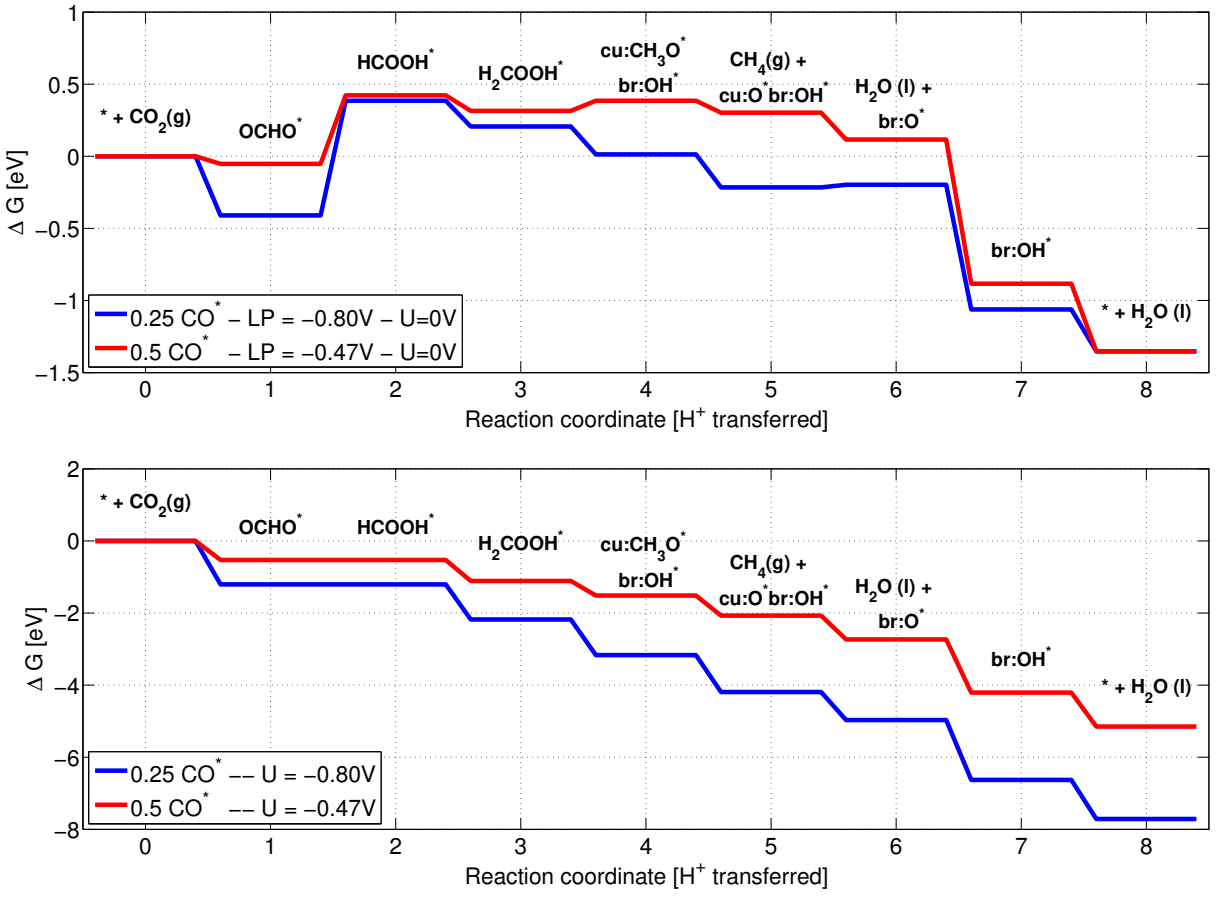

Figure 8.10: Free energy diagrams of CO_2 reduction on RuO_2 at zero potential applied (upper figure) and limiting potential applied (lower figure) at 0.25 CO^* (blue line) and 0.5 CO^* coverage (red line).

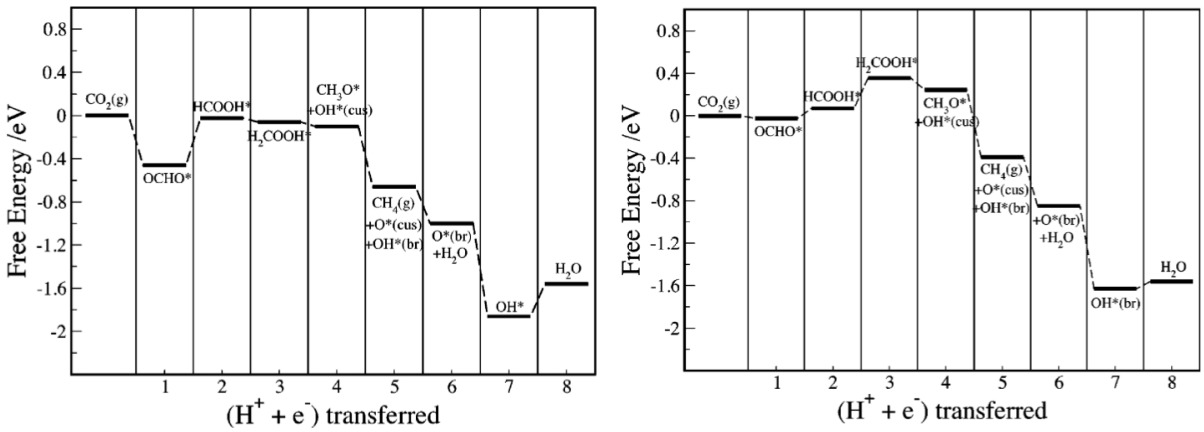

(a) 0.25 CO^* (b) 0.5 CO^*

Figure 8.11: Free energy diagrams for CO_2 reduction on RuO_2 at U = 0V (RHE) at 0.25 CO^* (a) and 0.5 CO^* coverage (b) extracted from Karamad *et al.* for comparison [27].

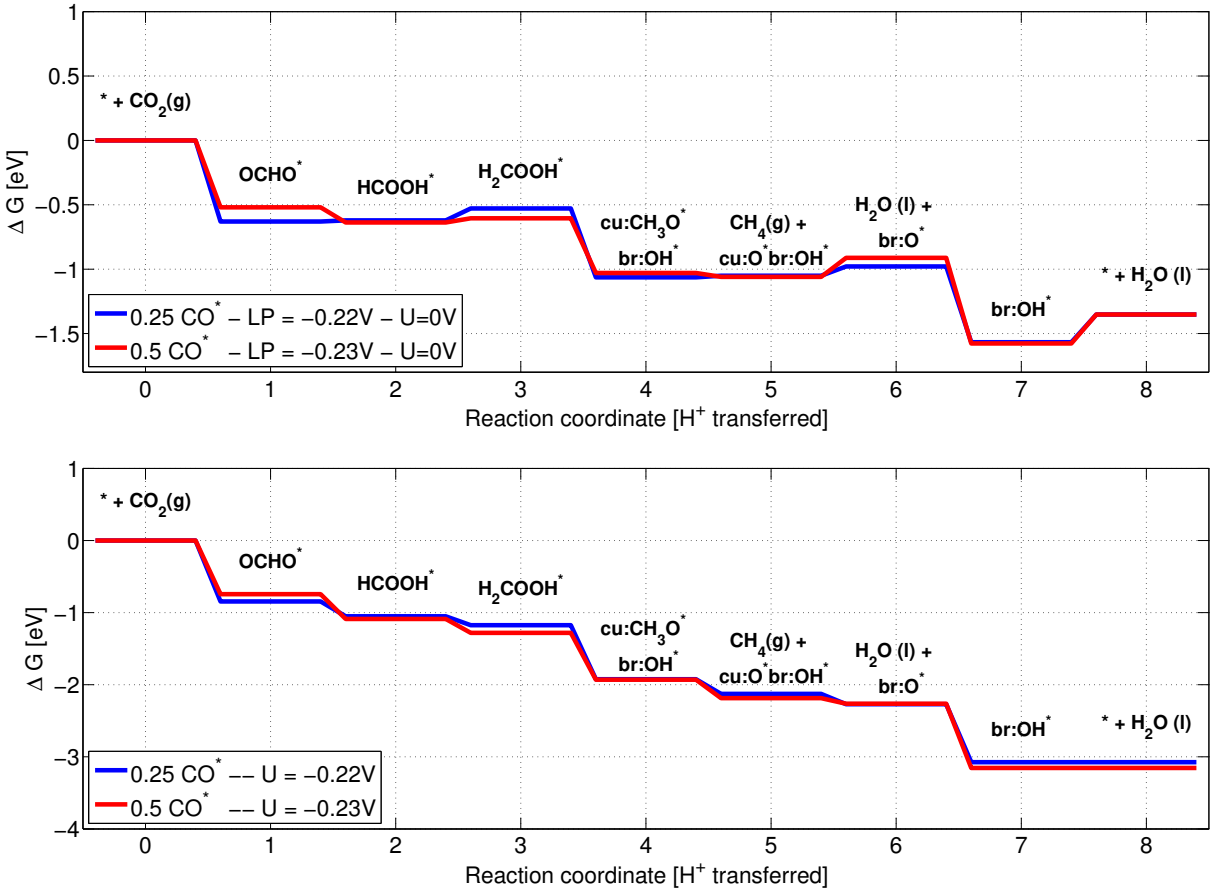

Figure 8.12: Free energy diagrams of CO_2 reduction on IrO_2 at zero potential applied (upper figure) and limiting potential applied (lower figure) at 0.25 CO^* (blue line) and 0.5 CO^* coverage (red line).

protonation of $HCOOH^*$ to H_2COOH^* is potential limiting. Moreover, he observed a limiting potential of $-0.43\,V$ and $-0.28\,V$ on 0.25 CO^* and 0.5 CO^* respectively, as opposed to $-0.8\,V$ and $-0.47\,V$ according to our computations.

On IrO_2 (figure 8.12), the reduction of CO_2 to CH_4 requires significantly lower limiting potentials

($-0.22\,V$ and $-0.23\,V$ on 0.25 CO^* and 0.5 CO^* respectively). Therefore, from a thermodynamical point of view, one could conclude IrO_2 should be a better catalyst than RuO_2 for this reaction. Notice in this case the protonation of OH^* to recover the original surface is the potential limiting step on both CO^* coverages. Another noteworthy difference with RuO_2 is the lower dependence on CO^* coverage. Indeed, on average, blue and red lines tend to remain closer to each other in figure 8.12 than in figure 8.10.

8.6 Other reaction pathways

So far, we have studied the reaction pathway proposed by Karamad *et al.* for the reduction of CO_2 into $CH_{4(g)}$. However, as we have seen in chapter 5, on copper this reaction is known to proceed through a different mechanism. In this section, we will investigate whether the reaction proposed by Karamad *et al.* (see figures 8.10 & 8.12) is indeed more favorable than the reaction mechanism on copper proposed by Peterson *et al.* [49]. The full reaction pathways were given in figure 5.2 on page 32 through the CHO^* intermediate and in figure 5.4 on page 33 through the COH^* intermediate. Both reaction mechanisms will be investigated here.

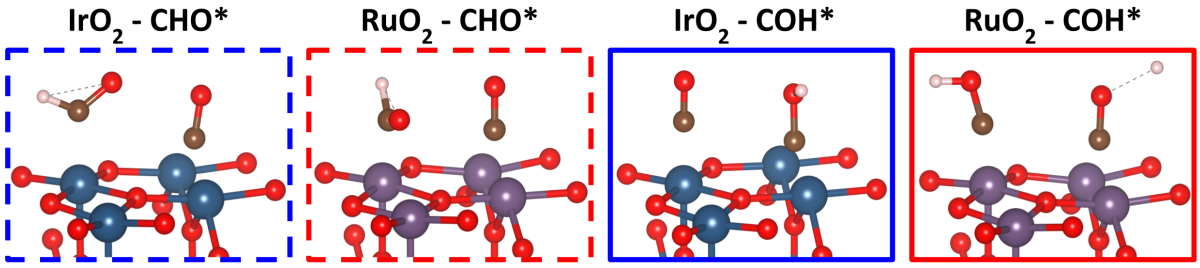

Figure 8.13: CHO^* and COH^* intermediates structures on 0.25 CO^* coverage.

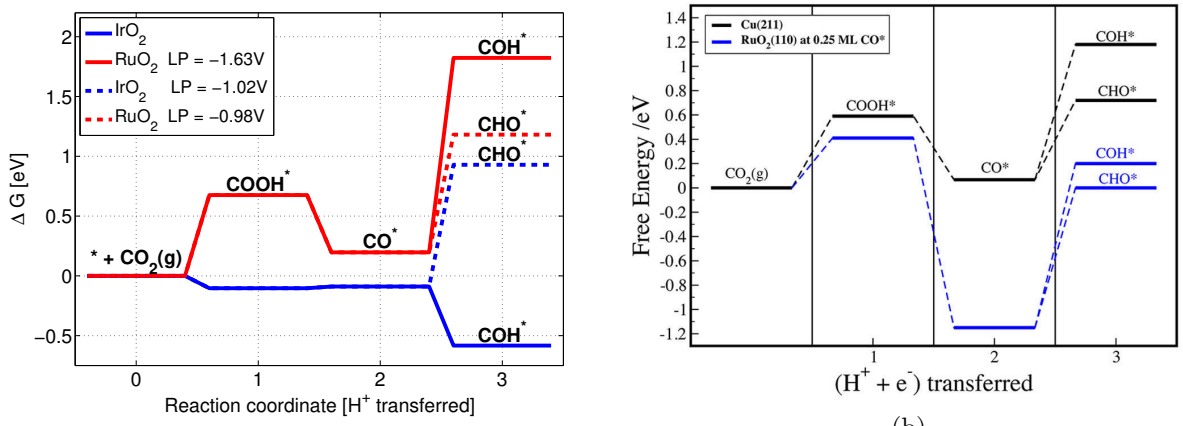

(a) (b)

Figure 8.14: Free energy diagrams for the reduction of CO_2 leading to the structures depicted in figure 8.13, on IrO_2 and RuO_2 (a) and a free energy diagram for the same reaction pathway extracted from the work of Karamad *et al.* on RuO_2 and Cu(211) (b). Limiting potentials (LP) in figure (a) are given for the last reaction step.

The relaxed structures are depicted in figure 8.13. Note that the structures are different on IrO_2 and RuO_2 slabs. Indeed, the CHO^* intermediate is oriented differently on both catalysts. Moreover, on IrO_2, the hydrogen atom from the COH^* intermediate has shifted from its original position on the CUS-site to the CO^* adsorbate on the bridge-site. This did not happen on RuO_2, where the hydrogen atom remained on its original adsorbate.
Figure 8.14 depicts the free energy diagrams constructed from results (a) and a plot extracted

from the work of Karamad *et al.* for comparison on RuO_2 and $Cu(211)$ (b).
Let us first compare RuO_2 in figures (a) (in red) and (b) (in blue). All in all, the the diagrams do not agree very well. However, in both cases, the protonation of CO^* is the limiting potential step. In the reaction pathway proposed by Karamad *et al.* (see figure 8.10), the protonation of $OCHO^*$ to $HCOOH^*$ was the potential limiting step and required $-0.8\,V$ on 0.25 CO^* RuO_2. In contrast, the formation of the COH^* and CHO^* intermediates require $-1.63\,V$ and $-0.98\,V$ respectively. This reaction pathway is thus not favorable as compared to Karamad *et al.*'s pathway. However, the picture is different for IrO_2. Indeed, whereas the formation of the CHO^* intermediate requires similar potential than on RuO_2, the formation of COH^* is exergonic on IrO_2. However, in the reaction pathway proceeding through COH^* on copper, the limiting reaction step is known to be the protonation of CH^* to CH_2^*. Therefore, before being able to draw any conclusions regarding this reaction pathway on IrO_2, the whole reaction mechanism should be investigated. Still, this result opens up new possibilities regarding CO_2 reduction on IrO_2.

8.7 Discussion

In this chapter, we have investigated the CO_2 reduction reaction on IrO_2 and RuO_2 catalysts. First, we started by reproducing results from the work of Karamad *et al.* Although our results matched relatively well, this result benchmarked the margin of error that can be expected in our computations. Also the impact of corrections have proven to be determining, in accordance with what has been demonstrated in chapter 7.
Next, we performed a stability analysis on the CO^* coverage in aqueous medium. Remember Karamad *et al.* study the reduction of CO_2 on 0.25 and 0.5 CO^* covered RuO_2 surfaces (see insets in figure 8.1). We have shown that water-covered surfaces exhibit increased stability as compared to Karamad *et al.*'s coverages. Moreover, our results indicate that CO^* has increased affinity on IrO_2 as compared to RuO_2, whereas H_2O is more stable on RuO_2 as compared to IrO_2. Additionally, we observed that bridge-sites adsorb CO^* more easily than CUS-sites.
After studying the stability of CO^*, we investigated the reaction pathway for the formation of this adsorbate. Here, we have identified the formation of the $COOH^*$ intermediate to be a crucial step. Whereas the formation of this intermediate required significant potential to be formed on a RuO_2 surface, on IrO_2 the formation of CO^* appeared to require very little to no additional potential. This observation is in good accordance with the previously performed stability analysis, where we pointed out that IrO_2 exhibits increased affinity for adsorbed CO^* compared to RuO_2.
After having identified the stability and mechanisms required for the formation of CO^*, we investigated the reaction pathway for the formation of $HCOOH^*$ on 0.25 and 0.5 CO^* surfaces. Karamad *et al.* report this is an important intermediate in the reduction reaction of CO_2 to CH_4 because its formation is potential limiting on the 0.25 CO^* surface. We investigated two different reaction pathways: through an $OCHO^*$ and a $COOH^*$ intermediate. On RuO_2, the $OCHO^*$ pathway turned out to be more favorable, which confirmed Karamad *et al.*'s choice for this intermediate. On IrO_2 however, both reaction pathways seemed to be in close competition. In either case, the overall $HCOOH^*$ formation process turned out to be much more favorable on IrO_2 than on RuO_2.
Having investigated crucial steps in the CO_2 reduction process, we finally studied the overall reaction up to the formation of CH_4, both on 0.25 and 0.5 CO^* coverages. On RuO_2, we established a good fit with Karamad *et al.*'s result. We calculated limiting potentials of -0.8 and $-0.47\,V$ on the 0.25 and 0.5 CO^* coverages respectively. Our limiting potentials overestimated Karamad *et al.*'s findings by 0.37 and $0.19\,V$ on the 0.25 and 0.5 CO^* coverages respectively. Whereas Karamad *et al.* report a different potential determining step on the 0.5 CO^* coverage, we observed the formation of $HCOOH^*$ to be potential determining on both coverages. In the

continuity of our previous findings, also here IrO_2 showed better performances, with limiting potentials as low as -0.22 and $-0.23\,V$ on the 0.25 and 0.5 CO^* coverages respectively.
At last, we investigated the reaction pathways reported on copper for CO_2 reduction. We studied both COH^* and CHO^* intermediates. On RuO_2, these alternative reaction pathways appeared to be less favorable than the mechanism proposed by Karamad *et al.* which was studied before. However, on IrO_2, the COH^* intermediate exhibited astonishing stability.
Table 8.1 summarizes the above discussed results on the 0.25 CO^* and 0.5 CO^* coverages for both IrO_2 and RuO_2. The table clearly highlights the superior activity of the IrO_2 catalyst over RuO_2.

	IrO_2 - 0.25 CO^*	**IrO_2** - 0.5 CO^*	**RuO_2** - 0.25 CO^*	**RuO_2** - 0.5 CO^*
CO^*	-0.01	$-$	-0.68	-1.01
$HCOOH^*_{OCHO^*}$	-0.01	$-$	-0.8	-0.47
$HCOOH^*_{COOH^*}$	$-$	$-$	-0.68	-1.01
$CH_{4(g)}$	-0.22	-0.23	-0.8	-0.47
CHO^*	-1.02	/	-0.98	/
COH^*	$-$	/	-1.63	/

Table 8.1: Required potentials for the formation of the indicated adsorbates/products on the given surfaces. '$-$' denotes the reaction is spontaneous. A '/' indicates the simulation was not performed. Intermediates given as subscript in the first column indicate the intermediate characterizing the reaction mechanism. All values are given in V.

To go further, the entire reaction pathway through the COH^* intermediate on IrO_2 should be computed, before any conclusions can be drawn regarding its potential interest. Additionally, let us not forget we identified the $COOH^*$ intermediate to be an interesting candidate for the formation of the $HCOOH^*$ adsorbate. This might also be investigated further in the future. Moreover, for the sake of comparability, we have studied the same surfaces as Karamad *et al.* for the CO_2 reduction reaction, namely the 0.25 and 0.5 CO^* coverages. A posteriori, this seems like a poor choice given the fact that we have precisely proven these surfaces to exhibit unfavorable stability in aqueous medium. It would have been interesting to investigate the feasibility of this reaction on other surface coverages.

It is important to put the observations we have made throughout this chapter in their due perspective. Indeed, let us not forget that below $0\,V$, the HER becomes favorable, which may compromise the numerous protonation reactions we proposed in this potential range. Moreover, the surfaces we have studied for the CO_2 reduction reaction possess empty active sites. This is a strong hypothesis, as we have demonstrated in this chapter that these sites will likely be covered with water molecules in aqueous medium. However, without the required adsorption sites, the reaction is compromised. Especially as we have seen certain bulky adsorbates may require two adjacent adsorption sites. Also keep in mind that our discussion is limited to the generation of a single product: methane. However, in practice, many other products may be formed during the reduction process, among which we can cite methanol, formic acid, carbon monoxide, ethylene and hydrogen, as was mentioned earlier. Furthermore, the analysis we have performed is limited to thermodynamical considerations. However, experimentally many other aspects are involved, such as the kinetic feasibility of the proposed reactions.
Moreover, notice we assumed gaseous CO_2 would protonate to from $COOH^*$ or $OCHO^*$. However, in practice the gaseous CO_2 will dissolve in water, forming compounds like CO_3^{2-} or HCO_3^-.
At last, it is worth pointing out that comparisons with Karamad *et al.* should be regarded with proper perspective, as errors and inconsistencies have been discovered during the thorough analysis of their article [27].

Chapter 9

Conclusion

The development of new catalyst materials plays a major role in the development of diverse technologies, many of which may contribute to to solving the climate crisis. In this scope, computational materials simulation is a fundamental tool.
In this work, we have studied IrO_2 and RuO_2 catalysts using *ab initio* simulations implemented by VASP. In particular, two distinct reactions were studied on these catalysts: the Oxygen Evolution Reaction (OER) and the CO_2 Reduction Reaction to CH_4.

First, a literature review concerning these two reactions was provided in chapters 4 and 5.
Concerning the OER, the reaction mechanism involving the basic intermediates (OH^*, O^* and OOH^*) was first presented. Next, it was reported that the OER on oxide catalysts requires lower potentials than on metal catalysts [54, 55]. At last, it was demonstrated that the formation of either the O^* or OOH^* intermediate is potential limiting.
Concerning the CO_2 Reduction Reaction, we came to the major conclusion that this reaction is complex and requires many-electron transfers. As a result, the experimental overpotential is large ($\sim 1\,V$) and the selectivity towards specific products is low. Different reaction pathways were identified for investigation, both on metals and on a RuO_2 catalyst.

The major simulation results were presented in chapters 7 and 8. Because the CO_2 Reduction Reaction occurs at reducing (low) potentials, first a preliminary study was performed to investigate possibly intervening OER intermediates at low potentials.
First, standard free energy diagrams of the OER were reproduced. On the one hand, these computations exposed the critical importance of applied corrections such as vdW or ZPE corrections and benchmarked the margin of error to be expected. On the other hand, they validated our computational implementation.
Next, a large inventory of possible OER intermediates (including H_2O^*, OH^*, O^* and H^* adsorbates) was listed and simulated. Structures exhibiting outstanding stability were identified at different applied potentials using relative stability diagrams. Attempts to move adsorbates from their standard positions on the catalysts did not lead to concluding results. However, a hydrogen-covered surface reconstruction (Ir_2O) exhibited competing stability with the conventional hydrogen-covered surface (IrO_2) in the negative potential range.
Comparing IrO_2 to RuO_2, all in all the selection of intermediates showing optimal stability was similar. However, in general the studied adsorbates appeared to be approximately $1\,eV$ more stable on RuO_2 than on IrO_2.

In chapter 8, the simulation results regarding the CO_2 Reduction Reaction were presented. Our analysis was initiated in the same way as for the OER, namely with the reproduction of reference work. Again, these results validated our implementation, but pointed out the importance of applied corrections.

Next, a CO^* coverage stability analysis was performed on both IrO_2 and RuO_2. Here, it was demonstrated that the hypothesis of Karamad *et al.* [27] to leave unoccupied active sites in an aqueous medium is rather unrealistic. Moreover, these results indicated an increased affinity for CO^* on IrO_2 (as compared to RuO_2) on the one hand, and an increased affinity for H_2O on RuO_2 (as compared to IrO_2) on the other hand. Additionally, the CO^* adsorbate was shown to adsorb with increased facility on bridge-sites as compared to CUS-sites.
Next, reaction intermediates and pathways for the reduction of CO_2 to CH_4 were investigated using free energy diagrams. First, we have shown that the formation of the CO^* intermediate is more favorable on IrO_2 as compared to RuO_2. Next, two different pathways for the formation of $HCOOH^*$ were investigated: through a $COOH^*$ or $OCHO^*$ intermediate. Whereas on RuO_2 the $OCHO^*$ intermediate clearly required lower energy, on IrO_2 both reaction pathways seemed to be in competition. After these preliminary studies, the full reaction pathway of CO_2 reduction to CH_4 was studied on both IrO_2 and RuO_2, according to the reaction mechanism and the catalyst surface suggested by Karamad *et al.* On RuO_2, a good fit was established with reference work: our overpotentials overestimated the results of Karamad *et al.* by 0.37 and $0.19\,V$ on both studied surfaces. On IrO_2 the reduction of CO_2 to CH_4 required astonishingly low potential as compared to RuO_2. At last, we investigated the reaction pathways commonly accepted on copper. Whereas on RuO_2 the investigated mechanism did not depict interesting energetic stability, on IrO_2 a promising reaction pathway was identified through a COH^* intermediate. However, full simulation of this reaction pathway would be required to validate this assertion.

In the introduction, it was established that a good catalyst should meet three important requirements: high selectivity towards required products, high activity for the formation of the desired products and high stability under reaction conditions. In this work, one of these aspects was investigated, namely the activity for the formation of the desired products. Possible surface configurations were identified using relative stability diagrams and the activity of the IrO_2 and RuO_2 catalysts was assessed through a qualitative analysis by means of free energy diagrams. However, along the discussion of the presented simulations, awareness was raised to a proper interpretation of the given results. Indeed, our study solely accounts for thermodynamical factors. However, in practice, the HER and kinetic barriers will largely affect the discussed reactions.

In essence, the simulations performed throughout this work have pointed out a tendency towards increased catalytic activity of IrO_2 compared to RuO_2 regarding the CO_2 reduction reaction to methane.

Bibliography

[1] B. Berger, P. Billuart, H. Jeanmart, and J. Proost. FSAB1302 - Equilibre électro-chimique, lecture notes. *Université Catholique de Louvain*, 2016.

[2] B. Boveri. Ruthenium dioxide as a hydrogen-evolving cathode. *Journal of Applied Electrochemistry*, 17:1190–1197, 1987.

[3] J.-C. Charlier, X. Gonze, L. Piraux, and G.-M. Rignanese. MAPR1492 - Physique des Matériaux, lecture notes. *Université Catholique de Louvain*, 2015.

[4] J.-C. Charlier, X. Gonze, and G.-M. Rignanese. MAPR2451 - Atomistic & Nanoscopic Simuations, lecture notes. *Université Catholique de Louvain*, 2016.

[5] S. Cherevko, S. Geiger, O. Kasian, N. Kulyk, J. P. Grote, A. Savan, B. R. Shrestha, S. Merzlikin, B. Breitbach, A. Ludwig, and K. J. J. Mayrhofer. Oxygen and hydrogen evolution reactions on Ru, RuO2, Ir, and IrO2 thin film electrodes in acidic and alkaline electrolytes: A comparative study on activity and stability. *Catalysis Today*, 262:170–180, 2016.

[6] E. R. Davidson. The iterative calculation of a few of the lowest eigenvalues and corresponding eigenvectors of large real-symmetric matrices. *Journal of Computational Physics*, 17:87–94, 1975.

[7] R. L. Doyle and M. E. G. Lyons. *The Oxygen Evolution Reaction: Mechanistic Concepts and Catalyst Design*. Springer International Publishing, 2016.

[8] E. Fabbri, A. Habereder, K. Waltar, R. Kötz, T. J. Schmidt, R Kotz, and T. J. Schmidt. Developments and perspectives of oxide-based catalysts for the oxygen evolution reaction. *Catalysis Science & Technology*, 4:3800–3821, 2014.

[9] R. P. Feynman. Forces in molecules. *Physical Review*, 56:340–343, 1939.

[10] A. Gilbert. Introduction to Computational Quantum Chemistry: Theory, lecture notes. *The Australian National University*, 2007.

[11] S. Grimme. Semi-empirical GGA-Type Density Functional Constructed with a Long-Range Dispersion Correction. *Journal of computational chemistry*, 27:1787–1799, 2006.

[12] S. Grimme, J. Antony, S. Ehrlich, and H. Krieg. A consistent and accurate ab initio parametrization of density functional dispersion correction (DFT-D) for the 94 elements H-Pu. *Journal of Chemical Physics*, 132:154104, 2010.

[13] S. Grimme, S. Ehrlich, and L. Goericgk. Effect of the Damping Function in Dispersion Corrected Density Functional Theory. *Journal of computational chemistry*, 32:1456–1465, 2011.

[14] R. Guidelli, R. G. Compton, J. M. Feliu, E. Gileadi, J. Lipkowski, W. Schmickler, and S. Trasatti. Defining the transfer coefficient in electrochemistry: An assessment (IUPAC Technical Report). *Pure and Applied Chemistry*, 86:245–258, 2014.

[15] J. Hafner, G. Kresse, A. Eichler, R. Lorenz, and R. Hirschl. Ab-initio simulations in materials science, VASP workshop lectures. *Center for Computational Material Science, Universität Wien*, 2003.

[16] D. Hamann, M. Schlüter, and C. Chiang. Norm-Conserving Pseudopotentials. *Physical Review Letters*, 43:1494–1497, 1979.

[17] B. Hammer, L. Hansen, and J. K. Nørskov. Improved adsorption energetics within density-functional theory using revised Perdew-Burke-Ernzerhof functionals. *Physical Review B*, 59:7413–7421, 1999.

[18] B. Hammer and J. K. Norskov. Theoretical Surface Science and Catalysis — Calculations and Concepts. *Advances in Catalysis*, 45:71–129, 2000.

[19] H. A. Hansen, J. Rossmeisl, and J. K. Nørskov. Surface Pourbaix diagrams and oxygen reduction activity of Pt, Ag and Ni(111) surfaces studied by DFT. *Physical Chemistry Chemical Physics*, 10:3722–3730, 2008.

[20] H. A. Hansen, C. Shi, A. Lausche, A. Peterson, and J. K. Nørskov. Bifunctional alloys for the electroreduction of CO2 and CO. *Physical Chemistry Chemical Physics*, 18:9194–9201, 2016.

[21] H. Hellmann. Einführung in die Quantenchemie. *Angewandte Chemie*, 54:156, 1937.

[22] N. Hidetomo, I. Shoichiro, Y. Akio, E. Hisahiko, and I. Kaname. Kinetics of Electrochemical Reduction of Carbon Dioxide on a Gold Electrode in Phosphate Buffer Solutions. *Bulletin of the Chemial Society of Japan*, 68:1889–1895, 1994.

[23] Y. Hori. Electrochemical CO 2 Reduction on Metal Electrodes. In C. G. Vayenas, R. E. White, and M. E. Gamboa-Aldeco, editors, *Modern Aspects of Electrochemistry*, number 42, chapter 3, pages 89–189. Springer New York, Chiba, Japan, 2008.

[24] Y. Hori, A. Murata, and R. Takahashi. Formation of hydrocarbons in the electrochemical reduction of carbon dioxide at a copper electrode in aqueous solution. *Journal of the Chemical Society, Faraday Transactions 1*, 85:2309–2326, 1989.

[25] Z. P. Jovanov, H. A. Hansen, A. S. Varela, P. Malacrida, A. A. Peterson, J. K. Norskov, I. E. L. Stephens, and I. B. Chorkendorff. Opportunities and challenges in the electrocatalysis of CO2 and CO reduction using bifunctional surfaces: A theoretical and experimental study of Au-Cd alloys. *Journal of Catalysis*, 343:215–231, 2016.

[26] M. Karamad, H. A. Hansen, J. Rossmeisl, and J. K. Nørskov. Mechanistic Pathway in the Electrochemical Reduction of CO 2 on RuO 2: Sup Info. *ACS Catalysis*, 5:4075–4081, 2015.

[27] M. Karamad, H. A. Hansen, J. Rossmeisl, and J. K. Norskov. Mechanistic Pathway in the Electrochemical Reduction of CO2 on RuO2. *ACS Catalysis*, 5:4075–4081, 2015.

[28] W. Kohn and L. J. Sham. Self-consistent equations including exchange and correlation effects. *Physical Review*, 140:A1133–A1138, 1965.

[29] R. Kortlever, J. Shen, K. J. P. Schouten, F. Calle-vallejo, and M. T. M. Koper. Catalysts and Reaction Pathways for the Electrochemical Reduction of Carbon Dioxide. *Journal of Physical Chemistry Letters*, 6:4073–4082, 2015.

[30] G. Kresse. From ultrasoft pseudopotentials to the projector augmented-wave method. *Physical Review B*, 59:1758–1775, 1999.

[31] G. Kresse and J. Furthmüller. Efficiency of ab-initio total energy calculations for metals and semiconductors using a plane-wave basis set. *Computational Materials Science*, 6:15–50, 1996.

[32] G. Kresse and J. Furthmüller. Efficient iterative schemes for ab initio total-energy calculations using a plane-wave basis set. *Physical Review B*, 54:11169–11186, 1996.

[33] G. Kresse and J. Hafner. Ab initio molecular dynamics for liquid metals. *Physical Review B*, 47:558–561, 1993.

[34] G. Kresse, M. Marsman, and J. Furthmüller. Vienna Ab-initio Package Vienna Simulation: VASP the GUIDE. Technical report, Computational Materials Physics, Faculty of Physics, Universität Wien, 2014.

[35] G. Kreysa, K.-I. Ota, and R. Savinell. *Encyclopedia of Applied Electrochemistry*. Springer-Verlag New York, 1 edition, 2014.

[36] K. P. Kuhl, T. Hatsukade, E. R. Cave, D. N. Abram, J. Kibsgaard, and T. F. Jaramillo. Electrocatalytic Conversion of Carbon Dioxide to Methane and Methanol on Transition Metal Surfaces. *Journal of the American Chemical Society*, 136:14107–14113, 2014.

[37] D.-Y. Kuo, J. K. Kawasaki, J. N. Nelson, J. Kloppenburg, G. Hautier, K. M. Shen, D. G. Schlom, and J. Suntivich. Influence of Surface Adsorption on the Oxygen Evolution Reaction on IrO2(110). *Journal of the American Chemical Society*, 2:3473–3479, 2017.

[38] June Gunn Lee. *Computational Materials Science: An Introduction*. CRC Press, 2012.

[39] Y Liu and Q Jinli. Introduction to CO2 Electroreduction. In Q. Jinli, L. Yuyu, and Z. Jiujun, editors, *Electrochemical Reduction of Carbon Dioxide*, chapter 1, pages 1–33. CRC Press, Vancouver, 2016.

[40] I. C. Man, H. Y. Su, F Calle-Vallejo, H. A. Hansen, J. I. Martínez, N. G. Inoglu, J. Kitchin, T. F. Jaramillo, J. K. Nørskov, and J. Rossmeisl. Universality in Oxygen Evolution Electrocatalysis on Oxide Surfaces. *ChemCatChem*, 3:1159–1165, 2011.

[41] M. Methfessel and A. T. Paxton. High-precision sampling for Brillouin-zone integration in metals. *Physical Review B*, 40:3616–3621, 1989.

[42] Global Footprint Network. Earth overshoot day, 2017. [Online; accessed 13-August-2017].

[43] X. Nie, M. R. Esopi, M. J. Janik, and A. Asthagiri. Selectivity of CO2 reduction on copper electrodes: The role of the kinetics of elementary steps. *Angewandte Chemie - International Edition*, 52:2459–2462, 2013.

[44] J. K. Nørskov, J. Rossmeisl, A. Logadottir, L. Lindqvist, J. R. Kitchin, T. Bligaard, and H. Jónsson. Origin of the overpotential for oxygen reduction at a fuel-cell cathode. *Journal of Physical Chemistry B*, 108:17886–17892, 2004.

[45] J. D. Pack and H. J. Monkhorst. Special points for Brillouin-zone integrations. *Physical Review B*, 16:1748–1749, 1977.

[46] J. P. Perdew, K. Burke, and M. Ernzerhof. Generalized Gradient Approximation Made Simple. *Physical Review Letters*, 77:3865–3868, 1996.

[47] J. P. Perdew and Y. Wang. Accurate and Simple Representation of the Electron-Gas Correlation-Energy. *Physical Review B*, 45:13244–13249, 1992.

[48] A. Peterson and J. K. Nørskov. Activity Descriptors for CO2 Electroreduction to Methane on Transition Metal Catalysts. *The Journal of Physical Chemistry Letters*, 3:251–258, 2012.

[49] A. A. Peterson, F. Abild-Pedersen, F. Studt, J. Rossmeisl, and J. K. Nørskov. How copper catalyzes the electroreduction of carbon dioxide into hydrocarbon fuels. *Energy & Environmental Science*, 3:1311, 2010.

[50] A. A. Peterson and J. K. Nørskov. Activity descriptors for CO 2 electroreduction to methane on transition-metal catalysts: SUP INFO. *Journal of Physical Chemistry Letters*, 3:251–258, 2012.

[51] P. Pulay. Convergence acceleration of iterative sequences. the case of scf iteration. *Chemical Physics Letters*, 73:393–398, 1980.

[52] D. Rochefort, P. Dabo, D. Guay, and P. M. A. Sherwood. XPS investigations of thermally prepared RuO2 electrodes in reductive conditions. *Electrochimica Acta*, 48:4245–4252, 2003.

[53] J. Rossmeisl. Water-Splitting Conceptual Approach. In R. Schlögl, editor, *Chemical Energy Storage*, chapter 3.2, pages 151–162. De Gruyter, Berlin, 2013.

[54] J. Rossmeisl, A. Logadottir, and J. K. Nørskov. Electrolysis of water on (oxidized) metal surfaces. *Chemical Physics*, 319:178–184, 2005.

[55] J. Rossmeisl, Z. W. Qu, H. Zhu, G. J. Kroes, and J. K. Nørskov. Electrolysis of water on oxide surfaces. *Journal of Electroanalytical Chemistry*, 607:83–89, 2007.

[56] N. Spataru, K. Tokuhiro, C. Terashima, T. N. Rao, and A. Fujishima. Electrochemical reduction of carbon dioxide at ruthenium dioxide deposited on boron-doped diamond. *Journal of Applied Electrochemistry*, 33:1205–1210, 2003.

[57] N.-T. Suen, S.-F. Hung, Q. Quan, N. Zhang, Y.-J. Xu, and H. M. Chen. Electrocatalysis for the oxygen evolution reaction: recent development and future perspectives. *Royal Society of Chemistry*, 46:337–365, 2017.

[58] A. Tkatchenko and M. Scheffler. Accurate molecular van der Waals interactions from ground-state electron density and free-atom reference data. *Physical Review Letters*, 102:6–9, 2009.

[59] N. Troullier and J. L. Martins. Efficient pseudopotentials for plane-wave calculations. *Physical Review B*, 43:8861–8869, 1991.

[60] H. Ünal, E. Mete, and S. Ellialtioglu. Re-assigning (1x2) reconstruction of rutile TiO2(110) from DFT+U calculations. *Physical Review B*, 84:115407, 2011.

[61] D. Vanderbilt. Soft self-consistent pseudopotentials in a generalized eigenvalue formalism. *Physical Review B*, 41:7892–7895, 1990.

[62] Y. Wang, M. Hatakeyama, K. Ogata, F. Jin, and S. Nakamura. Modeling of Electrochemical CO2 Reduction. In Q. Jinli, L. Yuyu, and Z. Jiujun, editors, *Electrochemical Reduction of Carbon Dioxide*, chapter 8, pages 311–328. CRC Press, Vancouver, 2016.

[63] Wikipedia. Bell–evans–polanyi principle — Wikipedia, the free encyclopedia, 2004. [Online; accessed 18-August-2017].

[64] Wikipedia. Electrocatalyst — Wikipedia, the free encyclopedia, 2004. [Online; accessed 22-April-2017].

[65] Wikipedia. Projector augmented wave method — Wikipedia, the free encyclopedia, 2004. [Online; accessed 9-August-2017].

[66] Wikipedia. Pseudopotential — Wikipedia, the free encyclopedia, 2004. [Online; accessed 17-July-2017].

[67] Wikipedia. Standard hydrogen electrode — Wikipedia, the free encyclopedia, 2004. [Online; accessed 2-May-2017].

[68] D. M. Wood and A. Zunger. A new method for diagonalising large matrices. *Journal of Physics A: Mathematical and General*, 18:1343–1359, 1985.

Appendix A

Additional relative stability diagrams

The major purpose of this appendix is not to investigate the stability of intermediates but to give an overview of the complete set of simulated structures.
(see next page)

A.1 OER adsorbates inventory study: preliminary selection

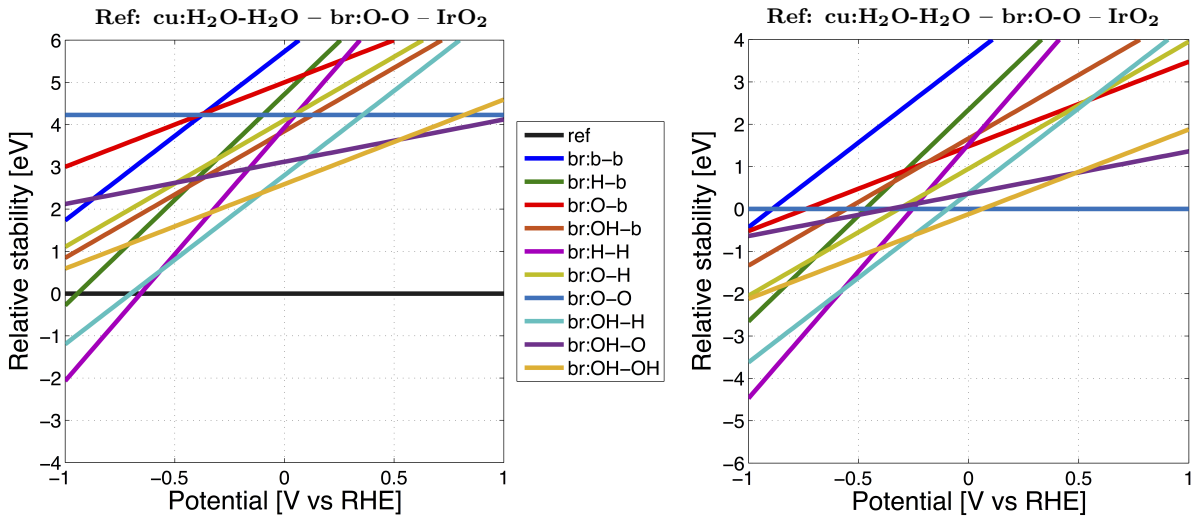

(a) cu:b-b (b) cu:H_2O-H_2O

Figure A.1: Overview of the stability of OER intermediates on IrO_2 slabs. In figure (a) both CUS-sites are left bare, in figure (b) both CUS-sites are occupied by water.

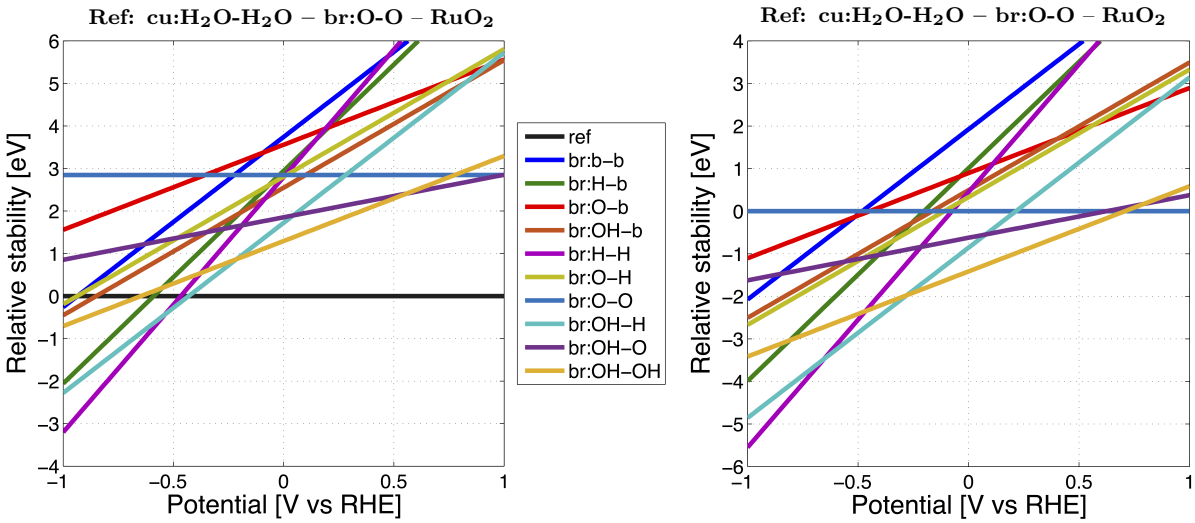

(a) cu:b-b (b) cu:H_2O-H_2O

Figure A.2: Overview of the stability of OER intermediates on RuO_2 slabs. In figure (a) both CUS-sites are left bare, in figure (b) both CUS-sites are occupied by water.

A.2 OER adsorbates inventory study: full overview

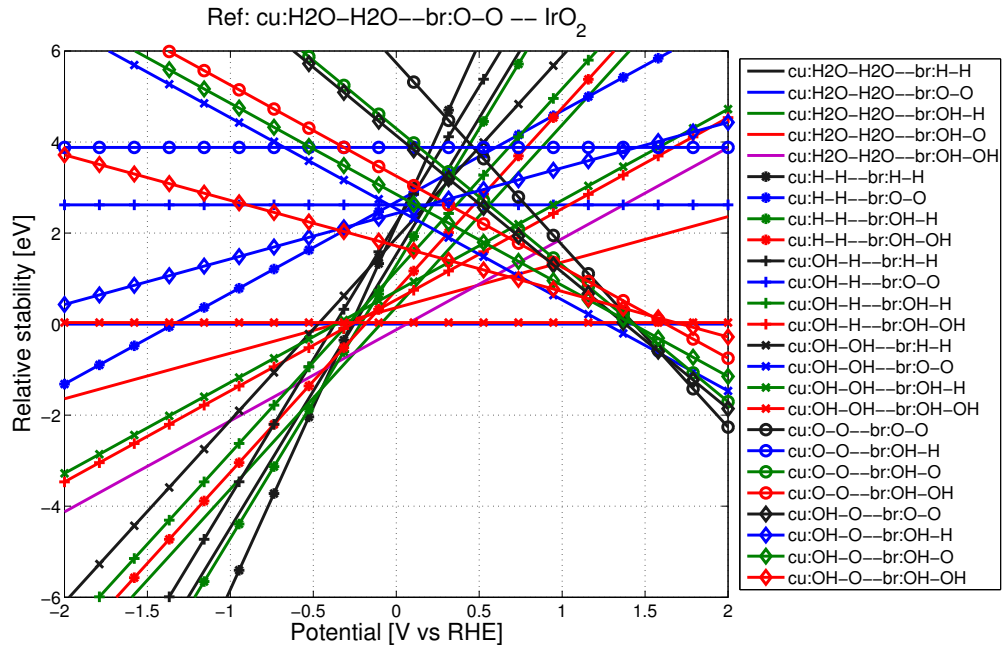

Figure A.3: Overview of all attempted intermediates for OER on IrO_2 plotted in a relative stability diagram

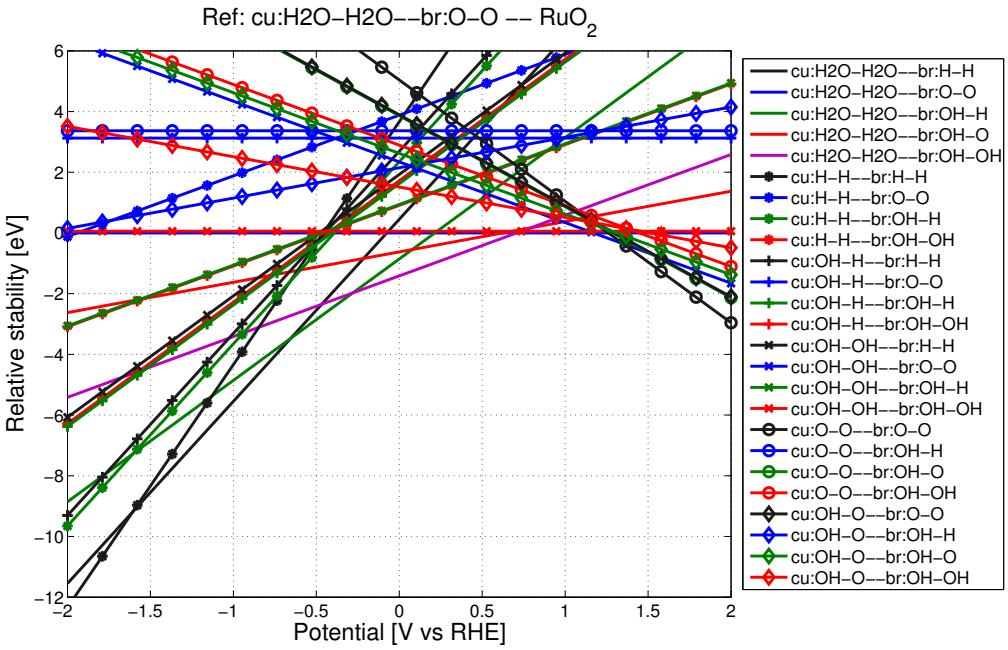

Figure A.4: Overview of all attempted intermediates for OER on RuO_2 plotted in a relative stability diagram

A.3 CO^* coverage analysis

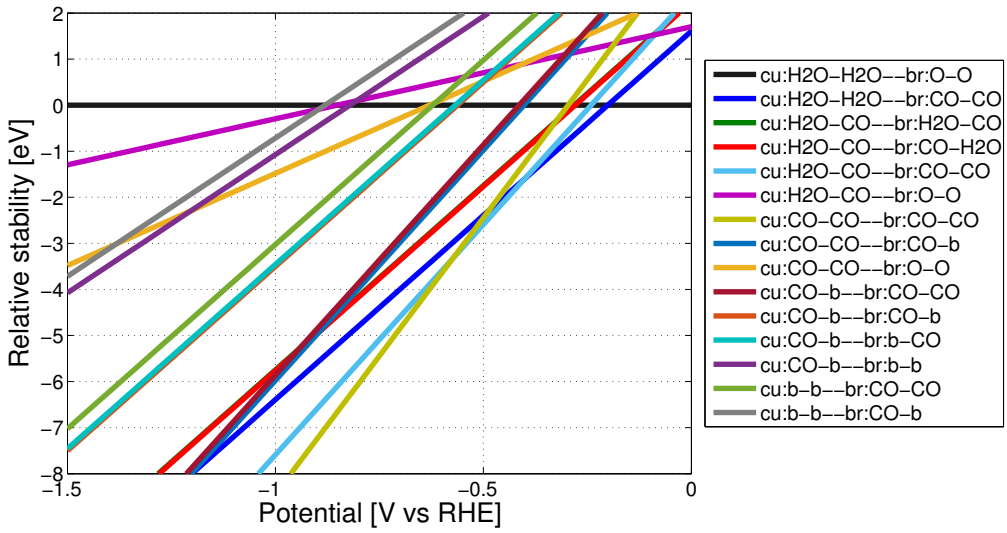

Figure A.5: Overview of the stability of all selected structures for the investigation of CO^* coverage on IrO_2 plotted in a Pourbaix diagram

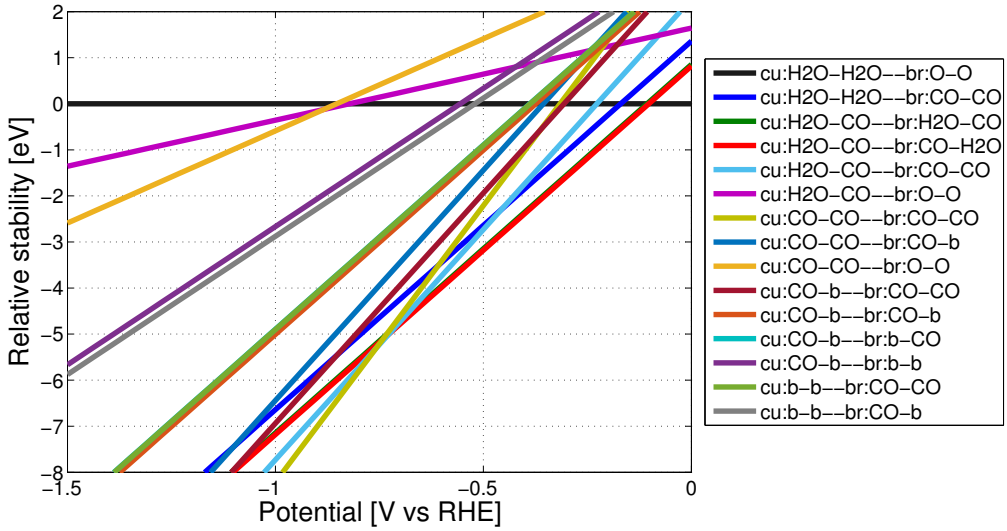

Figure A.6: Overview of the stability of all selected structures for the investigation of CO^* coverage on RuO_2 plotted in a Pourbaix diagram

Rue Archimède, 1 bte L6.11.01, 1348 Louvain-la-Neuve **www.uclouvain.be/epl**